CRANFIELD UNIVERSITY

ASLAM ABDULLAH

QUANTIFYING GUIDELINES AND CRITERIA FOR USING TURBULENCE MODELS IN COMPLEX FLOWS

SCHOOL OF ENGINEERING

PhD THESIS
Academic Year: 2011 - 2012

Supervisor: Professor A. M. Savill
November 2011

CRANFIELD UNIVERSITY

SCHOOL OF ENGINEERING

PhD THESIS

Academic Year 2011 - 2012

ASLAM ABDULLAH

Quantifying guidelines and criteria for using turbulence models in complex flows

Supervisor: Professor A. M. Savill

November 2011

Abstract

A framework for assessing the key statistical parameters of complex flows in choosing appropriate turbulence prediction methods on a quantitative basis is developed. These parameters characterise flow/modelling matching conditions quantified in this work. Matching conditions are important in classifying complex turbulent flows in order to frame best practice for model predictions to inform computational aerodynamics design optimisation in the context of virtual test beds. In the incompressible low Reynolds number shear flows considered here, the boundaries of the 'conforming domain' within which turbulence models are valid need to be defined, based on basic mechanisms of turbulence, and the statistical parameters. This has led to a new guideline 'localness map' for standard model applications. Since the choice of turbulence model depends on the complexity of the flows considered, it is useful if systematic sets of the parameters indicate the type of flow. They are that of residence time, the degree of spatial non-locality, the straining, and the non-Gaussianity, each of which is appropriately normalised. It can be demonstrated that the quantified map, in particular that of localness for the shear flows, provides a firm foundation for evaluating a wider range of Underlying Flow Regimes, including locating the Underlying Flow Regimes on the generalised localness modeling map as a framework for best practice guidelines. This work produces 7 sets of quantitative localness-structural parameters, which are used as baseline sets for grouping the Underlying Flow Regimes, and hence it opens the possibility of having complete modelling maps for Application Challenges to assess the need for zonal modelling.

Keywords:
Localness-structural parameters, one-point closure, DNS, LES, ERCOFTAC Application Challenges

Acknowledgements

First and foremost, I would like to express my deep and sincere gratitude to Prof. Mark Savill for his excellent support and guidance on various aspects throughout the time of this work, from whom I have learnt a great deal, and who has provided inspiration for pursuing an academic career. His knowledge, comments and advice have been invaluable.

I am indebted to Prof. Coleman from the Aerodynamics and Flight Mechanics (AFM) research group, University of Southampton, for allowing me to use their DNS Database Web Server facilities. Also from the AFM research group, I thank Dr. Maksym Bondarenko for organising my use of the Master-Mode Database, and for stimulating discussions about the manipulation of the DNS data.

Within the Computational Aerodynamics and Combustion Design group there are many colleagues from whom I have benefitted, either with simulation datasets or technical conversations, or simply friendly moral support; these include Dr. Ranga Dinesh, Apostolos Spanelis and Nurul Mazlan.

These acknowledgements would be incomplete without sincere thanks to my wife Radhiah for her support and faith in me during the hardship of my studies, and to my parents who always encouraged me to achieve the best.

To my beloved daughter, Iris.

Table of contents

List of figures

List of tables

List of equations

Nomenclature

$\bar{\bullet}$	ensemble mean value
$\vec{\bullet}$	vector valued quantity
$\frac{\mathrm{D}}{\mathrm{D}t} \equiv \frac{\partial}{\partial t} + \bar{u}_m \frac{\partial}{\partial x_m}$	substantial derivative based on advection by mean velocity
$\nabla\bar{\mathrm{u}}$	gradients of the mean velocity
$\nabla\mathrm{k}$	gradients of the turbulent kinetic energy
$a_{ij} \equiv \frac{R_{ij}}{k} - \frac{2}{3}\delta_{ij}$	Reynolds stress anisotropy tensor
$f_i, \bar{f}_i, f_i'$	total, mean, and fluctuating body force (per unit mass)
J_{ijk}	turbulent flux of the Reynolds stress tensor, including pressure transport
$k \equiv \frac{1}{2}\overline{u_i' u_i'}$	turbulent kinetic energy (per unit mass)
$p\left(\vec{x},t\right)$	total pressure field
$\bar{p}$	mean pressure
p'	pressure fluctuation
$R_{ij} \equiv \overline{u_i' u_j'}$	$-\rho R_{ij}$ is the Reynolds stress tensor
Re	(any) Reynolds number
s_{ij}, S_{ij}, s_{ij}'	total, mean, and fluctuating parts of the strain rate tensor
$u_i\left(\vec{x},t\right)$	total velocity field
$\bar{u}_i$	mean velocity
u_i'	velocity fluctuation
u_o	energy containing eddies velocity scale
u^*	wall friction velocity
U_e	velocity at the edge of the boundary layer
U_o	free stream velocity
U_1	local velocity
Q	potential sink strength
h	step height
$\left(u_1,u_2,u_3\right) \Leftrightarrow \left(u,v,w\right)$	alternative notation
$\left(x_1,x_2,x_3\right) \Leftrightarrow \left(x,y,z\right)$	alternative notation
x_2 or y	wall normal coordinate
x_i'	cartesian coordinates which move with the mean flow
$\varepsilon \equiv \nu \overline{\frac{\partial u_i'}{\partial x_k} \frac{\partial u_i'}{\partial x_k}}$	(homogeneous) dissipation rate

$\varepsilon_{ij} \equiv 2\nu \overline{\frac{\partial u_i'}{\partial x_k} \frac{\partial u_j'}{\partial x_k}}$	(homogeneous) dissipation rate tensor
μ	dynamic molecular viscosity
$\mu_{laminar}$	dynamic molecular viscosity in laminar region
$\mu_{turbulent}$	dynamic molecular viscosity in turbulent region
ν	kinematic molecular viscosity
μ_t	eddy viscosity
μ_{t_o}	eddy viscosity in the outer part of the defect layer
ν_t	kinematic eddy viscosity
τ	shear stress
ρ	fluid density
σ	turbulent Prandtl-Schmidt number
σ_{ij}	second order moments
St	non-dimensional time
$\omega_{ij}, \Omega_{ij}, \omega_{ij}'$	total, mean, and fluctuating parts of the rotation rate tensor
l_m	mixing length
l_o	old mixing length
κ	Von Karman constant
y^+	wall normal coordinate
δ^*	displacement thickness
δ	boundary layer thickness
S	mean shear
$G(z)$	filter kernels
Δ	change in turbulence quantities
L_X	eddy length scale
$\tilde{L}_X$	degree of non-locality
$\tilde{L}_{X_{av}}$	averaged degree on non-locality
$\Lambda^{k)}$	scale over which the turbulence structure varies
$\Lambda^{(\Sigma)}$	scale over which the mean strain rate varies
$\Lambda^{(\bar{u})}$	scale over which the mean strain rate varies in a shear flow
T'	time scale
T'_{av}	averaged time scale
y_{av}	averaged wall normal coordinates
n	number of samples
T_L	integral tme scale
$\tilde{T}_L$	degree of non-equilibrium
T_D	distortion time scale

$\tilde{T}_{L_{av}}$	averaged degree of non-equilibrium
$\tilde{A}$	sign of the advective term in a turbulent kinetic energy equation
$\tilde{S}$	strain parameter
$\tilde{S}_{av}$	averaged strain parameter
$\tilde{G}$	degree of non-Gaussianity
Σ_{ij}	symmetric strain (stretching) tensor
Ω_l	vorticity
ε_{lmn}	levi-civita tensor
$pr()$	probability distribution function
K_i	kurtosis, or flatness factor
S_i	skewness factor

Acronyms

AC	Application challenge
AFM	Aerodynamics and Flight Mechanics
ARSM	Algebraic Reynolds stress model
CFD	Computational Fluid Dynamics
CTF	Complex Turbulent Flow
DES	Detached eddy simulation
DNS	Direct numerical simulation
DNS	Direct numerical simulation
DSM	Distorted structural model
ER	Expansion ratio
ERCOFTAC	European Research Community on Flow, Turbulence, and Combustion
EU	European Union
EVM	Eddy viscosity model
HVAC	Heating, ventilation and air-conditioning
INI	Isaac Newton Institute
LES	Large eddy simulation
RANS	Reynolds-averaged Navier-Stokes
RDT	Rapid distortion theory
RHS	Right hand side
RNG	Renormalization group theory
RSM	Reynolds stress transport model
SGS	Subgrid-scale model
UDF	User defined function
UFR	Underlying flow regime
UKTC	UK Turbulence Consortium
ZM	Zonal modelling

Abbreviations

qual.	qualitative
quan.	quantitative
1D	one dimensional
2D	two dimensional
max	maximum

1
Introduction and thesis structure

1.1 Introduction

A vast array of turbulence models currently exists for predictions, which have been largely developed for simple shear layers. There is, however, a need to document and indeed 'map' these models more fully against flow types so as to select a 'best' model more systematically for a given flow – see [1]. This is achievable by grasping a more physical understanding of the dominant mechanisms of turbulence, which might then increase our ability to predict them.

This work concerns the guidelines and criteria to understand and predict complex turbulent flows. Its goal is to develop a best practice guidelines framework for turbulence modelling applications to inform computational fluid dynamics optimisation in the context of virtual reality test beds. In complex flows, the boundaries of the 'conforming domain' outside which these turbulence models are invalid need to be considered. As in the derivation of the models themselves, special assumptions based on physics are needed to define this domain (once defined, the domain can be represented by, for instance, a certain number of mesh points). The definition is driven by considerations of the basic mechanisms of turbulence, and characteristic statistical parameters, which lead to a new guideline 'map', as proposed by Hunt and Savill [1], for standard model applications in the kind of complex flows that are analysed in industrial and environmental problems.

In general, three types of standard models at the single-point closure level are considered, which are the local (mixing length) models, eddy viscosity models, as well as Reynolds stress models. Since the applications of turbulence models depend on the complexity of the flows considered, it is useful if a systematic set of appropriate parameters indicates the type of flows. Such parameters have been identified.

The intrinsic inhomogeneity of turbulence dynamics emerges when the scale Λ over which the turbulence structure or mean strain rate varies is of the order of the length scale L_X (of the eddies which contain much of the energy spectrum of turbulence) or smaller. Such degree of non-locality[1] $-\tilde{L}_X$ then, is the ratio of L_X to Λ with negative sign (to indicate non-localness of turbulence), and is the first statistical parameter of interest.

The dependence of the advected turbulence on the upstream boundary conditions, or the initial conditions, is represented by the degree of non-equilibrium of turbulence structure or the residence time parameter $\tilde{T}_L$. This parameter is defined by the 'turn-over' timescale T_L (which corresponds to L_X) scaled on the distortion timescale T_D (i.e. the time spent by a fluid particle in a domain). Studies have shown that in fully developed turbulent flows, the eddy structure, as characterised by certain statistical properties, has forms such as vortex sheets, streaky jets, and elongated vortices, either caused by swirling, shearing or pure staining motions – see [2]. These motions correspond to the third parameter, the normalised strain parameter $\tilde{S}$ derived from the gradients of the mean velocity $\nabla\bar{u}$. Finally the non-Gaussianity parameter $\tilde{G}$ has to be considered because only if the probability distribution of the fluctuating velocity is close to that of Gaussian variable, will third order moments emerging from the eddy kinetic energy equations have a general relation to second order moments σ_{ij}. This is defined by $\tilde{G}$'s magnitude being small.

[1] ,[2] Refer to more detailed definition in page 50-61.

All these parameters[2] are appropriately normalised, and have been carefully and qualitatively estimated [1] on a purely mathematical-empirical basis.

However, direct numerical simulation (DNS) and highly resolved large eddy simulations (LESs) data now provide a means for refining and quantifying the estimates and hence establishing a firmer framework for their 'map'. If it seems that more simulations are required to be done, they should be well defined, specific, and have very clear objectives. The previous databases (simulation and experimental results) may provide sufficient information needed in defining the parameters for a limited range of complex flows. A range of datasets has been selected for such refinement, based on the mathematical expression from associated literature, and on dimensional analysis involving the heuristic process. Although their values are different, with different total number of grid points and flow segments considered for each flow case, the most representative fall within the estimated range.

An alternative parameter estimate can also be performed by considering two-point correlations of the flow particle velocities. In principle, having plotted the variation of the velocity fluctuations (e.g. u) in space, the length scale L_X is given by the distance between two consecutive points which correspond to the correlated u with different signs (+ve and -ve). This information can be obtained from the running DNS.

The connection between the structural parameters (i.e. the strain $\tilde{S}$ and non-Gaussianity $\tilde{G}$) and localness of the turbulence have not previously been much focused on, but are addressed in this work since they offer other potential dimensions to the (2D) non-localness map that could potentially help to further differentiate types of flow and their modelling. It seems it may indeed be possible to use DNS to put all four map parameters as well as the map itself on a quantitative basis as a framework for best practice guidelines for predictions of turbulent flows of practical and environmental importance. This includes locating underlying flow regimes (UFRs) arising from

application challenges (ACs) on the guideline map for choosing appropriate prediction methods.

1.2 Objectives

The objectives set out in this research are:

i. Provide a framework to select a 'best' turbulence model more systematically for a given complex flow.

ii. 'Map' existing flow and model classes more fully against quantitatively documented flow types.

iii. Use a simulation database as well as experimental data so as to quantify dominant physical parameters to have a better understanding of the manner in which these parameters can determine complex flow properties and modelling.

A set of proposals for future works is then presented based on the achievement of these objectives.

1.3 Thesis structure

Chapter 2 revisits current single-point models of turbulence which are used to compute different types of flow. It describes the need for various closure levels, ranging from the zero-equation to more complex models. Also, the validity of the models based on the localness of turbulence in space and time is discussed. The state-of-the-art guidelines for predictions are reviewed at the end.

Chapter 3 briefly describes the several different types of simple turbulent flow chosen in order to quantify the statistical parameters, and gives general information on their simulations (both DNS and LES) and experiments. The specific purposes for the analysis of their simulation datasets and experimental data, and therefore the domains of interest, are also mentioned.

Chapter 4 deals with the methods used to obtain quantitative parameter estimates, which include defining the regions of interest, and testing the reliability of the quantification technique. Apart from that, the extraction of the higher-order correlations from the master-mode is explained.

Chapter 5 mainly consists of the results concerning both localness (i.e. $\tilde{L}_X$ and $\tilde{T}_L$) and structural parameters (i.e. $\tilde{S}$ and $\tilde{G}$) from the analysis on the various turbulent flow types described in Chapter 3, and of the comparison between the results and previous mathematical-empirical estimates.

Chapter 6 shows the close relationship between the prediction methods and the quantitative flow parameters and, in some cases, discusses the flexibility in choices of different types of closure. The chapter investigates if the gap between the state-of-the-art guidelines and the practical turbulent cases that are not exactly classified by fixed (i.e. readily available) combinations of the localness-structural parameters can be bridged.

The classification of underlying flow regimes (UFRs), and thence application challenges (ACs) are, among other topics, presented in Chapter 7, and reveal whether or not the localness-straining information is useful in determining the need for zonal-modelling. The latter requires some discussion on the interplays between localness ($\tilde{L}_X$ and $\tilde{T}_L$) and the strain ($\tilde{S}$). The conclusions and the considerations for future work, are outlined in Chapter 8.

2
Introduction to the turbulence models

There are two basic objectives in the application of computational fluid dynamics (CFD). The first is to generate scientific understanding of the mechanisms involved in, and the behaviour of, fluid flows of interest. Being able to design the hardware for engineering devices or systems is the second objective. An example of such a design is that of aircraft and components configured to maximise the aircraft performance by control of the flow through or around the aircraft. Thus, a CFD technology development goal is an improved ability to predict the flows characteristic of engineering devices. Progress should be made in order to produce a truly predictive computational scheme, and reduce fluid flows (especially complex turbulent flows) to computable phenomena [3-6]. Since the use of full governing Navier-Stokes equations is normally computationally impractical for the prediction of turbulent flows, a hierarchy of turbulence models is used to model fluctuations inherent in these equations.

Thus, these closure models are constructed based on certain assumptions and objectives which are illustrated in §2.1-2.7. Methods of calculation, inputs and outputs of the models are also reviewed. Then the appropriate choice and use of turbulence models are generally discussed in §2.8.

2.1 Zero-equation models

The idea of using a mixing length describing the turbulent mixing and therewith associated diffusion coefficient, μ_t, was proposed by Prandtl [7].

This model is referred to as the zero-equation model or algebraic model, since at this closure level, the velocity and length scales are modelled as functions of the local mean flow variables. Prandtl suggested, with dimensional reasoning,

$$\mu_t = \rho l_m{}^2 \left| \frac{d\bar{u}}{dy} \right| \tag{2-1}$$

where l_m, which is a characteristic distance over which packets of fluid are transported by turbulence, need to be tuned for different flows. The turbulence or eddy viscosity μ_t defined in (2-1) can then be used to determine a local relation between the shear and mean gradient,

$$\tau = \nu_e \left(\frac{\partial \bar{u}}{\partial y} \right),$$

(where $\nu_e = \mu_t / \rho$ which is always positive) in typical unidirectional non-uniform shear flows, provided that the turbulent kinetic energy is satisfied. Some workers suggest that linear stress-strain (or linear flux-gradient) relationship is valid for any kind of strain, for example:

$$\sigma_{ij} = -\nu_e \left(\frac{\partial \bar{u}_i}{\partial x_j} + \frac{\partial \bar{u}_j}{\partial x_i} \right), \tag{2-2}$$

(where $-\sigma_{ij}$ is the Reynolds stress), although a number of experimental as well as numerical researches on highly distorted or inhomogeneous turbulence (e.g. pipe bends or convective boundary layers) show the limitations of such an assumption [8]. This basic, so-called mixing length model, therefore, is accurate only for a number of flows for which the mixing length parameters have been correlated, and hence, is not a universal model.

For boundary layers, it has been proposed in [9] that

$$l_m = \kappa y \left[1 - e^{-y^+ / A_o{}^+} \right], \quad A_o{}^+ = 26$$

This modification of Prandtl's mixing length model provides better prediction of τ_{xy} as the wall is approached - DNS data shows τ_{xy} is proportional to y^4 as it tends to zero. A rather simpler model defines the mixing length near the solid surface (or wall) $\left(y \le \delta /5 \right)$, as;

$$l_m \approx \kappa\, y,$$

where δ is the boundary layer thickness, and the von Karman non-dimensional constant $\kappa \approx 0.4$. This is an instant of how to take care of boundary condition in the viscous sublayer region (i.e. at a solid surface). The near wall region is nearly universal where the law of the wall is valid. This justifies making the mixing length l_m independent of the flow type. This finding, where the normal velocity fluctuations are blocked by a solid surface at $y = 0$, and are reduced in scale by the increased shear $\left|\partial_y \bar{u}\right|$ near the surface, is interesting because the length scales $L_X^{(2)}$ of the eddy motions of the normal velocity component are of the order y, the distance from the surface. However, this is only valid, firstly at a high Reynolds number when there is a full spectrum of eddies [10], and secondly if the other straining effects (which are corresponding to the fluctuating velocity gradients) considered in turbulent kinetic energy equations are ignorable [1]. At a very high Reynolds number, the scale l_m is approximately the length scale $L_X^{(2)}$ Although this length scale over which the eddies are correlated decreases near the wall (due to damping process), at each level y it is of the order of l_m over which the mean velocity gradient changes. This suggests that the eddy structure, and hence l_m near the rigid surface is not just a local function of $\partial \bar{u}/\partial y$, but also is affected by the presence of the surface. This effect is considered in some turbulence models, e.g. [11] and [12], for Reynold stresses σ_{ij} near the wall.

Clauser [13] introduced a definition for the eddy viscosity in the outer part of the defect layer as

$$\mu_{t_o} = \alpha \rho U_e \delta^*$$

where U_e is the velocity at the edge of the layer and δ^* is the displacement thickness.

Klebanoff [14] introduced a further multiplier to account for intermittency in the boundary layer:

$$F_{kleb} = \left[1 + 5.5 \left(\frac{y}{\delta} \right)^6 \right]^{-1}$$

More recently, for non-uniform shear flows, [15] and [16] defined the mixing length l_m, given by

$$l_m \sim u_o / S,$$

where u_o is the energy containing the eddies velocity scale, and S is the mean shear, as the length scale over which the vertical velocity components and pressure fluctuations are correlated [15; 16].

The mixing length models do not involve evolution equations at all. Therefore, they should not be applied when the history effects are important, as in the separated compressible flows. In this type of flow, the distance to reattachment seems to be consistently overpredicted [17].

Among other zero-equation models are the Cebeci Smith model [18], and that of Baldwin-Lomax [19]), both of which are well known and much used [20].

Zero-equation models are attractive due to their simplicity and robustness, and have been further developed especially for (aeronautical) boundary layer flows, which incorporate the above modifications in attempts to further generalise the model. In spite of these advantages, it should be noted here that a zero-equation model is incomplete in the sense that the length scale involved is post-dictive, since it has been taken from some *ad hoc* empirical argument, and that it requires some physical or numerical adaptation where the mean shear tends to be zero.

2.2 One-equation models

Prandtl [21] proposed that the velocity scale could be determined using a modelled $k-\text{equation}$. This idea has been generalised to that of one-equation models in which only one of the two quantities from which the eddy viscosity μ_t is obtained is determined from a transport equation. In general, greater accuracy is achieved by one-equation models for a number of specific flows in comparison to zero-equation models for only a modest increase in cost.

In $k-\text{equation}$ based closures, the length scale needs to be taken from some *ad hoc* empirical argument, due to difficulty in accounting for rapid changes in length scale specification, for example shear layer behind an airfoil or multiple jet mixing. This serious problem is a shortcoming shared with zero-equation models, and has empirically been proved to seriously limit the usefulness and generality at the $k-\text{equation}$ model level. A perhaps better alternative to this type of model is suggested in [22], i.e. one-equation models based on a transport equation for μ_t itself. In principle another choice would be to consider a transport equation for length scale, as is done in the two-equation models case.

2.2.1 Baldwin-Barth model

The Baldwin-Barth model [23] seeks a solution of a single transport equation for the turbulent Reynolds number. At this level of closure, the transition phase from laminar to turbulent flow is set by the user through a multiplier to the production term. There are seven closure coefficients, two empirical damping functions, and a functional form for length scale. This model avoids the need for specification of length scale.

2.2.2 Spalart-Allmaras

This model, in which a solution of a single transport equation for a non-dimensional eddy viscosity is sought, is referred to as the Spalart-Allmaras

model [24]. It is quite similar to that of Baldwin-Barth but with the addition of a non-viscous turbulence destruction term dependent upon distance from the wall. Being a sophisticated transition model, the transition location is set by the user to provide a smooth transition. There are 12 closure coefficients, and two damping functions.

2.3 Two-Equation Models

The closure level which has proved to give a reasonable generality for engineering predictions in a great variety of flows, is referred to as the level of two-equation models. In fact, it is the lowest level of closure in which history effects can be accounted for in some reasonable manner.

Both the velocity and length scale, or some alternative pair of quantities that form the eddy viscosity are determined by transport equations. It was Kolmogorov [25] who used the angular velocity ω with the inverse timescale dimension, along with the kinetic energy k, for the first two-equation model formulation. Since then, the $k-\text{equation}$ has been used as a transport equation for the velocity scale for practically all models of two-equations.

It is interesting to note in this context, that several other alternative complementing quantities have been considered, which are the dissipation rate ε, the length scale l itself, and a timescale, for instance. So far, ε has been the most widely used, along with some other quantity, and is usually derived from the $\varepsilon-\text{equation}$.

At this level of closure the poor description of streamline curvature effects and system rotation or rotational mean flows form one of the problems of the standard two-equation models. This is partly caused by the linearity of the Boussinesq hypothesis resulting in an independence of the rotational, antisymmetric part of the mean velocity gradient tensor in this relation. The other main problem is the locality of the stress anisotropy description, as follows, from the Boussinesq hypothesis,

$$a_{ij} = -2\frac{\nu_t}{k}S_{ij}$$

The abandoning of the eddy-viscosity hypothesis altogether would be a natural solution for these problems, as in the formulation of the Reynolds stress transport models. Nevertheless, the considerable success of two-equation models for engineering flow predictions, and their relative ease of use and numerical robustness have motivated a strong interest in the continued use of this level of closure in computational fluid dynamics.

2.3.1 Standard High Reynolds Number $k-\varepsilon$ Model

In the development of the $k-\varepsilon$ model, much of the essential work was done in the seventies, for instance, by Jones and Launder [26; 27]. At this level of closure, the third moment in the turbulent kinetic energy equation has been expressed in terms of local gradient, and the model equation for k has been rescaled to model the dissipation rate (i.e. ε) transport equation;

$$\rho\bar{u}_k\frac{\partial}{\partial x_k}k=-\rho\overline{u_k'u'}_l\frac{\partial\bar{u}_l}{\partial x_k}-\frac{\partial}{\partial x_k}\left(\frac{\mu_t}{\sigma_k}\frac{\partial k}{\partial x_k}\right)-\rho\varepsilon$$

and

$$\rho\bar{u}_k\frac{\partial}{\partial x_k}\varepsilon=-\rho\overline{u_k'u_l'}\frac{\partial\bar{u}_l}{\partial x_k}\left(C_{\varepsilon_1}\frac{\varepsilon}{k}\right)-\frac{\partial}{\partial x_k}\left(\frac{\mu_t}{\sigma_\varepsilon}\frac{\partial\varepsilon}{\partial x_k}\right)-C_{\varepsilon_2}\rho\frac{\varepsilon^2}{k}$$

respectively. The expression

$$-\rho\overline{u_i'u_j'}=\mu_t\left(\frac{\partial\bar{u}_i}{\partial x_j}+\frac{\partial\bar{u}_j}{\partial x_i}-\frac{2}{3}\delta_{ij}\frac{\partial\bar{u}_k}{\partial x_k}\right)-\frac{2}{3}\rho k\delta_{ij},$$

where

$$\mu_t=C_\mu\rho\frac{k^2}{\varepsilon}\ :\ \ell=C_\mu\frac{k^{3/2}}{\varepsilon}$$

known as the (generalised) Boussinesq hypothesis, is the main assumption made at this level of closure (as well as in other eddy viscosity models).

The unknown coefficients in both equations have been appropriately calibrated in a number of turbulent flows of practical importance. Critical reviews and evaluations of the terms have been done, for instance by Rodi and Mansour [28]. If the coefficients are determined by analogy with the isotropic decay of grid turbulence and the assumption of equilibrium in a log-layer, then for instance;

$$C_{\varepsilon_1} = 1.44,\ C_{\varepsilon_2} = 1.92,\ \sigma_k = 1.0,\ \sigma_\varepsilon = 1.3,\ \text{and}\ C_\mu = 0.09.$$

For turbulence which is approximately Gaussian, and with small length scales, the diffusion mechanism is used to model the transport term

$$\frac{\partial}{\partial x_k}\left(\frac{\mu_t}{\sigma_k}\frac{\partial k}{\partial x_k}\right)$$

in the equations for fluxes [1; 10]. Other types of modelling techniques are required in the conditions involving large scale eddies [29].

Unfortunately, the standard model k-ε ignores viscous terms necessary to integrate through the boundary layer. Moreover, the dissipation rate ε is determined from a heuristically derived equation (see [30]).

In turbulence near a wall, [31] and [32] suggested that k increases towards the wall in proportion to $k \sim u_*^2\left[-\ln\left(x_2/l_s\right)+A\right]$, where u_* is wall friction velocity, $A \sim 10$ and l_s is the depth of the surface layer $l_s \sim \delta/10$. Thus, the highest value of k, which takes place where $x_2 \sim x_{20} \sim \nu/u_*$, increases with the Reynolds number Re (in proportion to $-\ln\left(1/Re\right)$). This sensitivity (which may lead to over- or under-prediction) of the ratio $k\left(x_2\right)/u_*^2$ to Re) can be circumvented (in shear flows) by substituting the fraction of turbulent

kinetic energy $\overline{u_2^2}$ as the $'k'$ variable in $k-\varepsilon$ models; near the 'wall' $\overline{u_2^2}/u_*^2$ is approximately constant outside the viscous sublayer zone as Re varies [1].

2.3.2 Renormalization Group Theory (RNG) Derived $k-\varepsilon$ Model

In theoretical physics, RNG theory is known as the process of systematically removing small length scales and rescaling the transport equations. In principle, this should allow analytical derivation of the $k-\varepsilon$ models. The RNG $k-\varepsilon$ model employs standard $k-\varepsilon$ transport equations with modified constants, in particular C_{ε_1} becomes a function of strain rate

$$C_{\varepsilon_1} = 1.42 - \frac{\eta\left(1-\frac{\eta}{\eta_o}\right)}{1+\beta\eta^3}$$

$$\eta = S\frac{k}{\varepsilon}$$

$$S = \left[\frac{\rho}{\mu_t}\left(-\rho u_i' u_j' \frac{\partial \bar{u}_i}{\partial x_j}\right)\right]^{1/2}$$

Other constants (*i.e.* $C_{\varepsilon_2}, \sigma_\varepsilon$, and C_μ) retain values very similar to empirically determined ones in the standard model.

Great claims (probably commercial) have been made regarding this model, although it is just another $k-\varepsilon$ model with tuned constants. In other words, it still relies upon isotropic eddy viscosity, consisting of a modelled $\varepsilon-$equation.

2.3.3 High Re $k-\varepsilon$ Model – Near Wall Treatment

Since the viscosity changes significantly when approaching the wall, it is necessary to integrate its term through the boundary layer. The boundary layer may be represented by law of the wall

$$\frac{\bar{u}}{u^*} = \frac{1}{k} ln\left(Ey^+\right) \qquad 20 < y^+ < 300$$

Differentiating this equation yields the velocity gradient

$$\frac{d\bar{u}}{dy} = \frac{u^*}{\kappa y}$$

Assuming turbulence is in local equilibrium, from the transport equation for turbulent kinetic energy, one has

$$< \text{Production} > \cong < \text{Dissipation} >$$
$$-\rho\overline{u_i' u_j'} \frac{d\bar{u}}{dy} \cong \rho\varepsilon$$

Substituting for ε from eddy viscosity definition and introducing the Boussinesq assumption yields

$$\mu_t = \frac{C_\mu \rho k^2}{\varepsilon}$$
$$-\rho\overline{u_i' u_j'} = \mu_t \frac{d\bar{u}}{dy}$$
$$-\overline{u_i' u_j'} \cong C_\mu{}^{1/2} k$$

This model makes use of experimental evidence of constant shear stress across the boundary layer in the vicinity of the wall (*i.e.* $\tau \cong \tau_w$). Note that this is just one example of a near wall treatment.

2.3.4 Low Reynolds Number $k-\varepsilon$ Model

The low Reynolds number $k-\varepsilon$ model considers, along with the viscous diffusion terms, damping terms for μ_t and ε in k and ε transport equations. The wall damping is required such that

$$\mu_t \to \mu_{laminar} \text{ as } y \to 0$$

A turbulent Reynolds number is given by

$$\mathrm{Re}_t = \frac{\rho}{\mu}\frac{k^2}{\varepsilon} \quad \text{or} \qquad \mathrm{Re}_y = \frac{\rho\sqrt{k}y}{\mu}$$

A flow is said to be of high Reynolds number when $\mathrm{Re}_t > 100.$, thus defining viscosity as

$$\mu = \mu_{laminar} + f_\mu \mu_{turbulent}$$

where

$$f_\mu \to 1 : \mathrm{Re}_t \to 100$$
$$f_\mu \to 0 : \mathrm{Re}_t \to 0$$

Note that f_μ is designed to mimic the effect of molecular viscosity on shear stress.

The models discussed in sections 3.1 to 3.3 are referred to as eddy viscosity models. They assume a direct and linear relationship between Reynolds stress and rate of strain. Note that in Reynolds stress budgets, the mean velocity gradient (i.e. the independent terms in the Boussinesq hypothesis for the stress tensor) helps to predict the time rate of change of the stress, but not directly its magnitude [33]. It is also worth noting that several studies have shown the limitations of the assumption that for any kind of strain, stress-strain or flux-gradient have linear relationships [8]. This suggests that there are cases where these models are not accurate. The study by Murakami et al., for example, has shown how eddy viscosity models can over-predict the straining's effect on the growth of k when the scale of the eddy turbulence is relatively large near bluff bodies [34]. Another limitation is when the turbulence Reynolds number increases above around 10^4, where there is a significant change in near wall turbulence structure such that the closure models (i.e. the widely used $k-\varepsilon$ model) have to be applied in a thin layer, where $0 \le x_2 \le x_{2w}$ [1; 35].

2.3.5 The $k-\omega$ Model

The $k-\omega$ model of Wilcox [22] is widely used in industry, and has a remarkable property where it is usable near solid boundaries without a need for wall functions or damping. This is because the model, with strain modification, produces extra production of dissipation near solid boundaries. The model is given by

$$\frac{\partial}{\partial t}k+\bar{u}_j\frac{\partial}{\partial x_j}k=2\nu_T|S|^2-k\omega+\frac{\partial}{\partial x_j}\left(\left(\nu+\frac{\nu_T}{\sigma_k}\right)\frac{\partial}{\partial x_j}k\right)$$

$$\frac{\partial}{\partial t}\omega+\bar{u}_j\frac{\partial}{\partial x_j}\omega=2C_\mu C_{\omega 1}|S|^2-C_{\omega 2}\omega^2+\frac{\partial}{\partial x_j}\left(\left(\nu+\frac{\nu_T}{\sigma_\omega}\right)\frac{\partial}{\partial x_j}\omega\right)$$

$$\nu_T=C_\mu k/\omega.$$

Note that the $k-$equation is modified by replacing ε with $k\omega$, while the $\omega-$equation is somewhat analogous to the $\varepsilon-$equation. The constants $\sigma_k=\sigma_\omega=2,\ C_\mu=0.09,\ C_{\omega 1}=5/9,$ and $C_{\omega 2}=5/6.$

The turbulent kinetic energy k in the viscous sublayer region increases with wall distance, while the dissipation rate ε decreases. Since the extra term in the $k-\omega$ model's solution is a source of dissipation, a larger ε is produced.The details about the properties of the $k-\omega$ model can be found in [22] and [12] .

2.4 Reynolds Stress Transport Models

Models in which the eddy-viscosity hypothesis is removed altogether, are referred to as Reynolds stress transport models (RSMs) or Differential Stress Models. These models are scalar equations formulated for the six components of the Reynolds stress tensor. The closure needs to be achieved by (at least) an equation for the length scale, or other equivalent equation, such as the most generally used equation for the kinetic energy dissipation rate. Since the Reynolds stress is the stress of motion rather molecular stress, the basis of this

approach with six equations for the energy distribution is seen as a strong emphasis on the description of the dynamics of the large scales only. In this regard, the small scales are more isotropic than the large scales, and more indirectly affected by imposed strain, rotation and geometrical constraints.

Much of the development of Reynolds stress models occurred during the 1970's and was done, for example, by Launder, Reece, and Rodi, and is still continuing for more advanced forms. Craft and Launder's version of RSM [36], for instance, includes the dependence of the initially non-isotropic turbulence (i.e. whether or not it may tend to isotropy) on how its spectrum is generated. However, the first model was devised by Rotta in 1951 [20].

By avoiding the Boussinesq assumption and its weaknesses, considerably better performance should be possible, compared to two-equation models. The major challenge at the Reynolds stress model level is the difficulty in the rotational effects description. The improvements to the description have been made by analysing generalisations where further transport equations are incorporated into the model.

The Reynolds stress transport equation is given by

$$\frac{\partial}{\partial x_k}\left(\rho\bar{u}_k\overline{u_i'u'}_j\right)=-\left(\rho\overline{u'_ju'}_k\frac{\partial\bar{u}_i}{\partial x_k}+\rho\overline{u_i'u'}_k\frac{\partial\bar{u}_j}{\partial x_k}\right)-\frac{\partial}{\partial x_k}\left(\rho\overline{u_i'u'_ju'_k}\right)$$
$$-\left[\frac{\partial}{\partial x_i}\left(\overline{pu'_j}\right)+\frac{\partial}{\partial x_j}\left(\overline{pu'_i}\right)\right]+\overline{p\left(\frac{\partial u'_i}{\partial x_j}+\frac{\partial u'_j}{\partial x_i}\right)}-\varepsilon_{ij} \qquad (2\text{-}3)$$

As in the $k-\varepsilon$ equations (§2.3.1-§2.3.4), simplifications have to be made to ensure a soluble set of equations. Other than production, all terms on RHS of (2-3), consist of six individual transport equations plus dissipation rate terms, require modelling in order to close the set of equations. Several workers (i.e. Lumley et al. [37] and Wyngaard [38]) have proposed equations for third-order correlations for at least some flows of practical importance at low Reynolds numbers. A further three equations are required for the scalar fluxes (i.e. Reynolds heat fluxes).

This more advanced type of closure (i.e. second order closure) is superior for flows where the Boussinesq assumption is known to fail, where the apparent stress and scalar fluxes $\sigma_{ij}, F_{\theta i}$ are not simply proportional to the local mean gradients; it involves the relations of two-point to one-point correlations and third order to second order moments [11; 36]. In these types of flow, the turbulence is less local, where the eddies develop rapidly enough and can be transported perpendicularly to the streamlines fast enough.

However, such a level of transport modelling gives greater computational burdens, and is less robust. Furthermore, there is no single unifying RSM. These shortcomings turn RSM into a complex and expensive model to solve. Another disadvantage is that it (as well as other current transport-based models) does not represent the sensitivity of the ratio $k\left(x_2\right)/u_*^2$ to the value of Re in the case of turbulent flow near a wall at high Reynolds number (i.e. $Re \gtrsim 10^4$)[35][39], where there is a significant change in the near-wall turbulence structure.

2.5 Algebraic Reynolds Stress & Non-Linear Eddy Viscosity Models

Unlike the two-equation models, the algebraic Reynolds stress models do not make use of the standard Boussinesq hypothesis nor the concept of an eddy viscosity. However, they are still based on two transport equations for, say, k and some auxiliary quantity. This simplified version of the RSM model seeks a generalisation of the constitutive-like relation between the stress anisotropy and the mean flow quantities $\left(S_{kl}, \Omega_{kl}\right)$. This approach gives a better description of e.g., rotation-associated effects on the turbulence, than that used at the level of two-equation closure does.

Rotta (1976) proposed that the transport terms could be modelled by analogy to the transport equation for turbulence kinetic energy, *i.e.*

$$< \text{convection} - \text{diffusion} >_{u_i u_j}$$

$$\approx \frac{\overline{u_i' u'}_j}{k} < \text{convection} - \text{diffusion} >_k$$
$$= \frac{\overline{u_i' u'}_j}{k} < \text{production} - \text{dissipation} >_k$$

Note that the Reynolds stress transport equation considered here is that in the case of locally homogeneous turbulence where the derivatives of the statistics (e.g. $\frac{\partial}{\partial x_k}\left(\rho \overline{u_i' u_j' u_k'}\right)$), not the statistics of the derivatives in the RHS of (2-3) vanish (i.e. the turbulence is in equilibrium).

Rearrangement yields a set of coupled *algebraic* equations for the six Reynolds stress correlations. In spite of being computationally attractive and successful for some flows (especially involving body forces) the model is not widely employed.

Alternatively, a higher order stress-strain relationship may be derived where the coefficients are functions of strain or vorticity invariants. Such models are referred to as *explicit algebraic* stress models, or non-linear eddy viscosity models.

2.6 Structural Models

The turbulence structural closure involves multi-scale modelling. The distorted structural model (DSM), for example, is generally based on the rapid distortion theory (RDT) estimates as well as experimental information on turbulent eddy structure that might be used to modify or moderate the constants in eddy viscosity μ_t, rapid pressure-strain, and dissipation rate ε closure of existing transport models [5]. This type of model incorporates a 3-eddy picture which consists of $u'(\text{coherent}), u'(\text{turbulent})$, and $u'(\text{subrange})$. Note that the usual picture of eddy involves single $u'(\text{turbulent})$ only, as could be seen in the standard Reynolds decompositions.

A more thorough discussion on the hierarchy of turbulence models may be found in [20; 40-45], with [46-51] giving more elementary references for the relevant mathematical foundations.

2.7 Large Eddy Simulation

A numerical technique called large eddy simulation (LES) was formulated in the late 1960s and is used to solve the governing equations for turbulent flows. Large eddy simulation was first used for meteorological calculations and predictions, and then began to be widely accepted in the field of engineering during the 80s and 90s.

Small eddies are self similar and have universal character, while larger eddies are dependent on the flow geometry. This is a deduction of the self similarity theory proposed by Kolmogorov in 1941. It became a practice, then, to model the effect of small eddies on larger ones, and solve only for the large eddies explicitly. Thus, in LES the small universal scales, called subgrid-scales of motion, are modelled using a subgrid-scale (SGS) model, while the equation of motions is low-pass filtered.

A filtered one dimensional variable $\tilde{u}$ is defined by

$$\tilde{u} = \int_{-\infty}^{\infty} G\left(x - x'\right) u\left(x'\right) dx',$$

where typical filter kernels $G(z)$ have a defined filter width Δ and include the Gaussian

$$G(z) = \frac{\exp\left(-z^2/\sigma^2\right)}{\sigma\sqrt{\pi}}$$

with $\sigma = \frac{\Delta}{\sqrt{6}}$, and the top hat filter

$$G(z) = \frac{1}{\Delta} \text{ for } z < \Delta, \text{ and } G(z) = 0 \text{ for } z \geq \Delta.$$

This filtering operation can be applied to the original Navier-Stokes equations.

Some recent development of LES includes deconvolution approaches to recovering the small scales, and the popular detached eddy simulation (DES) approach, which switches between LES and Reynolds-averaged Navier-Stokes (RANS) equations according to local criteria. These approaches have been discussed in, e.g., reference [52].

Large eddy simulation requires more effort than those methods that solve the RANS equations alone, such as those used at one/two-equation model levels, but less computational effort than direct numerical simulation (DNS).

2.8 Guidelines for Use of Turbulence Models[3]

Attempts have been made to classify the turbulence model applications based on types of engineering and environmental complex flow. Each classification is meant for specific groups of user, such as those involved in routine engineering as well as those in CFD calculations for industrial design development. Examples of the intentions of such classifications are as devices for achieving high-quality industrial CFD simulations, recommendations for pragmatic procedures in turbulence predictions, and guides for improvements of the "level of trust that can be placed in industrial CFD calculations" [53]. In general, their goal is to serve as a practical guide for a selection, application and expected capabilities of one- or two-point closures using modelled RANS equations in turbulence predictions and simulations [1; 2; 6; 53-56].

One of the most basic assumptions taken into account in the application of the turbulence models (in computing the mean flows and other statistics) is that the velocity fluctuation magnitude, and hence, the magnitude of momentum $-\sigma_{ij}$ are usually much weaker than the typical changes in mean velocity, and thus, mean momentum fluxes [1];

$$\Delta\left|\overline{u_i u_j}\right| \ll \Delta\left|\overline{u}_i \overline{u}_j\right|,$$

[3] Much of the work in this section and Chapter 4 was presented in [57].

where Δ denotes 'changes'. Thus the gradients of the Reynolds stress, $\partial_j \sigma_{ij}$, only have a significant effect on the mean flow when the mean accelerations $\partial_j^2 |\overline{u}_i \overline{u}_j|$ are small and the turbulence is changing slowly (where the inertia plays an important role) along the mean streamlines.

Interestingly, although $\partial_j^2 |\overline{u}_i \overline{u}_j|$ is large and there is a decrease in the exchange of energy between motions on different length scales when a blocking rigid surface is present, some workers assume that turbulence models are valid in the case of turbulence near a wall. This is done carefully by taking the reduction of the energy exchange between different wave lengths into account when defining the parameters of their model (e.g. [36]).

A combination of 'modelling' and 'simulation' approaches is an alternative for some problems where models are not currently satisfactory (e.g. [58]). Note that the 'simulations' and real time predictions are two different types of modelling. The former require an ensemble averaging of flow quantities over a sufficient number of 'turn-over' timescales to produce mean flow statistics. These are truly random eddy simulations, whether direct numerical simulations (DNSs), or large eddy simulations, LESs (see §2.7). In the latter case, information about turbulent quantities as they develop in space-time is arbitrary, in particular transient realisations of the flow can be obtained. These types of prediction are reviewed in [52] (see also [59]; [60]; [61]).

2.8.1 Stanford 1981 Matrix of Computations

The classification of methods/models for calculating turbulent flows in the matrix form was constructed as a result of the Stanford University Conference on Complex Turbulent Flows (CTFs) in 1981 [6]. The models considered are that of integral, prescribed eddy viscosity or length scale, Boussinesq, algebraic, Reynolds stress, as well as two-point closure. They are classified following the various types of both compressible and incompressible flows which are represented by 54 test cases.

Certain conclusions and trends were successfully found and reported along with such classification, and are summarised below;

1. In calculating the homogeneous turbulent flows, the RSMs were only slightly worse than the two-point closure scheme, but the results of the one-point closure scheme using an algebraic model were significantly worse.

2. The uncertainty of the results involving the flat-plate boundary layer (in compressible flow with insulated and variable wall temperature) computations is about ±10%.

3. Generally, the accuracy of results involving separated flows was significantly worse than for corresponding attached flows. In the case of a flow involving separation, the RSM model did no better than the less sophisticated methods (This conclusion was similar for free-shear layers).

4. The RSMs showed some advantages over other models.

The Stanford 1981 matrix of computations, however, is just an approximate guide, without a concrete suggestion for a best selection of models for given turbulent flows. There is a need for more systematic classification, since it has been confirmed in CTFs, that every method has its strong and weak points, and had no significant universality, nor was it proved to be universally bad.

2.8.2 ERCOFTAC‘s Knowledge Based "Best Practice Guidelines"

These guidelines [54] have been written and edited by making use of extensive consultation with CFD code vendors, code developers, academic experts and code users and this gives the guidelines wide support. They form a baseline reference for those involved in routine engineering CFD, which provides CFD users with a well established blueprint as a practical guide for the selection, application and expected capabilities of models. They are intended

as best practice advices for achieving high-quality industrial CFD simulations using the RANS equations. The editors claimed that the guidelines offer roughly those 20% of the most important general rules of advice that cover roughly 80% of the problems likely to be encountered. Hence, users who follow the advice given can be expected to avoid the most common pitfalls in CFD simulations.

The guidelines also provide a useful compilation of relevant information on the most important issues relevant to the credibility of CFD simulations, especially with regard to the most common sources of errors and uncertainties in CFD. Simple statements of advice are given for every aspect considered, which provide clear and generally accepted guidance for the CFD user in industrial applications.

The scope of these guidelines includes single-phase, compressible and incompressible, steady and unsteady, turbulent and laminar flow with and without heat transfer.

The ERCOFTAC Best Practice Guidelines includes eight carefully selected test cases which show:

1. important physical effects: strong swirl, heat transfer, flow in rotating components (turbomachinery), compressible flow, and unsteady flow.

2. numerical errors, grid dependency, spatial discretisation, temporal discretisation convergence, turbulence model, wall function, application uncertainty (boundary conditions and geometry).

3. some comparison with experimental data or to an analytic solution.

Some of test cases which deal with the choice of turbulence models for certain type of flow will be fully discussed in Chapter 7.

Test cases	Models compared	Results
T-Junction between main and auxiliary pipe	RSM *vs* $k-\varepsilon$ model	1. On the finest mesh, RSM is better. This is because it confirms the presence of the swirling flow structure. 2. On a too coarse mesh, $k-\varepsilon$ model is better.
Natural convection flow in a square cavity (modelling error)	Incompressible flow model with a simple Boussinesq approximation *vs* Low Mach no. compressible flow model (which avoids Boussinesq approximation)	1. Small temperature difference case: On a sufficiently fine mesh, both models are in good agreement with reference solutions. 2. Large temperature difference case: Only the Low Mach no. compressible flow model is acceptable based on reference solutions.
Sudden pipe expansion (modelling accuracy)	The standard $k-\varepsilon$ model alone *vs* The standard $k-\varepsilon$ model coupled to a length scale limiting device	The standard $k-\varepsilon$ model coupled to the length scale limiting device is better in terms of prediction of heat transfer in flow re-attachment regions.

Table 2-1 Some test cases in the ERCOFTAC Best Practice Guidelines

2.8.3 Universal or Zonal Modelling Strategies

It has been made clear that there is nothing 'good' or 'bad' about more or less universality in modelling, and since then, it has been generally accepted that there is no such thing as a 'universal' turbulence model [55]. This consensus has been generally accepted over the past 20 years or so and calls for pragmatic procedures such as 'zonal' modelling [53; 55; 56].

In order to form the basis of a predictive decision-making process for zonal modelling, it was proposed that both the length scale L and/or the timescale

T may be used to define zones so that constants in a baseline model can be adjusted from one zone to the next. An example could be a boundary layer with a high Reynolds number, where there is a full spectrum of turbulence. This zone is defined by the size of the eddy motions of the vertical fluctuation which are of the order of x_2, the distance from the wall [10].

A suggested scheme is [56]:

1. Obtain solution with baseline model using standard constants.
2. Identify deficiencies in veracity of solution.
3. Determine from solution with baseline model fractional changes in L to form the basis of decisions in determining zone boundaries.
4. Make changes to model constants, either on an *ad hoc* basis, or by making them functions of simple algebraic relationships such as those used to quantify the effects of extra strain rates, such as

$$l = l_o\left(1+\sigma\frac{e}{\partial U/\partial y}\right).$$

5. Use simple ordinary differential equations, which show that

$$V_k = \frac{\overline{p'v'}/\rho + \overline{kv'}}{k},$$

and

$$V_\tau = \frac{\overline{p'u'}/\rho + \overline{u'v'^2}}{\overline{u'v'}}$$

to take account of non-local effects.

It is worth noting that, in spite of the assertion made by Kline [55] about the non-universality of turbulence models [55] (which may lead to the idea of

zonal modelling), a general conclusion made at the 1999 Isaac Newton Institute (INI) programme on turbulence is that turbulence is partly universal in some statistical measures and kinematic features, and has stronger tendency towards these at small scales, while at the large scales, eddy motions within particular types of turbulence have qualitative similarities [2; 61].

2.8.4 A 'Localness' Map of Turbulence Models

The map, proposed by Hunt and Savill [1], is more fundamental than, but complementary to, the recent "Best practice guidelines" for CFD produced by ERCOFTAC [54]. Various turbulence model types and each of their key assumptions, and how they may influence the accuracy of computations in various classes of flow have been examined. Table 2-2 shows the flow classes involved, with their estimated spatial and time localness parameters[4].

This map, which is based on characteristic statistical parameters derived from standard models, was developed from considerations of basic mechanisms of turbulence and the different types of statistical turbulence model. It was concluded that turbulent flows can generally be classified on the basis of straining, Gaussianity, as well as rapidity of change in time and space (relative to the turbulence time and length scales), into broad groupings, where for practical purposes different sorts of model are most suitable. More precisely, such classification indicates in principle whether or not types of turbulent flow can be approximately calculated with the current generation of 'CFD', one-point turbulence models, including those involving $k-\varepsilon$ and second order closure equations.

The 'localness' map is also based on the hypothesis that the standard one-point models are only strictly valid and likely to provide accurate predictions when the turbulence dynamics are local in time and space and when the turbulence characteristics are 'typical', e.g. with probability distribution close

[4] Detailed definitions are given in page 50-61.

to Gaussian such that $G \leq 1$, and only moderate degrees of anisotropy of velocity and length scale (away from the boundaries).

	Types of turbulent flow	$\tilde{L}_x$	$\tilde{T}_L^*$	$\tilde{G}$	$\tilde{S}$
(i)	Homogeneous stationary turbulence	<<1	$\lesssim 1$	<<1	-
(ii)	Homogeneous decaying turbulence	<<1	~ -1	0	-
(iii)	Strained turbulence	<<1	$\gtrsim 1$	0	$0 \leftrightarrow 1$
(iv)	Turbulent boundary layer				
	(near a wall)	~1/2	<<1	0	<<1
	(near outer boundary)	~1	~1	$\lesssim 1$	$\lesssim 1$
(v)	Free shear flows and separated flows	~1	~1	$\lesssim 1$	$\lesssim 1$
(vi)	Large scale free stream turbulence interacting with a boundary layer	$\gtrsim 1$	~1	0	$\lesssim 1$
(vii)	Turbulence near a free surface	~1	<<1	0	-
(viii)	Natural convection (no mean flow)	~1	<<1	~1	-
(ix)	Shock boundary layer interaction	$\gtrsim 1$	>>1	<<1	$\lesssim 1$
(x)	Trailing edge boundary layer-wake interactions	>>1	~1	<<1	$\lesssim 1$
(xi)	Jet impaction	~1	~1	<<1	$\lesssim 1$
(xii)	Turbulent flow over small obstacles	$\gtrsim 1$	$\gtrsim 1$	<<1	≤ 1
(xiii)	Swirling shear flows	~1	~1	<<1	$\gtrsim$ -1

Table 2-2 Hunt and Savill's estimation for spatial and time localness parameters reproduced from [1]

2.8.5 The ERCOFTAC 'QNet' CFD Knowledge Base

This knowledge base is a result of a four-year "EU Network on Quality and Trust in the Industrial Application of Computational Fluid Dynamics" project which involved the expertise of 43 participating organisations across Europe. Its main objective was to improve the level of trust that can be placed in industrial CFD calculations [53] by assembling, structuring and collating existing knowledge, encapsulating the performance of models underlying the current generation of CFD codes.

The knowledge base may serve as a main reference for the possible need for zonal modelling. Its challenges include a wide range of application areas which have been divided into the following application challenges (ACs);

1. external aerodynamic*s* – *aero-acoustic cavity, RAE M2155 wing, RAE 2822 airfoil, channel flow with wall injection, Ahmed body, L1T2 3 element airfoil, and AS28G wing-body-pylon-nacelle,*

2. combustion and heat transfer – *bluff body burner for CH4-HE turbulent combustion, thermocapillary flow in cylindrical liquid bridge, gas burner controlled by variable density and/or counterflow, generic bluff body combustion, airflow cyclic variations in IC engines, the confined TECFLAM swirling natural gas burner, and confined double annular jet,*

3. chemical and process, thermal hydraulics and nuclear safety – *buoyancy-opposed wall jet, induced flow in a T-junction, cyclone separator, buoyant gas air-mixing, mixed convection in a reactor, spray evaporation in turbulent flow, combining/dividing flow in Y junction, and downward flow in a heated annulus,*

4. civil construction and HVAC – *wind environment around an airport terminal building, flow and sediment transport in a laboratory model of a stretch of the Elbe river, air flows in an open plan air conditioned office, tunnel fire, aerodynamic analysis of the Great Belt Bridge,*

5. environmental flows – *flow and dispersion in the presence of an L-shaped building***,** *dense gas release over flat terrain with and without obstruction, urban scale problems, mesoscale wind flow and dispersion, boundary layer flow and dispersion over isolated hills and valleys,* and

6. turbomachinery internal flows – *low-speed centrifugal compressor, annular compressor cascade without clearance, pump turbine, annular compressor cascade with tip clearance, gas turbine nozzle cascade, draft tube, high speed centrifugal compressor, axial compressor cascade, turbine cascade with cooling holes, and steam turbine rotor cascade* [53].

It is recognised that each of these complex flows involves combinations of a number of Underlying Flow Regimes (UFRs) which are generic, well studied test cases capturing important elements of the key flow physics encountered in one or more ACs. The full set is:

1. free flows – *underexpanded jet, blade tip and tip clearance vortex flow, annular coaxial jets flow and mixing, and jet in a cross flow,*

2. flows around bodies – *flow behind a blunt trailing edge, flow past cylinder, flow around oscillating airfoil, flow around (airfoils and) blades (subsonic), flow around airfoils (and blades) A-airfoil (Ma=0.15, Re/m=2x106), flow around (airfoils and) blades (transonic), 3D flow around blades, and rotor/stator interaction,*

3. semi-confined flows – *boundary layer interacting with wakes under adverse pressure gradient - NLR 7301 high lift configuration, 2D boundary layers with pressure gradients (A), laminar-turbulent boundary layer transition, shock/boundary-layer interaction (on airplanes), natural and mixed convection boundary layers on vertical heated walls (A), natural and mixed convection boundary layers on vertical heated walls (B), 3D boundary layers under various pressure gradients including severe adverse pressure gradient causing separation, impinging jet, the plane wall jet, pipe expansion (with heat transfer), stagnation point flow, flow over an isolated hill (without dispersion), flow over surface-mounted cube/rectangular obstacles, 2D flow over backward facing step, 2D boundary layers with pressure gradients (B), bypass transition on a flat plate,* and

4. confined flows – *confined coaxial swirling jets, pipe flow - rotating, flow in a curved rectangular duct - non rotating, curved passage flow, swirling diffuser flow, developing channel flow with mass injection through wall, orifice/deflector flow, confined buoyant plume, natural convection in simple closed cavity, simple room flow, compression of vortex in cavity, flow in pipes with sudden contraction* [53].

These UFRs overlap with the simple flow types identified by Hunt and Savill [1] (see Table 2-2). This in principle allows UFRs to be located in the 'localness' map described in §2.8.4 [63], and shown in Figure 4-1 of Chapter 4.

One example of the UFRs that make up an AC is that of those involved around multi element airfoil. The possible flow regimes are:

1. 2D boundary layers with pressure gradients (iva,ivb,v).
2. 2D flow over backward facing step (v).
3. 3D boundary layers under various pressure gradients including severe adverse pressure gradient causing separation (iva,ivb,v).
4. Stagnation point flow (ix).
5. Flow behind a blunt trailing edge (x,v).
6. Flow around airfoils (subsonic and transonic) (vi).
7. Boundary layer/wakes interaction under negative pressure gradient (x,v).
8. Shock/boundary-layer interaction (ix).
9. Flow around oscillating airfoil (generally consists of a certain combination/s of the above flows).
10. Laminar-turbulent boundary layer transition.
11. Bypass transition on a flat plate.

(Note that the roman numerals beside each UFR refer to a particular flow type described in Table 2-2, §2.8.4. A full list of UFRs and ACs can be found in Table 2-3)

		Underlying flow regimes
1	(1-01)	Underexpanded jet
2	(1-02)	Blade tip and tip clearance vortex flow
3	(1-05)	Jet in a cross flow
4	(1-04)	Annular coaxial jets, flow and mixing
5	(2-01)	Flow behind a blunt trailing edge
6	(2-02)	Flow past cylinder
7	(2-03)	Flow around oscillating airfoil
8	(2-04)	Flow around (airfoils and) blades (subsonic)
9	(2-05)	Flow around airfoils (and blades) A-airfoil (Ma=0.15, Re/m=2x106)
10	(2-06)	Flow around (airfoils and) blades (transonic)
11	(2-07)	3D flow around blades
12	(2-09)	Rotor/stator interaction
13	(3-01)	Boundary layer interacting with wakes under adverse pressure gradient - NLR 7301 high lift configuration
14	(3-02)	Atmospheric boundary layer with rough wall (mesoscale)
15	(3-03)	2D boundary layers with pressure gradients (A)
16	(3-04)	Laminar-turbulent boundary layer transition
17	(3-05)	Shock boundary layer interaction (on airplanes)
18	(3-06)	Natural and mixed convection boundary layers on vertical heated walls (A)
19	(3-07)	Natural and mixed convection boundary layers on vertical heated walls (B)

Application Challenges
External Aerodynamics
Environmental Flows
Turbomachinery Internal Flows
Combustion
Chemical & Process, Thermal Hydraulics & Nuclear Safety
Civil Construction & HVAC

Table 2-3 Underlying Flow Regimes (UFRs) of interest, based on turbulent flow types. Each single UFR is primary to an AC.

		Underlying flow regimes
20	(3-08)	3D boundary layers under various pressure gradients, including severe adverse pressure gradient causing separation
21	(3-09)	Impinging jet
22	(3-10)	The plane wall jet
23	(3-13)	Flow over an isolated hill (without dispersion)
24	(3-14)	Flow over surface-mounted cube/rectangular obstacles
25	(3-16)	Wave-driven flow in a basin
26	(3-18)	2D boundary layers with pressure gradients (B)
27	(3-19)	Bypass transition on a flat plate
28	(4-02)	Confined coaxial swirling jets
29	(4-03)	Pipe flow – rotating
30	(4-04)	Flow in a curved rectangular duct – non rotating
31	(4-05)	Curved passage flow
32	(4-06)	Swirling diffuser flow
33	(4-09)	Confined buoyant plume
34	(4-10)	Natural convection in simple closed cavity
35	(4-11)	Simple room flow
36	(4-12)	Flows in chambers with multiple inlet/outlets
37	(4-13)	Compression of vortex in cavity
38	(4-07)	Developing channel flow with mass injection through wall

Table 2-3 *(continued)*

3

Simple turbulent test cases as the baseline flows[5]

Several turbulent flows which were initially considered to address the types identified in [1] are described in the following sections. These flows (i.e. [64][65][66][67][68][69]), whose DNS datasets are accessible from the ERCOFTAC database, need to be analysed in order to quantify the dominant physical parameters (i.e. $\tilde{L}_X$, $\tilde{T}_L$, and $\tilde{S}$, in particular) which represent their properties. One of the limitations of such datasets is the absence of higher-order correlations information, where the degree of non-Gaussianity parameter $\tilde{G}$ is not able to be determined. Other cases (i.e. those of experiments) have been analysed to circumvent this problem, and will be discussed later in §5.4.

Note that not all 13 main types of flow in [1] have been referred to in this work. Only those which represent the types described within §3.1-§3.8 have been considered.

3.1 Constant pressure boundary layer

The constant pressure flat plate turbulent boundary layer was numerically simulated by Spalart [65] whose idea was to use the fact that both the boundary layer thickness and the turbulence energy level vary slowly along x.

The simulation was run at four stations between $Re_\theta = 225$ to $Re_\theta = 1410$

[5] Much of the work in this chapter as well as in §5.1 - 5.3 of Chapter 5 was presented in [70].

(which are equivalent to $Re_{\delta^+} = 150$ and $Re_{\delta^+} = 650$, respectively), where the three-dimensional transient Navier-Stokes equations were solved using a spectral method with up to around 10^7 grid points. An appropriate procedure was used to estimate the slow growth of the boundary layer in a streamwise direction. The solution provides a good approximation to the local state of the boundary layer which is changing slowly in space.

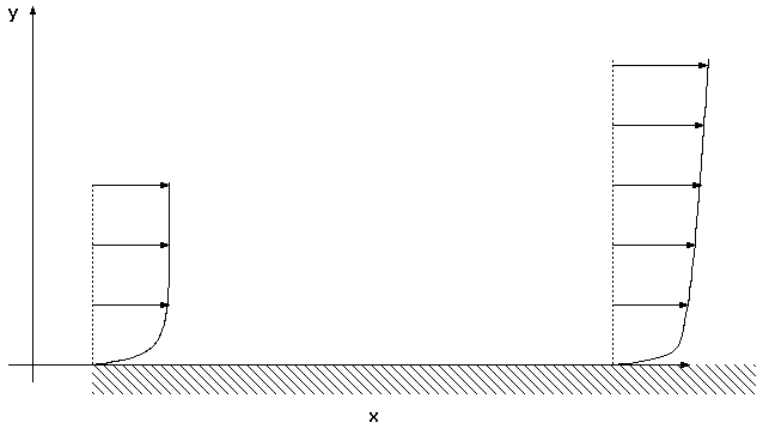

Figure 3-1 Mean velocity profile in a constant pressure boundary layer (reproduced from [65]). In this case, the flow velocity is zero at the wall as required by the no-slip condition, and varies slowly in a streamwise direction x.

3.2 Flat plate transitional boundary layer

A large eddy simulation (LES) of the constant pressure flat-plate transitional two-dimensional boundary layer flow with zero temperature gradient has been conducted by Yang and Voke [64]. The free-stream velocity and the upwind turbulence intensity are given by $u_\infty = 9.6 \text{ms}^{-1}$ and $I = 5.0\%$, respectively. See Figure 3-2 for further details.

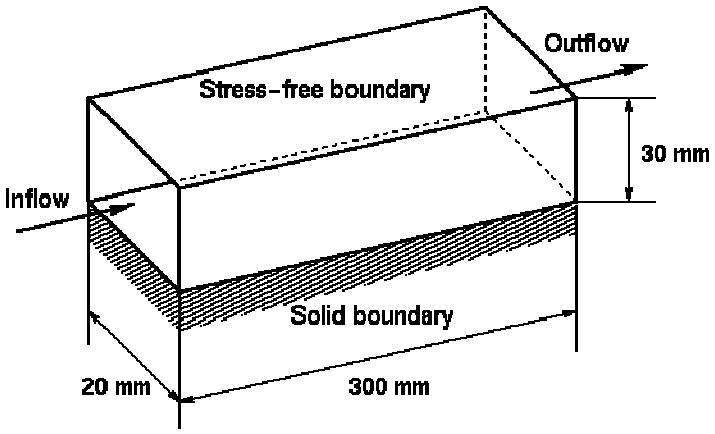

Figure 3-2 Flat plate transitional boundary layer geometry reproduced from [64]. This type of flow is the intermediate state where the flat plate laminar boundary layer breakdown occurs. The transition process from laminar to turbulence is based on instability mechanisms.

3.3 Sink flow

In addition to Spalart's constant pressure boundary layer datasets, his three-dimensional sink-flow boundary layer direct simulations (DNS)[66] data are also considered. Sink-flow boundary layer is the best example of an 'equilibrium' turbulent boundary layer, a boundary layer with a shape that is invariant in the streamwise direction. The flow geometry is shown in

Figure 3-3. It is an incompressible flow with periodic conditions in the directions parallel to the plate, and is a relatively simple flow because it obeys a single similarity law across the entire boundary layer, while general equilibrium boundary layers contain a 'wall' layer and an 'outer' or 'defect' layer. The flow was started with large-amplitude random disturbances, and it was assumed to be statistically steady. The numerical resolution was (170 × 30 × 85) grid points in all dimensions, the acceleration parameter K was set to be in between 1.5×10^{-6} and 3.0×10^{-6}, and as in the previous simulation (i.e. turbulent boundary layer with zero pressure gradient), the three-dimensional, unsteady Navier-Stokes governing equations were solved numerically using a spectral method. The solutions agreed well with the experiments of [27].

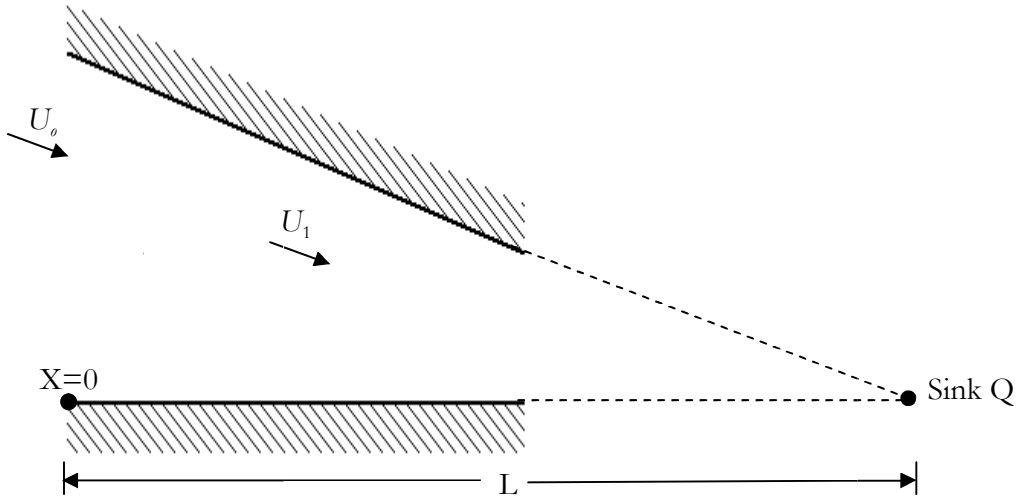

Figure 3-3 Sink flow boundary layer geometry reproduced from [66]; U_o is the free stream velocity at the start of the boundary layer, and U_1 is the local velocity. A potential sink of strength Q exists at x = L. Note that x is the streamwise coordinate.

Spatial averages were taken over the stream and cross-stream directions. Also, the average over time was taken. The spatial-temporal average was necessary so as to reduce statistical jitter.

3.4 Shear layer impingement

The flow over a backward-facing step DNS of Le and Moin [67] provides very useful datasets for studying the shear layer impingement and free shear flow (see Figure 3-4). The simulation used the mean velocity profile obtained from a boundary layer simulation and a convective boundary condition, which were imposed at the inlet at $Re_\theta = 667$ and at the exit, respectively. Also, it used 770 × 194 × 66 mesh points in $x, y,$ and z directions, respectively. Uniform grid spacing was applied in both streamwise and spanwise directions. In wall normal direction, a staggered grid was employed with grid refinement at the wall and near the step.

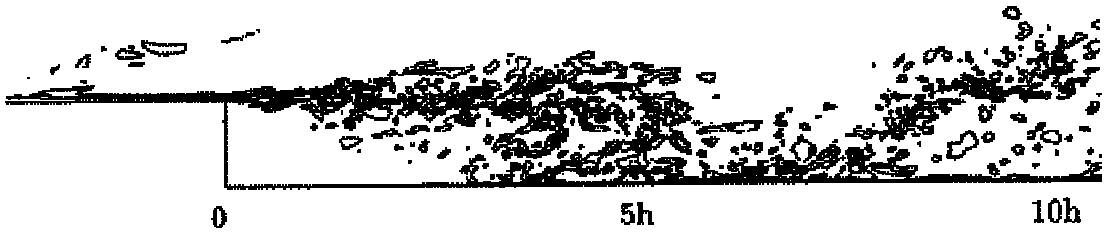

Figure 3-4 Contour plots of the instantaneous spanwise vorticity on a typical vertical plane (reproduced from [67]). The flow that spreads from the step at x=0 is a free shear layer, and is then reattached at around x=6*h* where the shear layer impingement takes place.

The streamwise domain consisted of a $10h$ entry section upstream of the step, and a post-expansion section of length $20h$, where h was the height of the step. The vertical dimensions before and after the expansion were $W_1 = 5h$ and $W_2 = 6h$, respectively, which gave an expansion ratio ER of 1.20, while the spanwise dimension was 4*h*. The step height and the mean inlet free stream velocity u_∞ based Reynolds number was $Re_h = 5100$.

The time-dependent Navier-Stokes equations were discretized using a finite difference method on an irregular grid. The statistical solutions obtained were spatially averaged over z direction, and were also temporally averaged.

It is worth noting here that in this simulation of [67], it was found that there was an interaction between the flow spreading from the step and the lower wall near the mean re-attachment point, i.e. at $x = 6h$ (see [67] for further details).

3.5 Channel flow

The main data used for the quantification of 'localness'-structural parameters in a fully developed turbulent channel flow, are the DNS data by Kim et al. [68]**.** All essential scales of motion were resolved, and no subgrid-scale model was used in this computation. A diagram of the flow geometry and co-ordinate system are shown below in Figure 3-5.

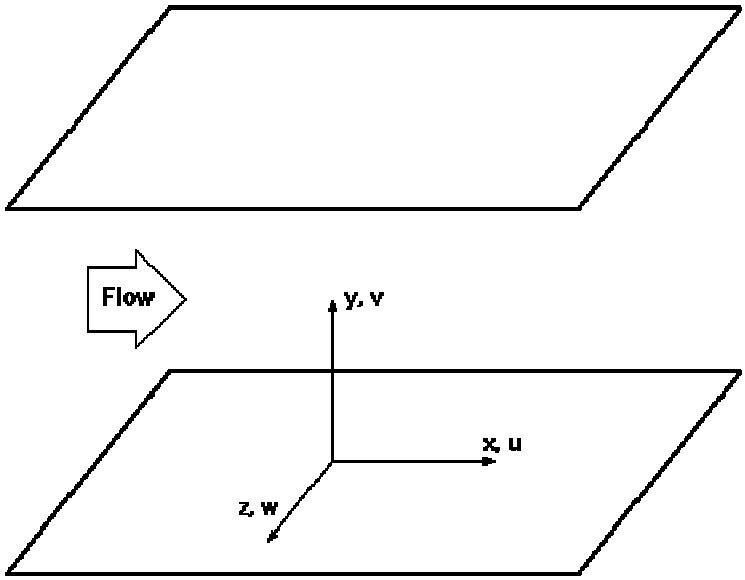

Figure 3-5 Channel flow geometry and co-ordinate system reproduced from [68]. The domain of computation whose boundaries are in the x, y, and z directions is adjusted as necessary in order to make sure that the fluctuations become decorrelated at a separation of one half-period in the homogenous directions.

The channel half-width δ and the centreline velocity u_c based Reynolds number was $Re_\delta = 3300$ which was equivalent to $Re_\tau = 180$ based on the wall friction velocity u_τ.

The computation was carried out with 3,962,880 mesh points (192 × 129 × 160, in streamwise, normal, and spanwise directions, respectively). Staggered grids were used in y direction. The first grid point away from the wall and the maximum spacing (at the centreline of the channel) were at $y^+ \approx 0.05$ and $y^+ = 4.4$, respectively, where y^+ is wall coordinate.

One source of the discrepancy might be related to the measurement of the wall-shear velocity u_τ. When the mean-velocity profiles are renormalised with the corrected (experimental) u_τ, excellent agreement between the experimental results and the computed results is obtained. When the turbulence intensities and the Reynolds shear stress are similarly rescaled, the overall agreement is better, but the computed turbulence intensities, except the streamwise fluctuations, remain lower than the measured values. The use

of hot-film probes to measure turbulence quantities in the proximity of the wall is a possible source of error.

Another source of the discrepancy may be the test section of the oil channel used in the experiments of [71]. The test section is 22cm wide and 7m long and filled with oil to a depth of 85cm, which gives an aspect ratio of 3.9 (depth to width), and the length of the test section is 32 channel widths. This aspect ratio is well below the recommended minimum value of seven to be representative of two-dimensional flow.

The disagreement between the computed and measured values are mostly confined to the immediate vicinity of the wall and do not seem to be serious.

3.6 Sheared homogeneous turbulent flow

In the sheared homogeneous turbulence simulation of [69], while the mean flow was imposed and sheared in the x- and y-directions, respectively, where the shear rate is constant (i.e. S=3.0). The velocity field is initialized to be an isotropic state, satisfying both the continuity equation and the given energy spectrum. The statistics (i.e. the ensemble-averaged turbulent quantities) were computed at the dimensionless time St = 0.0, 1.0, 2.0, ... The calculation was performed in arbitrary units, since the flow did not have appropriate scales for non-dimensionalising the governing time dependent Navier-Stokes and continuity equations. Remeshing was made at a constant interval in order to advance the computation in the coordinate system moving with mean flow. Figure 3-6 represents the flow geometry and co-ordinate system diagram.

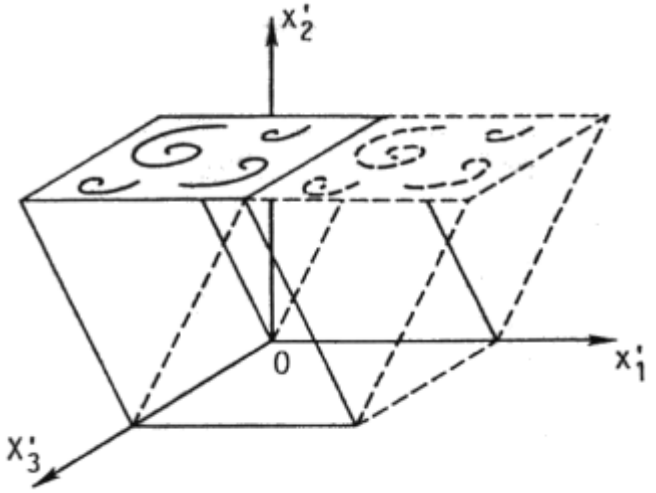

Figure 3-6 A diagram of the sheared homogeneous turbulent flow geometry, and co-ordinates x_i' (i=1, 2, 3) which move with the mean flow (reproduced from [69]). Since the mean strain is irrotational, the mesh has becomed skewed to the right as illustrated by the dashed line. The field is then interpolated onto the mesh skewed to the left (the solid line).

3.7 Free shear flow

A mixing layer, which is that between two uniform parallel streams of different velocities, and jet flow are two instances of free shear flow. In real life, however, a free shear flow can be a combination of these two types of flow. A round jet in co-flow is such an example.

The flow over a rearward facing step [67] is considered as a baseline flow since it was found that there is a free shear flow spreading from the step (see §3.4 for flow and simulation descriptions).

3.8 A note on fully developed turbulence

The cases described in §3.1-§3.6 are fully developed turbulent flows, which in principle, should fulfil the working definition of the fully developed turbulence.

An exchange between random momentums on different timescales and in different directions occurs as a result of the random turbulent motion. In fully

developed turbulent flows, the kinetic energy spectrum $E\left(\hat{k}\right)$ and probability density function $pr(\mathrm{u})$ of fully developed turbulence generally have a single maximum, where $E\left(\hat{k}\right)=E\left(\hat{k}_{mx}\right)$ at the large eddy scales ($\hat{k}_{mx}\sim L_X^{-1}$), and a single maximum in $pr_{(u)}(\mathrm{u})$, respectively. This is true when the mean rate of distortion of turbulence by the mean flow or external forces is not too large (relative to the integral timescale $T_L \sim L_X/u_0$). The skewness S and kurtosis K of $pr(\mathrm{u})$ however, can vary considerably from one flow to another (e.g. [1]). Thus, if there are typically two maxima in $E\left(\hat{k}\right)$, for instance, the turbulence does not satisfy the required criteria. See for example [72] for such cases[6], and [73] for a more detailed discussion of the 'standard' form of $E\left(\hat{k}\right)$.

[6] In [72], a bluff body placed in a turbulent stream is considered. The near wake flow is found not to be fully developed. Rather, a fully developed flow is observed over some diameters downstream.

4
Quantification technique

This chapter sets out to establish a mathematical analysis for the localness-structural parameters, and, generally, their ranges of validity.

Two analysis schemes are adopted to analyse profile data taken from numerical simulation databases. These are a 'segment-by-segment' and 'fixed-point' approaches which are briefly introduced throughout §4.1-§4.3, where the latter is used in the final calculation so as to avoid any loss of information during the repetitive process of averaging the 'localness' parameters, and the former is useful in validating the approach (i.e. the use of finite difference quotients [74]) to obtain the mean velocity gradients $\partial_j \bar{u}_i$. The strategy used to extract and verify the numerical values from the experimental graphs, and to analyse them in order to obtain $\tilde{G}$ is mentioned towards the end of the section.

In the case of master-modes (§4.7), the higher-order correlations needed to be obtained from the simulation first, before $\tilde{G}$ could be determined (rather than quantifying it more directly by analysing the readily available datasets provided by others). The following sections would then introduce the use of its original codes, discuss exactly how to determine the higher-order single-point correlations by means of master-modes, and stress the necessity to modify the codes in order to achieve the objective.

4.1 The Approach

In complex flows, the boundary and matching conditions at the boundaries of the 'conforming domain' outside which the considered turbulence models are invalid need to be considered. Special assumptions based on physics are needed to define these matching conditions, just as in the derivation of the models themselves. Their formulation depends on the nature of the modelling, and on properties of turbulent flow, such as the rate of production and dissipation of energy, and the Reynolds number value. This derivation is driven by considerations of basic mechanisms of turbulence, and characteristic statistical parameters.

A systematic set of four characteristic statistical parameter estimations indicating the type of flows (i.e. that of residence time $\tilde{T}_L$, the normalised strain $\tilde{S}$, the non-Gaussianity $\tilde{G}$, and the degree of non-locality $-\tilde{L}_X$, each of which is dimensionless) will be refined and quantified to establish a firmer framework for their map, by means of direct numerical simulation (DNS) data (the current map is shown in figure 4.1). It is worth noting here that several fundamental simulation analysis data provided by the European Research Community on Flow, Turbulence and Combustion (ERCOFTAC), which is one of the DNS and LES data resources for this research, are providing an essential complement to the mathematical-empirical proposals developed by Hunt and Savill [1; 75].

Each segment of the flows consisting of a sufficient number of grid points will be considered such that the results will cover the interested flow region only, as in the fully developed inner turbulence region near a wall, in the case of constant pressure boundary layer [65], and will allow sufficient averaging.

The results should, in principle, propose an analytic foundation in deciding which types of one-point turbulence models, including those using k-ε and second order closure equations, can or cannot approximately calculate types of turbulent flow.

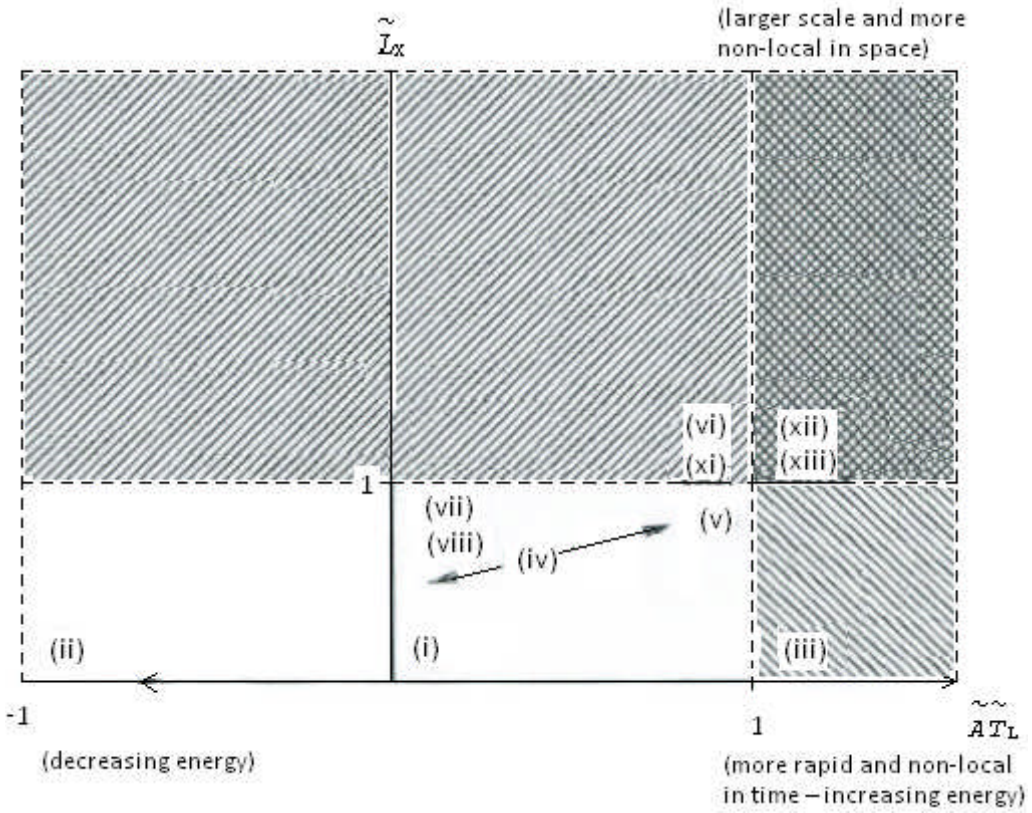

Figure 4-1 Maps for the localness of turbulence process; *Original map by Hunt and Savill* [1]. The Roman numerals on the graph refer to main types of flow. Note that $\tilde{A}$ is the sign of the advective term in the kinetic energy equation (that is either '+' or '-').

4.2 Analysis Equations and Calculation Details

There are two classes of data analysed by these equations. The numerical simulations (i.e. DNS and LES) datasets are considered to quantify the 'localness' parameters and that of strain, in general, while the experimental data are used in quantifying the non-Gaussianity structural parameter. Thus, both the empirical and simulation results are analysed. This is necessary due to the fact that there has been no available single dataset (simulation or experiment) with all the necessary statistics for the quantification of a complete set of the localness-structural parameters. The only exception is the jet in free stream LES data produced by [76] whose dataset is analysed and discussed in §5.4.5 of Chapter 5.

The key parameters are defined as follows [1; 61]:

4.3 'Localness' Parameters

Degree of non-locality

The degree to which turbulence effects are not purely local can be measured by means of the degree of non-locality parameter which is the ratio of the turbulence length scale L_X to that at which the turbulence structure or mean strain rate varies $\Lambda^{(k)}$ or $\Lambda^{(\Sigma)}$, and is therefore mathematically defined as

$$\tilde{L}_X = \max\left\{L_X / \Lambda^{(k)}, L_X / \Lambda^{(\Sigma)}\right\}, \tag{4-1}$$

where

$$0 \le \tilde{L}_X < \infty,$$

$$\Lambda^{(k)} = \frac{k}{|\nabla k|}, \text{ and} \tag{4-2}$$

$$\Lambda^{(\Sigma)} = \frac{S}{|\nabla S|}. \tag{4-3}$$

The larger L_X in comparison with Λ, the more sensitive the turbulence structure to non-local influences (i.e. as a consequence of the non-local relation between the mean velocity gradients and the pressure fluctuations).

Here are considered two distinct cases, each of which is corresponding to different $\Lambda^{(k)}$ and $\Lambda^{(\Sigma)}$, respectively;

Case (a) – The turbulence structure varies more rapidly than the mean strain rate (i.e. $\Lambda^{(k)} < \Lambda^{(\Sigma)}$).

Based on the exact equation (4-1) and (4-2), and the available information in the DNS/LES dataset (e.g. [65] which is considered in this section to illustrate the main method of analysis used for the rest of the cases), the computations for the prediction of $\widetilde{L_x}$ are as follows:

$$\tilde{L}_X = L_X \Big/ \Lambda^{(k)}$$
$$= \frac{k^{3/2}/\varepsilon}{k/\partial_y k}$$
$$= \frac{\sqrt{k}\partial_y k}{\varepsilon} \qquad (4\text{-}4)$$

Note that the values of k and ε in (4-4) could be retrieved from the dataset. To determine $\partial_y k$ the finite difference quotients are used along the shear axis;

$$\partial_y k = \frac{k_{j+1} - k_{j-1}}{2\Delta y} \qquad (4\text{-}5)$$

(Second-order central difference)

At the boundary (e.g. solid boundary),

$$\partial_y k = \frac{-3k_1 + 4k_2 - k_3}{2\Delta y} \qquad (4\text{-}6)$$

(Second-order forward difference)

and

$$\partial_y k = \frac{k_j - k_{j-1}}{\Delta y} \qquad (4\text{-}7)$$

(First-order rearward difference)

The model equation for the normalised length scale $\widetilde{L}_x$ is given by

$$\widetilde{L}_x = \frac{\left[\left(\overline{u_i}\overline{u_i}\right)_{av} T'^2_{av}\right]^{\frac{1}{2}}}{y_{av}}$$
$$= \frac{\sqrt{\left(2k\right)_{av}} T'_{av}}{y_{av}} \qquad (4\text{-}8)$$

where

$$y_{av} = \frac{y_1 + y_2 + ... + y_n}{n}, \qquad (4\text{-}9)$$

$$\left(\overline{u_i u_i}\right)_{\text{av}} = \frac{\left(\overline{u_i u_i}\right)_1 + \left(\overline{u_i u_i}\right)_2 + \ldots + \left(\overline{u_i u_i}\right)_{\text{n}}}{n}, \tag{4-10}$$

$$T'_{\text{av}} = \frac{\left(T'_1 + T'_2 + \ldots + T'_n\right)}{n}, \text{and} \tag{4-11}$$

$$T' = \frac{(y)}{\sqrt{\overline{u_i u_i}}}. \tag{4-12}$$

This model equation works well in the case of constant pressure boundary layer, and this has been successfully validated (see §5.1 and Figure 5-1 of Chapter 5). It is useful when the DNS/LES simulation datasets do not include the rate of dissipation ε which is needed when using the exact equation (4-4).

Note that between the *fixed-point* and *segment-by-segment* approaches, the former is given the priority, not only because the eddies in, for instance, boundary layer (near a wall) are relatively small, but also to avoid the loss of information during the averaging.

However, some of the computations use both approaches, in order to check the reliability of the statistical parameters in defining the region of interest appropriately, of the model equations, and of the finite different quotients in obtaining the gradients (e.g. $\partial_y k$) and accelerations (e.g. $\partial_y^2 \bar{u}$). Note that the finite difference quotients are applied when a simulation dataset does not contain such derivatives, but gives rather 'simple' values as k and $\bar{u}$ at each mesh point. The details are included in §5.1 of Chapter 5.

Case (b) – The mean strain rate varies more rapidly than the turbulence structure (i.e. $\Lambda^{(k)} > \Lambda^{(\Sigma)}$). The normalised length scale $\mathcal{L}_x^{(\Sigma)}$ is calculated by using the following equation [1];

$$\tilde{L}_X = L_X / \Lambda^{(\Sigma)}, \tag{4-13}$$

$$0 \le \tilde{L}_X < \infty,$$

where

$$\Lambda^{(\Sigma)} = \left| S/\nabla S \right|.$$

In shear flow,

$S = \partial_y \bar{u}$, and

$$\nabla S = \partial_y^2 \bar{u}.$$

Thus equation (4-13) becomes

$$\tilde{L}_X = \frac{L_X}{\left| \partial_y \bar{u} / \partial_y^2 \bar{u} \right|}. \tag{4-14}$$

In manipulating DNS or LES data of shear flows, the averages of the above parameter values (4-4) and (4-13) have to be calculated for a particular number of grid points across turbulent flows:

$$\tilde{L}_{\mathrm{X_{av}}} = \frac{\tilde{L}_{\mathrm{X_1}} + \tilde{L}_{\mathrm{X_2}} + \ldots + \tilde{L}_{\mathrm{X_n}}}{\mathrm{n}},$$

where n is the total number of points covering the flow or flow region of interest.

Note that the values of parameter $\tilde{L}_x$, defined by (4-4), (4-8), and (4-13) vary with respect to the number of grid points, but nevertheless, only fall in the qualitative estimate for the flow region of interest (i.e. with sufficient number of grid points). Equations (4-4) and (4-8) apply when the turbulent kinetic energy changes more rapidly than the mean rate of strain in space. If the mean strain rate variation is more significant, then equation (4-13) applies.

Residence time parameter

When the eddies become distorted, the timescale over which they are subject to convection into a domain (e.g. a pipe or boundary layer) is $T_D = T_{Df} - T_{Di}$, where T_{Di} and T_{Df} are the initial and final times, respectively. The residence time parameter $\tilde{T}_L$ is mathematically defined as the ratio of Lagrangian integral timescale (or turbulence timescale) T_L to the flow distortion timescale:

$$\tilde{T}_L = \frac{T_L}{T_D},$$

which provides a measure of the dependence of the advected turbulence on the upstream boundary conditions, or initial conditions.

In the case where the turbulence is changing rapidly, $\tilde{T}_L > 1$, which means that the degree of non-equilibrium is high, and the eddies are rapidly distorted, the turbulent kinetic energy k helps to maintain the eddies, and thus, its net production (i.e. $(\mathcal{P}-\varepsilon)$, where $\mathcal{P}$ is the production of turbulent energy and ε is the dissipation rate) would increase the eddies' lifetime. The net production, however, is less significant when $\tilde{T}_L < 1$ (i.e. equilibrium turbulent flow). Both cases are equivalent to those in which $\mathcal{P} < \varepsilon$ and $\mathcal{P} \approx \varepsilon$, respectively, and the turbulence changes rapidly and slowly with respect to time in the former and the latter, respectively. Several authors, e.g. [2], have demonstrated the very close similarity between turbulence change and the degree of non-equilibrium of its structure, and hence, $\tilde{T}_L$ is also known as the degree of non-equilibrium of turbulence structure such that;

$$\tilde{T}_L = T_L / T_D \cong \left| P/\varepsilon - 1 \right|, \qquad (4\text{-}15)$$
$$0 \le \tilde{T}_L \le \infty.$$

Exploiting DNS data of shear flows, the average (i.e. $\tilde{T}_{L_{\text{av}}}$) calculated for a particular number of grid points n across turbulent flows is defined by

$$\tilde{T}_{L_{\text{av}}} = \frac{\left(\tilde{T}_{L_1} + \tilde{T}_{L_2} + \ldots + \tilde{T}_{L_n}\right)}{n}.$$

When non-continual energy input (e.g. body force) is taken into account, the sign of the advective term $\tilde{\text{A}}$ is included in the definition (4-15):

$$\tilde{\text{A}}\tilde{T}_L = \tilde{\text{A}}T_L/T_D,$$
$$\text{where } \tilde{\text{A}} = 1, -1.$$

Note that, in this work, the sign $\tilde{\text{A}}$ is considered as invalid if the energy input is constant (e.g. in homogeneous turbulence), as will be discussed in §7.1.

There is a special case when $\mathcal{P} < \varepsilon$, (i.e. in homogeneous decaying turbulence where the net production is negative), yet the unresolved motion is not just dissipating energy locally but feeding it back to the large scale motion, as a consequence of the fact that vortex forms are not stretched monotonically but sometimes contract [33]. In such a case $\tilde{T}_L < 0$.

If there is no variation in the turbulence structure and/or mean strain rate over a turbulent scale (e.g. L_X), then there would not be any significant difference between the effect of turbulence at two points (i.e. at $\left(x + dx\big|_{dx\to 0}\right)$ and $\left(x + x_2\right)$) and at a single point $\left(x + dx\big|_{dx\to 0}\right)$ on the turbulence at a given point x. The turbulence is local (i.e. there are no non-local influences), and therefore, changes slowly, and the single-point correlation is sufficient and appropriate:

$$\begin{aligned}\overline{u_i\left(x + dx\big|_{dx\to 0}\right)u_j\left(x + x_2\right)} &= \overline{u_i\left(x + dx\big|_{dx\to 0}\right)u_j\left(x + dx\big|_{dx\to 0}\right)} \\ &= \overline{u_i(x)u_j(x)} \\ &= \overline{u_i u_j} \quad \left(\text{non-local influences can be neglected}\right),\end{aligned}$$

Where $dx < \left|x_2 - x\right| \le L_X$. Otherwise, such perturbations at two points and that at a single point affect differently the turbulence at the given point, and

thus, the single-point correlation would no longer be sufficient (i.e. the two-point correlation is significant):

$$\begin{aligned}\overline{u_i\left(x+dx\big|_{dx\to 0}\right)u_j\left(x+x_2\right)} &\neq \overline{u_i\left(x+dx\big|_{dx\to 0}\right)u_j\left(x+dx\big|_{dx\to 0}\right)} \\ &\neq \overline{u_i(x)u_j(x)} \\ &\neq \overline{u_i u_j}\ \left(\text{non-local influences present}\right),\end{aligned}$$

where $dx<\left|x_2-x\right|\le L_X$. Therefore, in the latter case, a one-point closure model cannot correctly represent two turbulent quantities which have a non-local relation, even for simple homogeneous turbulent flows in, for instance, the presence of rapidly changing mean velocity gradients. The non-local relation between the velocity and pressure, for instance, can be demonstrated using linear theory, where the linear or 'rapid' part of the pressure-strain redistribution term dominates:

$$-\frac{1}{\rho}\partial_k^2 p' = 2\partial_j \bar{u}_i \partial_i u'_j .$$

In the improvement of single-point closure estimates, the linear theory has proved to be useful especially for swirling flows, though the expression above is only approximately modelled (in Reynolds stress transport model, RSM, equations). The length scale anisotropy effects can be incorporated directly in RSM [77]. The discussion on this fundamental difficulty can be found in [59] and [78].

4.4 Structural parameters

Strain parameter

An indication of the strength of flow distortions, or (more precisely) of the relative domination between mean strain rate and mean rate of rotation in a turbulent flow region is given by a non-dimensional strain parameter $\tilde{S}$ that is the second order invariant of the large scale straining derived from the gradients of the mean velocity, and normalised on the squares of the

symmetric strain rate and the vorticity. Despite its name, this parameter which ranges between -1 and 1 is not exactly the mean strain rate. It is mathematically defined by

$$\tilde{S} = \frac{\Sigma^2 - \frac{1}{2}\Omega^2}{\Sigma^2 + \frac{1}{2}\Omega^2}, -1 < \tilde{S} < 1$$

$$= \frac{\Sigma_{ij}\Sigma_{ij} - \frac{1}{2}\Omega_l\Omega_l}{\Sigma_{ij}\Sigma_{ij} + \frac{1}{2}\Omega_l\Omega_l} \qquad (4\text{-}16)$$

where $\Sigma^2 = \Sigma_{ij}\Sigma_{ij}$, $\Omega^2 = \Omega_l\Omega_l$. (4-17)

Taking an average over a number of grid points,

$$\tilde{S}_{av} = \frac{\tilde{S}_1 + \tilde{S}_2 + \ldots + \tilde{S}_n}{n},$$

Note that Σ_{ij} in (4-16) and (4-17) is the symmetric strain (stretching) tensor, and Ω_l is the vorticity, each of which is defined by

$\Sigma_{ij} = \frac{1}{2}\left(\partial_j \bar{u}_i + \partial_i \bar{u}_j\right)$, and

$\Omega_l = \varepsilon_{lmn}\partial_n \bar{u}_m$, respectively.

Some simulations (e.g. strained channel [79] and rearward-facing step [67] DNS) either assumed zero, or produced the insignificantly small mean velocity gradients in the streamwise direction, and thence equation (4-16) can be reduced to:

$$\tilde{S} = \frac{\left(\partial_y \bar{v}\right)^2}{\left(\partial_y \bar{v}\right)^2 + \left(\partial_y \bar{u}\right)^2 + \left(\partial_y \bar{w}\right)^2} \qquad (4\text{-}18)$$

Rewriting (4-18) in finite-difference quotients along the shear axis, one has

$$\tilde{S}=\frac{\left[\left(\bar{v}_{j+1}-\bar{v}_{j-1}\right)/2\Delta y\right]^2}{\left[\left(\bar{v}_{j+1}-\bar{v}_{j-1}\right)/2\Delta y\right]^2+\left[\left(\bar{u}_{j+1}-\bar{u}_{j-1}\right)/2\Delta y\right]^2} \tag{4-19}$$

(second-order central difference)

At the boundary (e.g. solid boundary)

$$\tilde{S}=\frac{\left[\left(-3\bar{v}_1+4\bar{v}_2-\bar{v}_3\right)/2\Delta y\right]^2}{\left[\left(-3\bar{v}_1+4\bar{v}_2-\bar{v}_3\right)/2\Delta y\right]^2+\left[\left(-3\bar{u}_1+4\bar{u}_2-\bar{u}_3\right)/2\Delta y\right]^2} \tag{4-20}$$

(second-order forward difference)

and

$$\tilde{S}=\frac{\left[\left(\bar{v}_{j}-\bar{v}_{j-1}\right)/\Delta y\right]^2}{\left[\left(\bar{v}_{j}-\bar{v}_{j-1}\right)/\Delta y\right]^2+\left[\left(\bar{u}_{j}-\bar{u}_{j-1}\right)/\Delta y\right]^2} \tag{4-21}$$

(first-order backward difference)

It is worth noting that in purely rotating (or swirling) flow and in purely straining flow, $\tilde{S}\sim -1$ and $\tilde{S}=1$, respectively, where the eddy structure and the energy of the turbulence are quite sensitive to the initial conditions and the history of the flow [80].

Degree of Non-Gaussianity

The third moment, or asymmetry (skewness) S_i of the u_i distribution is given by $\overline{u_i u_i u_i}$ scaled on $\overline{u_i u_i}^{3/2}$. In the case of single-point correlation function, the definition is;

$$S_i = \frac{\left\langle u_i(\mathbf{x}) u_i(\mathbf{x}) u_i(\mathbf{x}) \right\rangle}{\left\langle u_i(\mathbf{x}) u_i(\mathbf{x}) \right\rangle^{3/2}} = \frac{\left\langle u_i(\mathbf{x})^3 \right\rangle}{\left\langle u_i(\mathbf{x})^2 \right\rangle^{3/2}} = \frac{\left\langle u_i{}^3 \right\rangle}{\left\langle u_i{}^2 \right\rangle^{3/2}},$$

where

$u_i = \text{fluctuating velocity}\,(i = 1,2,3)$
$u_1 = u$
$u_2 = v$
$u_3 = w.$

This factor S_i indicates whether the function is symmetric about the origin or not, where $S_i = 0$ or $S_i \neq 0$, respectively. Note that the Gaussian value for the skewness is 0. If S_i is positive, large positive values of u_i are more frequent than large negative values, and vice versa.

The fourth moment of a quantity, such as $\overline{u_i^4}$ normalised by $\overline{u_i^2}^2$, describes the kurtosis K_i, or flatness of the probability distribution of u_i, i.e. $pr(u_i)$;

$$K_i = \frac{\left\langle u_i(\mathbf{x}) u_i(\mathbf{x}) u_i(\mathbf{x}) u_i(\mathbf{x}) \right\rangle}{\left\langle u_i(\mathbf{x}) u_i(\mathbf{x}) \right\rangle^2} = \frac{\left\langle u_i(\mathbf{x})^4 \right\rangle}{\left\langle u_i(\mathbf{x})^2 \right\rangle^2} = \frac{\left\langle u_i{}^4 \right\rangle}{\left\langle u_i{}^2 \right\rangle^2}.$$

It functions as a measure of the frequency of having u_i far from the horizontal axis. When this event is relatively frequent, $|K_i| > 3.$ For a Gaussian distribution, $|K_i| = 0.$ The non-Gaussianity in term of flatness factor is given by $\left(K(u_i) - 3\right).$

Defined as small if the probability distribution of the fluctuating velocity is close to that of the Gaussian variable, the parameter $\tilde{G}$ measures the degree of non-Gaussianity of turbulence. In other words, it is the deviation of the velocity fluctuations distribution from that of Gaussian. It is constructed via skewness S_i and kurtosis K_i factors-based criteria, and is defined by

$$\tilde{G} = \max\left\{ \frac{\overline{u_i^4}}{\left(\overline{u_i^2}\right)^2} - 3, \frac{\overline{u_i^3}}{\left(\overline{u_i^2}\right)^{3/2}} \right\}, \tag{4-22}$$

The first term refers to the deviation from the flatness in Gaussian distribution, while the second indicates the 'difference' from the skewness factor. Such deviation is independent of the signs of the factors. If S_1 and S_2 take, for instance, the values of 1 and -1, respectively, $\tilde{G} = 1$ in both cases. Similarly, in each case where $K_2 = 3$ or $K_2 = -3,$ for example, $\tilde{G} = 0$. In fact, by definition, $0 < \tilde{G} < \infty$. This implies that the first and last terms in the equation (4-22),

$$\overline{u_i 4} \Big/ \left(\overline{u_i 2}\right)^2 \text{ and } \overline{u_i 3} \Big/ \left(\overline{u_i 2}\right)^{3/2}$$

are necessarily positives. If the distribution is exactly normal, then $\tilde{G} = 0.$

The definition (4-22) is not to be considered as the summation over the repeating indices (as that following the Einstein convention). It is clear that in any spatial direction (i.e. streamwise, cross stream, and spanwise directions), the flatness, for example, takes the value of 3 for the Gaussian distribution of the velocity fluctuations. This study considers the quantification of $\tilde{G}$ on average in three-dimensions.

If there is no variation in the Gaussian structure of the large scale turbulence, then the effects of its structure at two points (i.e. at $\left(x + dx\big|_{dx\to 0}\right)$ and $\left(x + x_2\right)$) would not significantly differ from those at a single point $\left(x + dx\big|_{dx\to 0}\right)$ on the structure at a given point x. The turbulence is locally Gaussian, and therefore, the single-point correlation is sufficient and appropriate;

$$\begin{aligned} \overline{u_i\left(x + dx\big|_{dx\to 0}\right) u_j\left(x + x_2\right)} &= \overline{u_i\left(x + dx\big|_{dx\to 0}\right) u_j\left(x + dx\big|_{dx\to 0}\right)} \\ &= \overline{u_i u_j}, \end{aligned}$$

where

$dx < |x_2 - x| < L_X$.

Otherwise, the effects of such a structure at two points would differ from those at a single point, and thus, the single-point correlation would no longer be accurate (i.e. the two-point correlation is irreducible);

$$\overline{u_i\left(x+dx|_{dx\to 0}\right)u_j\left(x+x_2\right)} \neq \overline{u_i\left(x+dx|_{dx\to 0}\right)u_j\left(x+dx|_{dx\to 0}\right)}$$

$$\overline{u_i\left(x+dx|_{dx\to 0}\right)u_j\left(x+x_2\right)} \neq \overline{u_i u_j},$$

where

$dx < |x_2 - x| < L_X$.

4.5 Remarks

Need for alternatives

Note that current archival simulation databases do not generally include sufficient information in order to execute equation (4-1). The direct numerical simulation (DNS) dataset for turbulent boundary layer in [65], for instance, contains only very basic statistics. To illustrate this situation further, consider first equation (4-2). The turbulent kinetic energy,

$$k = \frac{1}{2}\overline{u_i u_i},$$

can be calculated from "Mean and mean-square fluctuations" (see next page). However, one cannot simply determine the denominator,

$$\left|\nabla k\right| = \left|\left(\partial_x + \partial_y + \partial_z\right)k\right|,$$

based on the dataset, because;

i) The advection term's values,

$$\bar{u}_k \partial_k k = \left(\bar{u}\partial_x + \bar{v}\partial_y + \bar{w}\partial_z \right) k,$$

in the kinetic energy equation are given in single forms rather than $\bar{u}\partial_x k$, $\bar{v}\partial_y k$, and $\bar{w}\partial_z k$.

ii) Mean velocity $\bar{u}$ is included (from momentum equation) but not $\bar{v}$ and $\bar{w}$.

Note that practically $|\nabla k|$ could be determined, in the absence of these problems, by

$$|\nabla k| = \left| \frac{\bar{u}_k \partial_k k}{\bar{u}_k} \right|$$

For a shear flow, the denominator of equation (4-3) becomes

$$\begin{aligned} |\nabla S| &= \left| \left(\partial_x + \partial_y + \partial_z \right) S \right| \\ &= \left| \partial_y{}^2 \bar{u} \right| \end{aligned}$$

Again, $|\nabla S|$ cannot simply be calculated based on the dataset especially because it is not a part of the terms in the Reynolds averaged Navier-Stokes equations. This necessitates the use of other options such as finite different quotients, i.e (4-5)-(4-7) and (4-19)-(4-21), and model equations (in particular those to determine direct influence between two distant turbulent regions), i.e. (4-8)-(4-12).

As an example, consider the DNS dataset [65] for turbulent boundary layer with constant pressure at $Re_{\delta^+} = 650$ [65]. Applying equation (4-8) gives a value of around 0.5 for $\tilde{L}_x$ for the 'near wall' region. This agrees with the estimate presented in Table 2-2. On the other hand, the decelerated wall bounded turbulent flow DNS data [79] is also analysed; the result will be compared with the qualitative estimate. Details and conditions of the calculations are shown in §5.1 of Chapter 5. This model equation is essentially dimensional analysis and heuristically constructed. However, good results

have been obtained. Although it may not be clear where proper physics enters the process, this approach is still useful, provided that the models of turbulence in the later guidelines can give a design and/or performance prediction of critical engineering devices to acceptable engineering accuracy, over the full range of flows of interest.

'Good' turbulence models

The idea of having appropriate turbulence predictions based on the localness-structural statistical parameters has been stressed in [1] (see also §2.8.4), where criteria for the general validity of the models have reasonably been proposed by considering the 'localness' of the turbulence dynamics in the particular 'types' of flow chosen as the test cases for the construction of the model equation. This is why the turbulent flow classification founded on the basic mechanism of the turbulence structure is very useful, and is indeed of critical importance in choosing the correct closure models. Thus, the mutual interplay between such flow 'types' (i.e. typical shear flows, boundary layers, jets, wakes, and slowly decaying homogeneous turbulence) and, for example, the k equation in the case of the local model, suggests that the criteria for the wider validity of the flow are approximately similar to the $k-$ equation.

Another criterion for $k-\varepsilon$ to be valid is that the type of 'straining' is not prevalent, i.e. $\tilde{S} < 1/10$, because the ε equation is not well adapted for turbulent flows in which the mean strain is mainly rotational or irrotational [1].

4.6 Defining the regions of interest

In relatively difficult cases, each region of interest (e.g. reattachment region in the flow over rearward facing step) is identified by the normalised length scale $\tilde{L}_x$. See §5.1 of Chapter 5.

4.7 Master-modes Manipulation

A master-mode-set is a series in a form of basic functions (i.e. those which are referred to as modes) that represent the turbulent flow fields. It gives the time history of the entire flow provided that the flow is developed. The master-mode-set for turbulent channel flow was demonstrated numerically by [103]. It has been found that the minimal set is a good approximation for mean velocity in the entire flow field, although a larger than minimal set is necessary to predict mean velocity derivatives and two-point correlations correctly. Detailed information can be found in [103; 104].

The original codes used in the master-modes were meant for computing second-order two-point correlations. Such codes have been modified to produce higher-order correlations in order to quantify the degree of non-Gaussianity $\tilde{G}$ whose formulation is given in §4.4. This computation has been made on the UKTC DNS Web Server, and is discussed in detail in §5.4.6.

4.8 Other Possible Methods of Estimation

The degree of non-locality $\tilde{L}_X$, could also possibly be obtained by other measurement methods. The examples of such an approach would be that of a hot wire anemometer as well as the DNS that produce two-point correlations of the flow particle velocities, i.e. u_i' $(i=1,2,3)$. The length scales are determined by integrating such fluctuating velocities, as functions of spatial and time dimensions (i.e. $\vec{x}_1, \vec{x}_2, t$), with respect to time. Since u_i' are considerably homogeneous for small scales, it is necessary to integrate u_i' in a sufficiently long time. This will increase the possibility of obtaining the larger scale at which u_i' changes its magnitude, ideally with parallel opposite direction to that evaluated at the lower limit of time. The length scales, combined with those over which the turbulence structure or mean strain rate varies Λ, will provide a more 'direct', and perhaps, better estimation for $\tilde{L}_X$. The result could be used to refine the model equations (4-8)-(4-12).

4.9 'Quantitative' Application

In order to finalise the guideline map for choosing appropriate prediction methods as a framework for best practice guidelines, the application challenges (ACs) arise from the zonal modelling approach with respect to the underlying flow regimes (UFRs) that need to be considered [53]. Both ACs with their UFRs of interest are presented in Table 2-3 of Chapter 2. Every flow regime will be made 'realisable' in the map. Given a complex flow, we should be able to decide whether or not its flow regimes could be fully or partially grouped together in terms of a certain turbulence model. This 'realisation' will be done on the grounds of quantitative characteristic statistical parameters, in particular those of the spatial and temporal localness, and the straining.

5
Quantified 'localness'-structural statistical parameters

An array of sets of DNS and LES data provided in [64-69], each of which is based on a low Reynolds number, are considered in this analysis, involving the turbulent flows that are spatially local, local in time, and non-local both in space and time. Brief descriptions about these flow types of practical importance, their properties, classes based on main flow types [1], and number of datasets considered, have already been given in Chapter 3.

The starting and ending grid points, as well as the number of points lying in between were chosen such that they covered the fully developed turbulence zones of interest only, including/excluding the viscous sub-layer zone depending on the cases. Considering various total numbers of grid points, across streamlines, the computations for the statistical parameters were done.

The resulting explicit values for the 'localness' (i.e. $\tilde{L}_X$ and $\tilde{T}_L$) as well as structural statistical parameters (i.e. $\tilde{S}$ and $\tilde{G}$) presented in §5.1, 5.2, 5.4, and 5.5 need to be tested against the previous mathematical-empirical study (also shown in Figure 4-1 in Chapter 4) to ascertain numerical accuracy (i.e. whether or not they fall nicely into the previous estimate).

5.1 Normalised Length Scale

It is worth, at this point, finding out if the model equation (4-8) works well by considering the constant pressure boundary layer case. Equation (4-8) reflects the proportionality between $\widetilde{L}_x$ and the square root of mean turbulent kinetic energy $\sqrt{k}$, as does the exact equation (4-4). Figure 5-1 shows the variation of the quantified $\tilde{L}_X$ across the domain, and that it tends towards 0.50. Note that the qualitative estimate for $\tilde{L}_X$ is ~½ (see Table 2-2). This suggests that both the equation (4-8) and the finite difference quotients (4-5)-(4-7) used for computing $\tilde{L}_X$ work well if a sufficient number of points are available, and the boundary limit point is well defined[7].

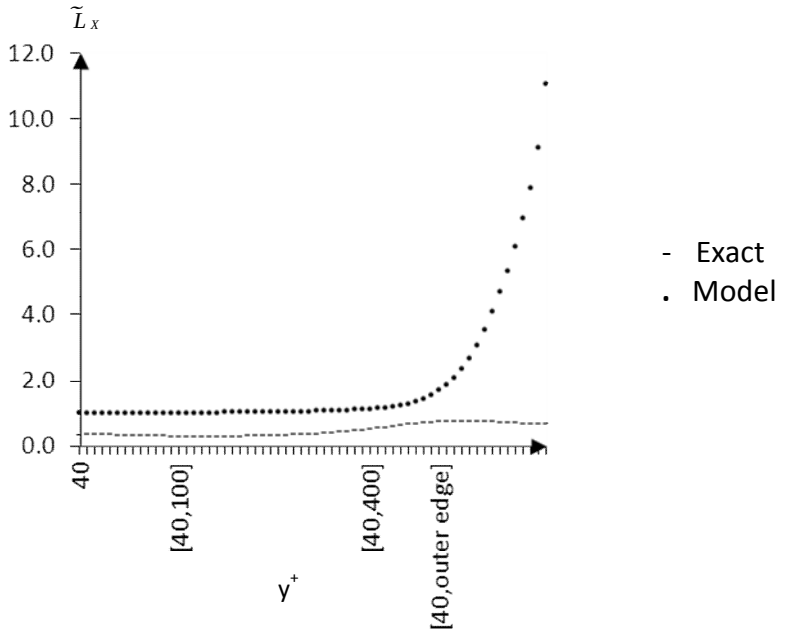

Figure 5-1 Variations of the normalised length scale in constant pressure boundary layer at $Re_{\delta^+} = 650$, as predicted by (exact) equations (4-4)-(4-7), and by (model) (4-8). The parameter $\widetilde{L}_x$ in the region of interest takes the value of about 0.5. The region (near a wall) is that which starts from about $y^+ = 40$ (below which the effects of viscous sublayer regions begin to be seen) and ends at the edge of the inner region (around $y^+ = 400$).

Secondly, it will be demonstrated that the normalised length scale can be used to define the regions of interest, in particular in relatively difficult cases.

[7] Note that the concept of finite difference quotients used here is also applied in quantifying the straining parameter $\tilde{S}$ in §5.4.

Consider Figure 5-2 for the variation of $\widetilde{L}_x$ in three different cases. In case (a) where $Re_{\delta^+} = 650$, the region of interest is $40 \leq y^+ \leq 400$; it is assumed that the edge of the viscous layer and the inner edge of the boundary layer lie at $y^+ \approx 40$ and $y^+ \approx 400$, respectively. However, this choice is not possible in cases (b) and (c), where the Reynolds numbers Re_{δ^+} are relatively low (i.e. 325 and 150, respectively), especially since the outer edge of the boundary layer is at $y^+ < 400$. This could be understood since the low Reynolds number reflects the relatively thin boundary layer.

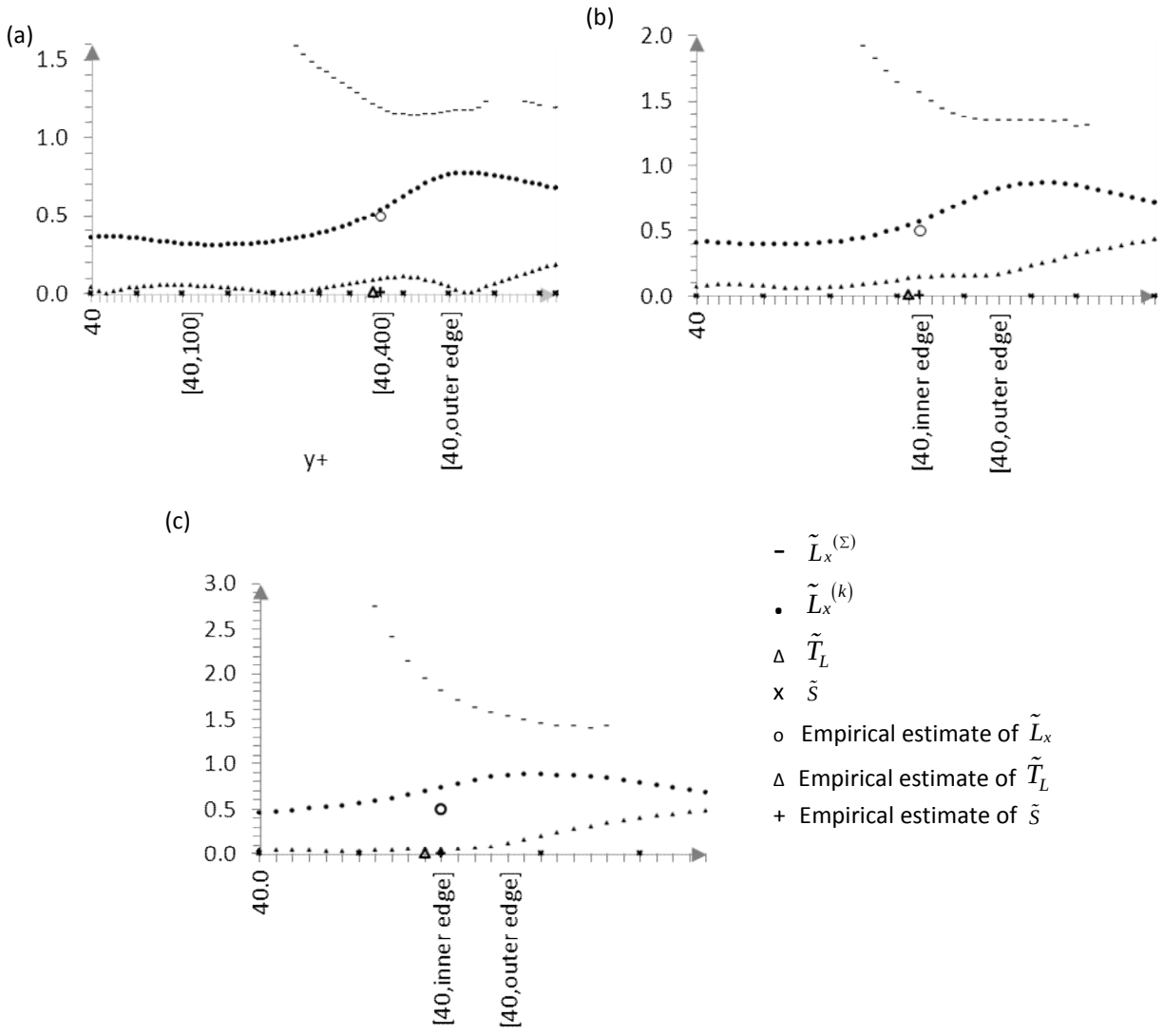

Figure 5-2 Variations of the normalised statistical parameters in constant pressure boundary layer (near a wall).

It can be shown that, as in case (a), the distance between the edge of the viscous layer and the inner edge of boundary layer is about 60% of that between the viscous layer edge and the outer edge of the boundary layer, such that

$$y^+_{\text{inner edge}} \approx 40 + 0.6\left(y^+_{\text{outer edge}} - 40 \right).$$

When one applies this equation to both cases (b) and (c), the inner edges then lie at

$$\left(\text{b}\right) y^+_{\text{inner edge}} = 181 \quad \text{at} \quad Re_{\delta^+} = 325$$

$$\left(\text{c}\right) y^+_{\text{inner edge}} = 99 \quad \text{at} \quad Re_{\delta^+} = 150$$

This information has been used for defining the regions of interest in order to quantify the normalised statistical parameter in both cases (b) and (c). Table 5-1 shows the quantification results. Even if the inner edge of the boundary layer lies at $y^+<400$, the results still confirm the qualitative estimate, and hence proves that the quantification approach used is reliable for the low Reynolds number flows.

Note that *fixed-point* approach is used, and that the empirical estimates shown on the graphs are subject to uncertainty bounds. (a) $Re_{\delta^+} = 650.$ (b) $Re_{\delta^+} = 325.$ (c) $Re_{\delta^+} = 150.$ The fact that the residence time parameter $\tilde{T}_L$ in (a) is slightly underestimated, though $\tilde{L}_X$ value is acceptable, might suggest that the qualitative reference is not really applicable to such low Re_{δ^+}.

	Re_{δ^+}	Interested region	Quantitative $\tilde{L}_x^{(k)}$	Quantitative $\tilde{L}_x^{(\Sigma)}$	Qualitative $\tilde{L}_x$	$\tilde{T}_L$ Quantitative	$\tilde{T}_L$ Qualitative	Flow of reference
(a)	650		0.53	1.20		0.10		
(b)	325	$40 \le y^+ \le$ inner edge	0.57	1.57	$\sim 1/2$	0.15	$<< 1$	Turbulent boundary layer (near a wall)
(c)	150		0.74	1.82		0.05		

Table 5-1 The quantitative and qualitative estimates of the normalised statistical parameters in constant pressure boundary layer. All values well agree with the empirical estimates. In all cases, the only non-zero (mean) velocity gradient is $\partial_y \bar{u}$ as suggested by the corresponding datasets, and thus $\tilde{S}$ vanishes (see(4-18)).

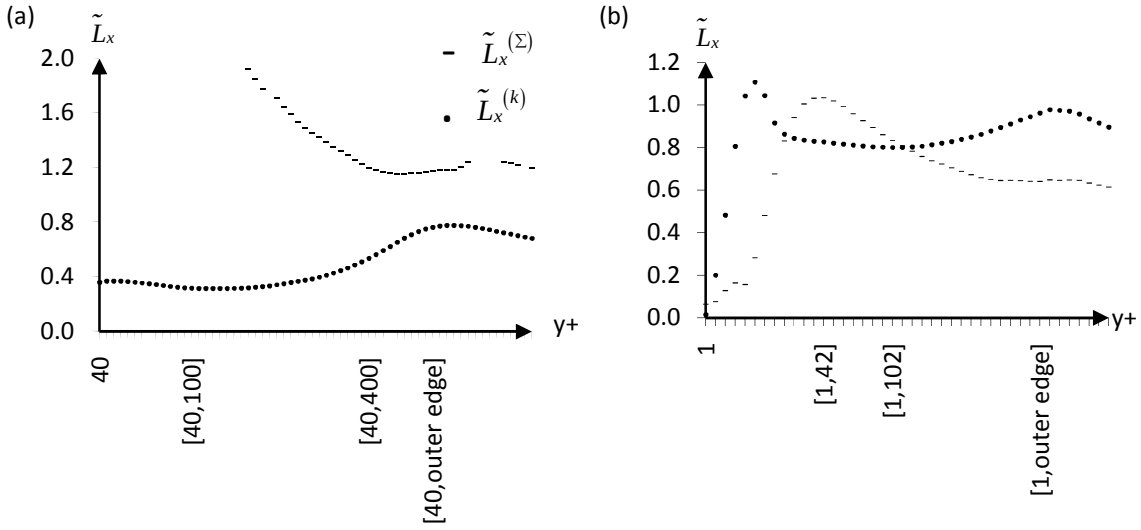

Figure 5-3 Variations of the normalised length scales ($\tilde{L}_x^{(\Sigma)}$ and $\tilde{L}_x^{(k)}$)

(a) Constant pressure boundary layer (DNS by Spalart, 1988) at $Re_{\delta^+} = 650$.
(b) Sink-flow (DNS by Spalart, 1986) at $Re_\theta = 690$, and with acceleration parameter $K=1.5\text{x}10^{6}$.

In the case of flat plate transitional boundary layer, the data [64] have been analysed *segment-by-segment* across the streamline. The main results of $\tilde{T}_L$ are those ranging between 0.57 and 0.94 for the last four segments, and show

good agreement with the mathematical-empirical estimate of ~ 1. These segments consist of 16 grid points as shown in Figure 5-4, and are approximately those with 99% of the free stream velocity (i.e. around 'the edge of the boundary layer'). This means that the values for $\tilde{L}_X$ should also be those for the last four segments, which range between 0.98 and 1.00, compared to the empirical estimate of $\gtrsim 1$.

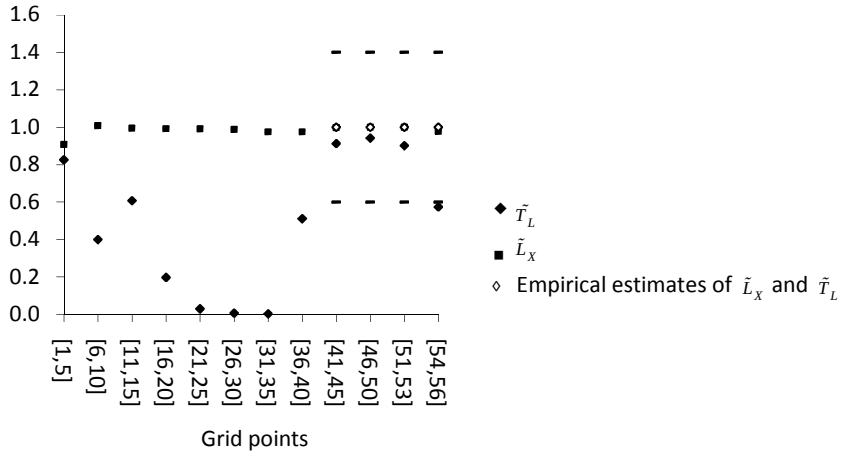

Figure 5-4 Variations of $\tilde{T}_L$ and $\tilde{L}_X$ in flat plate transitional boundary layer, and again the dashes (-) denote the illustrative tolerance values.

A similar analysis approach (i.e. fixed-point method using definitions (4-1) and (4-4)-(4-7)) was implemented for the rest of the flows (see Appendix B.1) and the results are recorded in Table 5-2.

	Flow types	Region of interest	Quantitative $\tilde{L}_x^{(k)}$	Quantitative $\tilde{L}_x^{(\Sigma)}$	Qualitative	Flows of reference [1]
(a)	Constant pressure boundary layer	$40 \le y^+ \le 400$	<u>0.53</u>	1.20	$\sim 1/2$	Turbulent boundary layer (near a wall)
(b)	Sink flow	$1 \le y^+ \le y^+_{\delta 0.99}$	0.96	<u>0.64</u>	$<< 1$	Strained turbulence
(c)	Flat plate transitional boundary layer	$0.1 \le y(mm) \le y_{\delta 0.99}$	<u>1.79</u>	3.68	$\gtrsim 1$	Large scale free stream turbulence interacting with a boundary layer
(d)	Shear layer impingement	$0 \le y/h \le 1$	<u>1.84</u>	4.47	~ 1	Jet impaction
(e)	Channel flow	$0 \le y^+ \le y^+_{d/2}$	<u>1.50</u>	1.82	~ 1	Turbulent boundary layer (near outer boundary)
(f)	Sheared homogeneous turbulent flow	$0 \le y \le 2.9$	<u>0.002</u> ≈ 0	-	$<< 1$	Strained turbulence
(g)	Free shear flow	$0 \le y/h \le 3.45$	<u>2.38</u>	16.06	~ 1	Free shear flows and separated flows

Table 5-2 The quantitative and qualitative estimates of the normalised length scales $\tilde{L}_x$. Note that the underlined values are those which are smaller, though all values (except that of $\tilde{L}_x^{(k)}$ and $\tilde{L}_x^{(\Sigma)}$ in (b) and (g) cases, respectively) generally fall within the qualitative estimates. In the case of the sheared homogeneous turbulent flow (f), no mean velocity was included in the dataset and thus $\tilde{L}_x^{(\Sigma)}$ has not been quantified.

Both values (i.e. those of $\widetilde{L}_X^{(\Sigma)}$ and $\widetilde{L}_X^{(k)}$) satisfy the previous qualitative estimate, in general. In case (d) shown in Table 5-2, for example, the quantitative estimates are of the order of 1, despite the fact that $\widetilde{L}_X^{(\Sigma)}$ is not exactly close to 1 (i.e. one does not necessarily have the scale $\widetilde{L}_X^{(\Sigma)} \approx 1$, which is of course a subset of all acceptable numbers that are of the order of 1).

The only exceptions are the cases where $\widetilde{L}_X^{(k)}$ and $\widetilde{L}_X^{(\Sigma)}$ in (b) and (g), respectively, do not fall within the qualitative approximate. These are instances where the turbulent kinetic energy k in the former case and the mean strain rate S in the latter case are very sensitive to non-local influences such that the inhomogeneity scales $\Lambda^{(k)}$ and $\Lambda^{(S)}$ (i.e. the scales over which S and k vary, respectively) are small in comparison to the length scale L_X;

$$L_X > \Lambda^{(S)}.$$

This phenomenon indicate that, for example, the corresponding flow (g) in the case of the flow over rearward facing step considered in this work cannot totally be considered as a free shear flow, in which strong non-local influence might have its role. As far as the scale $\Lambda^{(k)}$ is concerned however, the use of 'free shear flow' as the main flow type of reference [1] in this case is justifiable, where the previous estimate is satisfied. Indeed, the 'anomaly' in case (g) suggests that the choice of prediction method for the associated zone has to be made more carefully.

5.2 Normalised timescale

Clearly the normalised timescale defined by equation (4-15) was determined in a relatively straightforward manner by using the production and dissipation rate from the datasets. The results are presented in Figure 5-5.

(a)

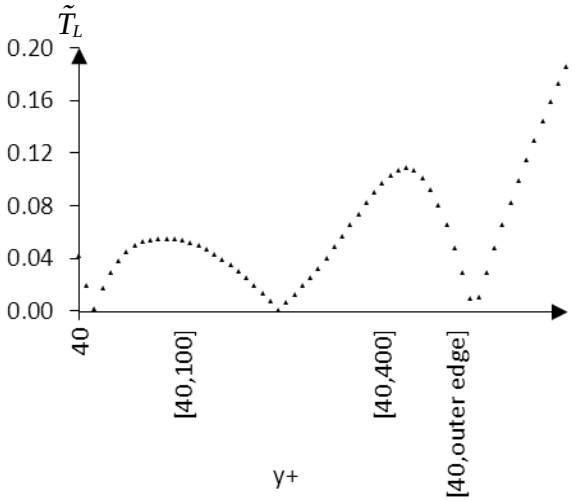

(b)

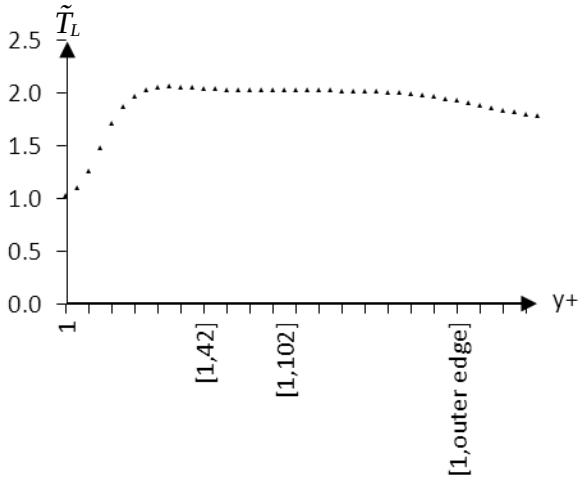

Figure 5-5 Variations of the normalised time scales $\tilde{T}_L$.
(Graphs are presented using a *fixed-point* approach.)
(a) Constant pressure boundary layer (DNS by Spalart, 1988) at $Re_{\delta^+} = 650$.
(b) Sink-flow (DNS by Spalart, 1986) at $Re_\theta = 690$, and with acceleration parameter K=1.5x10^{6}.

	Flow types	Region of interest	$\tilde{T}_L$ Quantitative	Qualitative
(a)	Constant pressure boundary layer	$40 \le y^+ \le 400$	0.10	$<<1$
(b)	Sink flow	$1 \le y^+ \le y^+_{\delta 0.99}$	1.92	$\gtrsim 1$
(c)	Flat plate transitional boundary layer	$0.1 \le y(mm) \le y_{\delta 0.99}$	0.34	~ 1
(d)	Shear layer impingement	$0 \le y / h \le 1$	0.62	~ 1
(e)	Channel flow	$0 \le y^+ \le y^+_{d/2}$	0.43	~ 1
(f)	Sheared homogeneous turbulent flow	$0 \le y \le 2.9$	1.08	$\lesssim 1$
(g)	Free shear flow	$0 \le y / h \le 3.45$	3.39	~ 1

Table 5-3 The quantitative and qualitative estimates of the normalised time scales $\tilde{T}_L$. All values fall within the qualitative estimates. Flows of reference [1] are as shown in Table 5-2.

5.3 Remarks on the 'localness' parameters

It is found that both 'localness' parameters (i.e. $\tilde{T}_L$ and $\tilde{L}_X$) do not necessarily agree with each other, as shown in §5.1 and §5.2 . In sheared homogeneous turbulent flow for example, non-local influences are rapid over time ($\tilde{T}_L > 1$), while their effects on, for instance, the mean strain rate change over the eddy length scale, are negligible ($\tilde{L}_X << 1$). Thus, in the former and latter situations, the turbulence is non-local in time and spatially local, respectively. Apart from free shear flows, the local (mixing length) models are valid for all other types of flow analysed in this work, even though the turbulence is temporally or spatially less or non-local, provided that the statistics of interest are those which need to be computed at a specific time $t = C$ (e.g. $\overline{u}(\boldsymbol{x}, C)$ and thence $\sigma_{ij}(\boldsymbol{x}, C)$ where C is a constant) in the kinematic studies if $\tilde{T}_L > 1$, $\tilde{L}_X << 1$ (where the turbulence is homogeneous), or at specific point $x=C$, e.g. $\langle u \rangle(C, t)$ if $L_X > 1$, $T_L < 1$. Note that in the former, the length scale over which the turbulence is correlated is relatively small and therefore the eddy structure is a local function of mean velocity gradients, and is not affected by, for instance, the

presence of the rigid surface, i.e. the turbulence satisfies the condition necessary for the validity of the models. It is important to note that the quantitative estimates are not necessarily correct if agree with the qualitative ones. Instead, it the quantitative estimates which shows whether the qualitative range is reasonable.

5.4 Degree of non-Gaussianity[8]

The degree of non-Gaussianity $\tilde{G}$ defined by equation (4-22) was determined by further manipulating the experimental results as well as those of the simulations. The choice of cases has been made on the basis of flows whose 'localness' and strain parameters were already quantified in Chapter 5. For instance, the experimental case of near wall layer beneath separated flow (around reattachment) can be related to the simulation case of flow over a rearward facing step (around reattachment), since they both can be referred to as shear layer impingement cases. Two selected experimental cases will be discussed in detail in §5.4.1 and §5.4.2, followed by a discussion on large eddy simulation (LES) cases in §5.4.3-§5.4.5 and that on a direct numerical simulation (DNS) case in §5.4.6.

5.4.1 Turbulent plane wake

The wind tunnel experiment was conducted by [81] to investigate the probability density distributions in the case of far plane turbulent wake created by a cylinder by means of digital processing hot-wire signals. Both 4^{th}- and 3^{rd}-order correlation functions for the 3-dimensional velocity fluctuations were measured and shown, in general. The exception was the skewness factors of the spanwise fluctuations which were not included in [81] since they are in all cases very near to zero, as expected for a stationary, 2-dimensional turbulence. The flatness K_i as well as skewness S_i factors needed in non-Gaussianity calculation at x/D=400 (where x and D are the streamwise axis and cylinder's diameter, respectively) have been extracted and tabulated in Table 5-4.

[8] Much of the work in §5.4 - 5.6 was presented in [82].

y/D	K_u	K_v	K_w
4.84	2.700	2.640	3.200
6.00	3.240	3.300	3.400
7.78	3.780	3.960	3.800
8.42	5.350	4.290	3.600
10.00	5.620	4.620	4.200
10.73	4.540	4.290	5.200
12.00	0.110	4.130	3.800

y/D	S_u	S_v
4.84	-0.600	0.520
6.00	-0.840	0.600
7.78	-1.020	0.680
8.42	-1.400	0.800
10.00	-1.400	0.960
10.73	-0.920	0.760
12.00	-0.880	0.080

Table 5-4 Quadruple and triple correlation functions collected from [81].

As a verification, both K_i and S_i have been re-plotted as shown in Figure 5-6. Note that the cylinder was 6.25mm in diameter and the free stream velocity was 6.46m/s

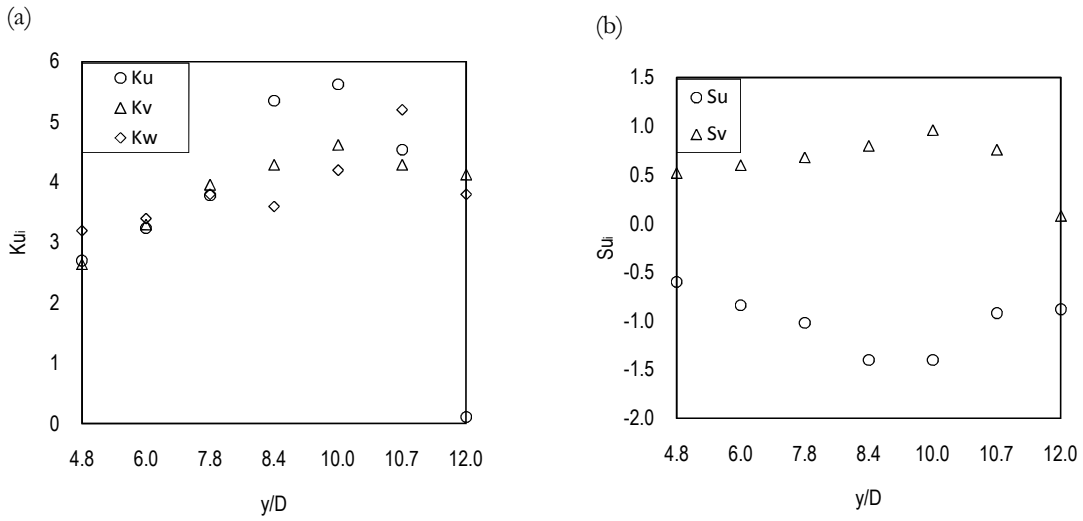

Figure 5-6 Correlation functions obtained from the experiment [81]. (a) 4th order correlations. (b) 3rd order correlations.

The degree of non-Gaussianity has then been calculated and its variation is shown in Figure 5-7 below;

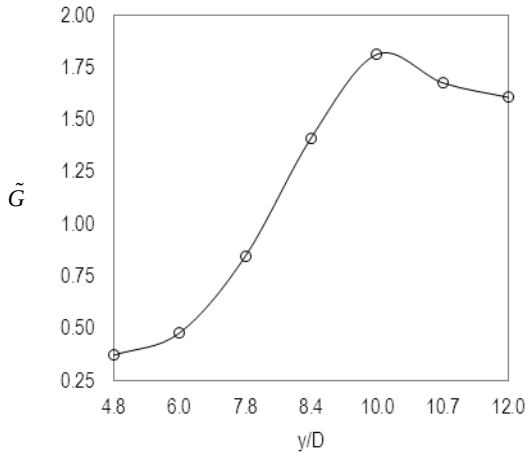

Figure 5-7 The variation with respect to the non-dimensionalised lateral coordinate in the far plane turbulent wake created by a cylinder at x/D = 400. Note that the coordinate origin is at the centreline of the wake.

By referring to [1], the empirical estimate of $\tilde{G}$ for free shear flows is of the order of 1 or smaller. The overall value of $\tilde{G}$ given in Figure 5-7 is 1.17, which agrees well with the estimate.

It is worth noting that the result of $\tilde{G}$ in this kind of flow is dominated by the flatness factors alone; by definition, the 3rd-order correlation of the velocity fluctuations' influence on $\tilde{G}$ is relatively weak.

5.4.2 Turbulent channel flow

All three components of the fluctuating velocity in a fully developed turbulent channel flow were measured by [71] using hot-film probes. The wall region was emphasised in their paper. Nevertheless, information for the whole channel width was also given.

Both 4th- and 3rd-order correlation functions for the 3-dimensional velocity fluctuations were measured and shown by them. Interestingly, unlike [81],

they measured and included the skewness factors of the spanwise fluctuations in their paper, and have successfully shown that such factors are very near to zero, as expected for a stationary, 2-dimensional turbulence.

The flatness K_i as well as skewness S_i factors along the cross stream – needed in non-Gaussianity calculation – at 32 channel widths between the channel's top cover and bottom, where the flow is fully developed, have been extracted and tabulated, and as a verification, K_i and S_i have been re-plotted (see Table B-4a and Figure B-4a in Appendix B).

Note that the channel is 8.5 m long, 0.22 m wide, and 0.79 m deep, and the flow is tripped at the entrance to the channel.

The degree of non-Gaussianity has then been calculated as indicated in Figure 5-8. This necessitates some points in Table B-4a (Appendix B) to be removed, and some others linearly interpolated.

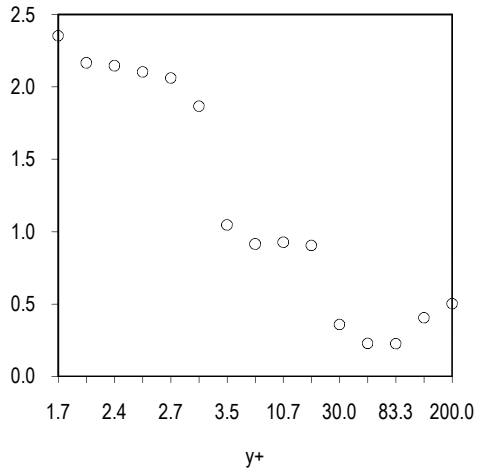

Figure 5-8 The variation of $\tilde{G}$ with respect to wall coordinate over channel half-width at Re=7700.

The results from Figure 5-8 above are summarised in the following table;

Region	$\tilde{G}$
$y^+ \lesssim 5$	$1.96\,(>1)$
$y^+ \approx 5$	$1.05\,(\sim 1)$
$5 \lesssim y^+ \le (\text{channel half}-\text{width})$	$0.61\,(\sim 0.5)$

Table 5-5 The results summary. Note that $y^+ \lesssim 5$ is the viscous sublayer zone.

Other experimental cases which have also been analysed for quantifying the degree of non-Gaussianity $\tilde{G}$ are:

(a) Boundary layer (before separation point) [83].
(b) Boundary layer under favourable pressure gradient [84].
(c) Zero-pressure-gradient boundary layer $(Re \approx Re_{trans})$ [85].
(d) Near wall layer beneath separated flow (around reattachment) [86].

The flatness K_i and skewness S_i factors in these flows are presented in Table B-4a – B-4f and Figure B-4(1) – B-4(6) in Appendix B. Table 5-11 in §5.6 shows both the quantitative and qualitative estimates of $\tilde{G}$.

5.4.3 Unsteady turbulent jet

Large eddy simulation (LES) has been used in [87] within an acoustic analogy approach in order to model a jet noise. In particular, the LES-predicted covariance and quadruple two-point two-time correlations for the streamwise velocity fluctuation are of primary importance in describing the acoustic sources. Both correlation functions R_{11} and $R_{11,11}$ at dx/D=0 (where x and D are streamwise axis and jet diameter, respectively) have been tabulated in Table 5-6, and as a verification, the data was re-plotted, as shown in Figure 5-9.

Note that the unsteady turbulent jet is that at $Re=10^6$ and Mach number of 0.75.

0.65 U_j/D dt	R_{11}	R_{1111}
0	1.000	1.000
0.1	0.825	0.750
0.2	0.570	0.300
0.3	0.360	0.120
0.4	0.210	0.050
0.5	0.110	0.017
0.6	0.025	0.001
0.7	-0.025	-0.004
0.8	-0.065	-0.012
0.9	-0.095	-0.020

Table 5-6 Covariance and quadruple correlation functions collected from[87]. Note that U_j/D dt is the dimensionless time, where U_j is the mean jet velocity.

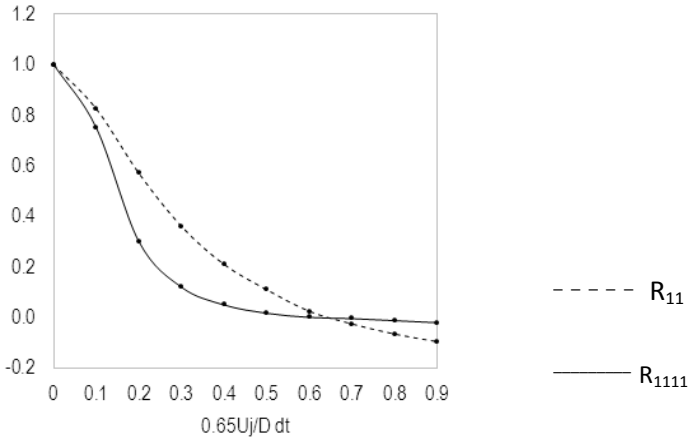

Figure 5-9 Large eddy simulation (LES) predicted covariance and quadruple correlation functions

Based Figure 5-9 above, the values of other significant components (R_{2222}, R_{3333}) needed in 'flatness' calculations were extracted;

0.65 U_j/D dt	R_{2222}	R_{3333}	R_{1212}	R_{2323}
0	0.350	0.300	0.400	0.150
0.1	0.263	0.225	0.300	0.113
0.2	0.105	0.090	0.120	0.045
0.3	0.042	0.036	0.048	0.018
0.4	0.018	0.015	0.020	0.008
0.5	0.006	0.005	0.007	0.003
0.6	0.000	0.000	0.000	0.000
0.7	-0.001	-0.001	-0.002	-0.001
0.8	-0.004	-0.004	-0.005	-0.002
0.9	-0.007	-0.006	-0.008	-0.003

Table 5-7

The degree of non-Gaussianity (based on the flatness term only) was then calculated;

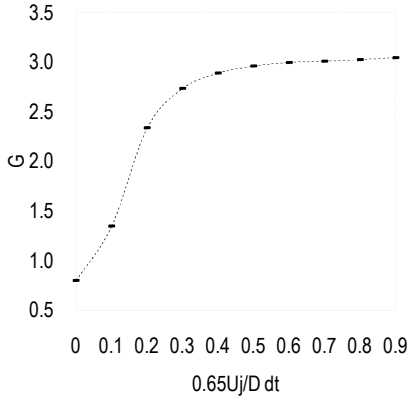

Figure 5-10 The Variation of $\tilde{G}$ for a streamwise separation vector dx/D = 0 in the middle of the shear layer downstream of the nozzle (x = 0) at x/D = 4.

Note that the empirical estimate of $\tilde{G}$ for free shear flows is comparable or smaller than one [1]. Taking into account the uncertainty bounds, the quantitative values of $\tilde{G}$ given in Figure 5-10 agrees well with the estimate.

It is worth having plots at dx/D = 0.2, dx/D = 0.4, and dx/D = 0.6 as well. The data is shown in Table 5-8.

	dx/D=0					dx/D=0.2				
0.65 Uj/D dt	R_{1111}	R_{2222}	R_{3333}	R_{1212}	R_{2323}	R_{1111}	R_{2222}	R_{3333}	R_{1212}	R_{2323}
0	1.000	0.350	0.300	0.400	0.150	0.200	0.070	0.060	0.080	0.030
0.1	0.750	0.263	0.225	0.300	0.113	0.500	0.175	0.150	0.200	0.075
0.2	0.300	0.105	0.090	0.120	0.045	0.700	0.245	0.210	0.280	0.105
0.3	0.120	0.042	0.036	0.048	0.018	0.550	0.193	0.165	0.220	0.083
0.4	0.050	0.018	0.015	0.020	0.008	0.320	0.112	0.096	0.128	0.048
0.5	0.017	0.006	0.005	0.007	0.003	0.150	0.053	0.045	0.060	0.023
0.6	0.001	0.000	0.000	0.000	0.000	0.050	0.018	0.015	0.020	0.008
0.7	-0.004	-0.001	-0.001	-0.002	-0.001	0.009	0.003	0.003	0.004	0.001
0.8	-0.012	-0.004	-0.004	-0.005	-0.002	-0.002	-0.001	-0.001	-0.001	0.000
0.9	-0.020	-0.007	-0.006	-0.008	-0.003	-0.010	-0.004	-0.003	-0.004	-0.002

	dx/D=0.4					dx/D=0.6				
0.65 Uj/D dt	R_{1111}	R_{2222}	R_{3333}	R_{1212}	R_{2323}	R_{1111}	R_{2222}	R_{3333}	R_{1212}	R_{2323}
0	0.050	0.018	0.015	0.020	0.008	-0.025	-0.009	-0.008	-0.010	-0.004
0.1	0.080	0.028	0.024	0.032	0.012	0.000	0.000	0.000	0.000	0.000
0.2	0.150	0.053	0.045	0.060	0.023	0.030	0.011	0.009	0.012	0.005
0.3	0.300	0.105	0.090	0.120	0.045	0.090	0.032	0.027	0.036	0.014
0.4	0.400	0.140	0.120	0.160	0.060	0.175	0.061	0.053	0.070	0.026
0.5	0.350	0.123	0.105	0.140	0.053	0.275	0.096	0.083	0.110	0.041
0.6	0.250	0.088	0.075	0.100	0.038	0.300	0.105	0.090	0.120	0.045
0.7	0.170	0.060	0.051	0.068	0.026	0.260	0.091	0.078	0.104	0.039
0.8	0.110	0.039	0.033	0.044	0.017	0.190	0.067	0.057	0.076	0.029
0.9	0.080	0.028	0.024	0.032	0.012	0.125	0.044	0.038	0.050	0.019

Table 5-8 Quadruple correlation functions collected from [87]. Note that U_j/D dt is the dimensionless time, where U_j is the mean jet velocity.

The corresponding plots are presented in Figure 5-11). The combined results would provide the variation with respect to space, and be used to compare with the $\tilde{G}$ plot for a round jet in co-flow [88] at r = 3mm and r = 15mm.

Unfortunately, however, the triple correlation of the velocity fluctuations is not of interest in jet noise prediction, and hence, the skewness-based measure was unable to be calculated.

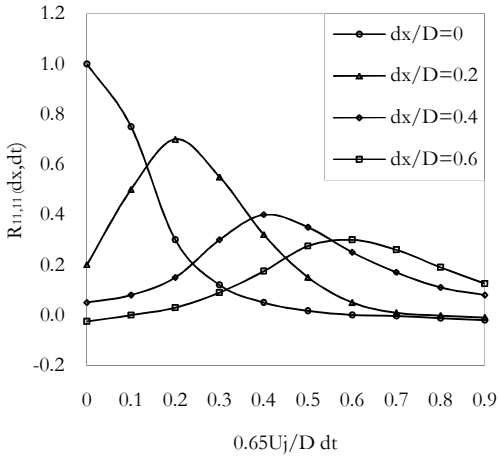

Figure 5-11 Large eddy simulation (LES) predicted quadruple correlation functions

The degrees of non-Gaussianity (based on flatness term only) were then calculated;

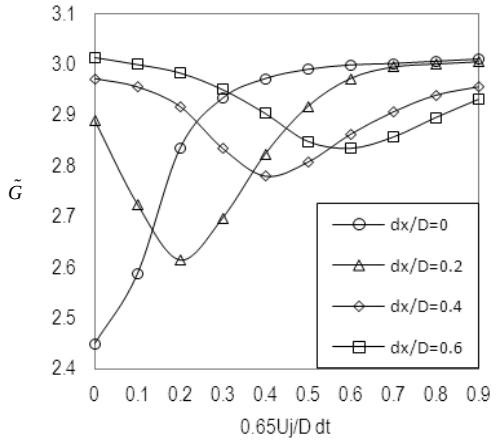

Figure 5-12 The variation of $\tilde{G}$ for various streamwise separation vectors in the middle of the shear layer downstream of the nozzle (x = 0) at x/D = 4.

The empirical estimate of $\tilde{G}$ for free shear flows is of the order of 1 or smaller [1]. Taking into account the uncertainty bounds, the overall converged value of $\tilde{G}$ (i.e. at $0.65\,U_j/D\,dt \approx 0.9$) given in Figure 5-12, is around 2.98, and agrees well with the estimate. The skewness-based measure was unable to be calculated in the present analysis, since the triple correlation of the velocity fluctuations is not of interest in jet noise prediction.

5.4.4 A round jet in co-flow

Large eddy simulation dataset of [88] has been analysed for the quantified degree of non-Gaussianity $\tilde{G}$. In the cases where the radial distances r=0mm, and r=3mm, $\tilde{G}$ is of the order of 1 or smaller along z-axis, including both in the near-field and far-field of the jet (see Figure 5-13 (a),(b)).

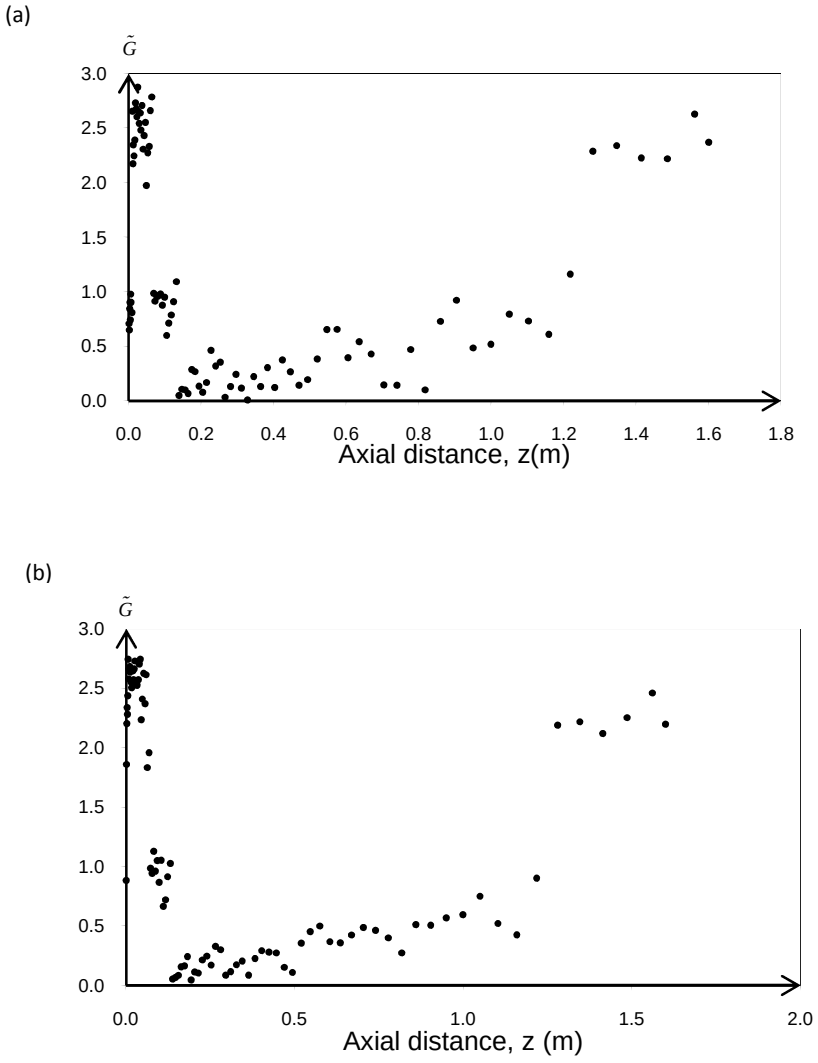

Figure 5-13 Variations of non-Gaussianity parameter, denoted by $\tilde{G} = \max\left\{\overline{u_i^4}\Big/\left(\overline{u_i^2}\right)^2 - 3, \overline{u_i^3}\Big/\left(\overline{u_i^2}\right)^{3/2}\right\}$, at different radial distances r along a round jet in co-flow (*large eddy simulation dataset of* [88]). (a) r = 0 mm (core jet centre line) (b) r = 3 mm (centre of the initial mixing layer from the exit).

Turbulence fluctuations exhibit a relatively smaller deviation from Gaussian distribution (such that $\tilde{G} \approx 0$) near the tip of the jet core (at $z \approx 0.24\,\mathrm{m}$), in comparison with the fluctuations near the jet exit.

When r=15mm, non-Gaussian distribution is relatively higher near the jet edge at $z \approx 0.1\,\mathrm{m}$, as shown in Figure 5-14(a), although $\tilde{G}$ is still of the order of or smaller than 1.

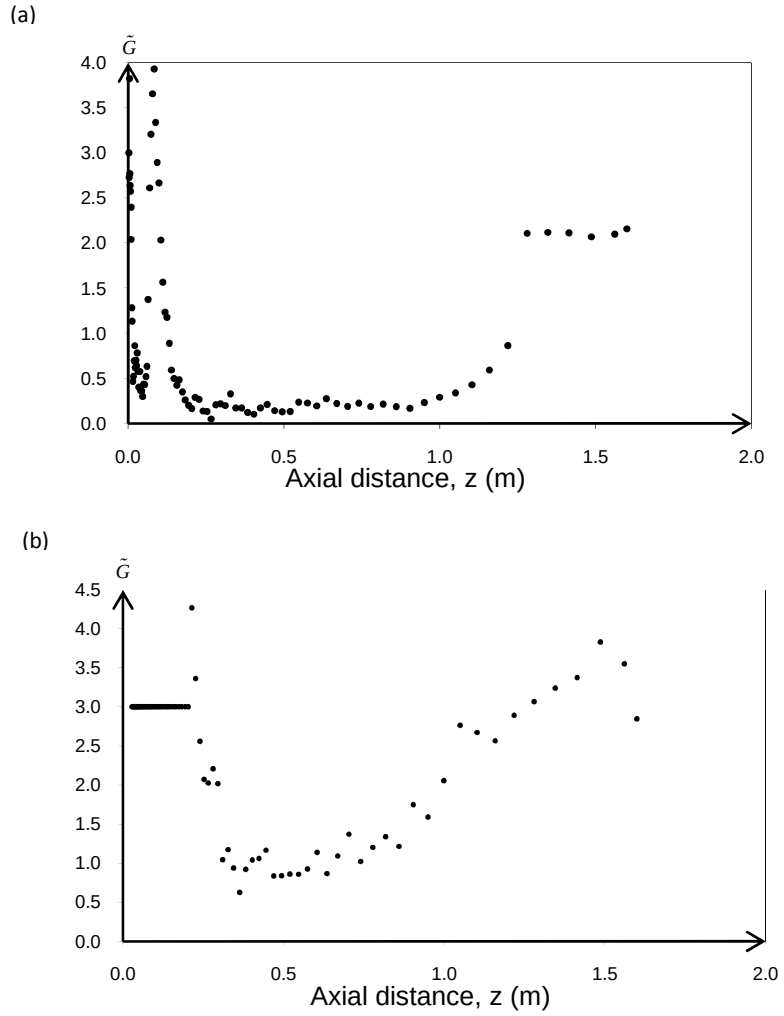

Figure 5-14 Variations of non-Gaussianity parameter $\tilde{G}$ at (a) r = 15 mm, and (b) r = 50 mm, along a round jet in co-flow (*large eddy simulation dataset of* [88])

The variations of $\tilde{G}$ in co-flow, instead of the jet (i.e. when r=50mm) is exhibited in Figure 5-14(b). Note that there is no turbulence at z < 0.03 m. The quadruple and triple correlations are zero at $0.03\text{m} \le z \le 0.20\text{m}$ such that the initial part of the curve has a zero slope.

In general, the parameter falls into the qualitative range for the round jet in co-flow. Note that the qualitative estimate [1] (for a free shear flow) is $\tilde{G} \lesssim 1$.

5.4.5 Fully developed single round jet

To compute the low-velocity round jet flow development, the computational fluid dynamics (CFD) technique of large eddy simulation (LES) has been utilised by [76]. The small-scale (unresolved) turbulent motions are computed by using the dynamic Smagorinsky model that assumes the isotropicity of the small scales. The filter (i.e. scale separation) must then lie well inside the inertial sub-range (i.e. $k^{-5/3}$ slope of the energy spectra).

The grid used for this simulation fulfils the above requirement, where the mean streamwise velocity $\bar{u}$ and the variance of the streamwise velocity fluctuations (i.e. $\overline{u'^2}$) obtained from the experimental data agree well with the LES results of [76].

The details of the simulation are as follows:

D $=0.00635$m,
U_b $=23$m/s,
I $=5.17\%$,
$U_{f\text{-}s}$ $=5$m/s,

where D, U_b, I, and $U_{f\text{-}s}$ are the radius of the jet, bulk velocity at the inlet of the computational domain, turbulence intensity, and free stream velocity, respectively. Note that a laminar boundary layer profile following the $1/7^{th}$ power law is used at the inlet of the domain where the turbulence intensity I is superimposed. Also, the domain is sufficiently long to avoid any influence of the 'outflow' boundary at the exit on the region of interest (i.e. the

intermediate downstream locations x/D=15,20,25 for the statistical analysis). Such influence only takes place in very close proximity. The turbulent kinetic energy is still at high level, and the transition to a fully turbulent state has completed at the region of interest.

The flow is first initialised by leaving the jet flowing for 0.06 seconds, and then the sampling process begins. The simulation is run for 0.15 more seconds in order to assure a good averaging quality.

The mean velocity vector is calculated by

$$\overline{u}_i = \frac{\sum_{i=1}^{n} u_i}{n},$$

where u_i and n are the instantaneous velocity vector and the number of samples counted in averaging (taken every 1.5e-5s), respectively. The velocity fluctuation vector $u_i' = u_i - \overline{u}_i$ can then be instantly computed, and is used to compute $u_i'^2, u_i'^3, u_i'^4$ and ε. By following the same averaging process, time-averaged values for these quantities (i.e. $\overline{u_i'^2}, \overline{u_i'^3}, \overline{u_i'^4}$) are obtained. The process of averaging lasts for more than 0.25s; it is much more difficult for these quantities to be averaged well in comparison to the mean velocities $\overline{u}_i$. At the end of the simulation, the time averaged production of k is evaluated.

Note that Fluent calculates the spatial derivatives required for the computation of the above statistical quantities at the beginning of every iteration step. This involves user defined function (UDF) utilisation.

Three-dimensional cross of data at the centre of the mixing layer at x/D=15,20,25 is extracted in order to analyse all three Cartesian directions; every direction effectively accounting for the streamwise, radial and z modes of the jet.

The results of the quantified non-Gaussianity parameter $\tilde{G}$ are presented by Figure 5-15.

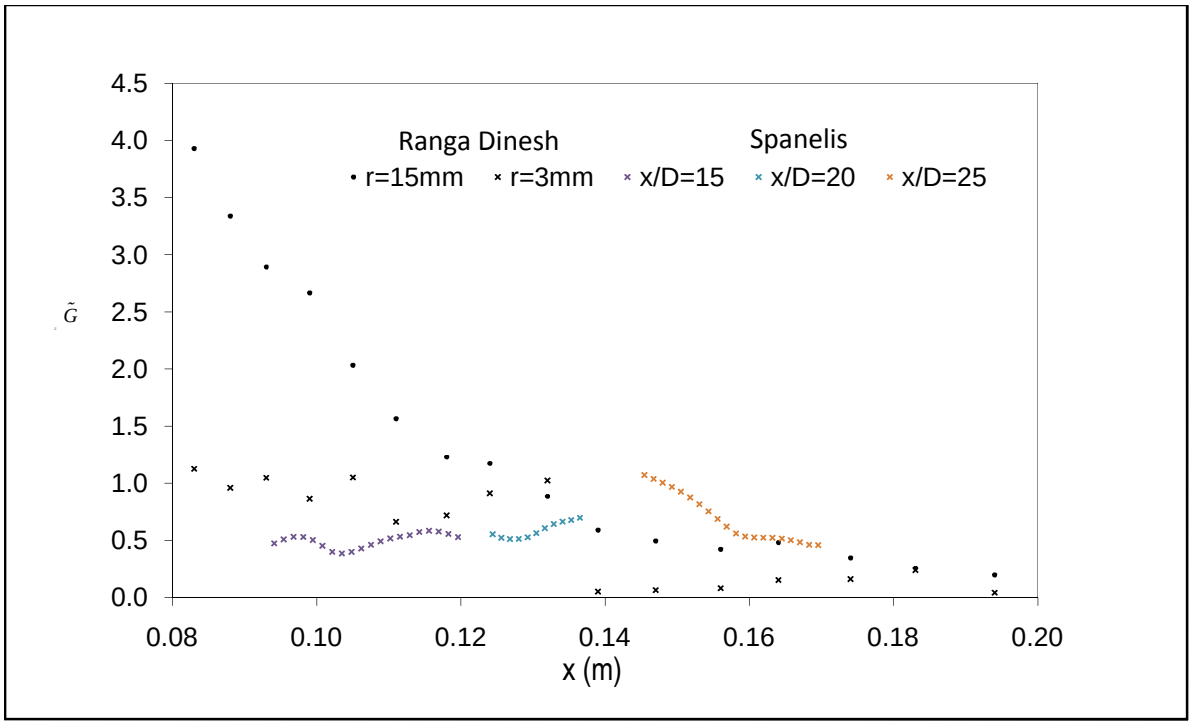

Figure 5-15 Degree of Non-Gaussianity in single round jets simulated by Spanelis [76] and Ranga Dinesh [88].

The locations where the data are extracted (i.e. at x/D=15,20,25) are those in the middle of the mixing layer or within the fluctuating fluid interface between turbulent (i.e. the jet) and non-turbulent motion (i.e. the free stream), where the turbulence structure is close to 'normal', such that the overall value of $\tilde{G}$ in this case is 0.63 (see Figure 5-15). The result produced by [88] at r=15mm confirms that the small scale rotational turbulence becomes intermittent at $x \le 0.12\text{m}$ near the interface, and the probability density function of velocity fluctuations becomes skewed, with relatively high flatness. However, within the fluctuating interface (i.e. at $x > 0.12\text{m}$) the turbulence structure is close to Gaussian, so that the statistics of the turbulence at a given point depend greatly on how often that point is on the turbulent or non-turbulent side of the interface.

5.4.6 Extracting higher-order correlations by means of master-modes in 3D turbulent channel

The main idea for obtaining higher-order correlations by means of master-modes in 3D turbulent channel is to avoid running full DNS. This is possible because in a master-mode-set, the turbulent flow fields are represented by basic functions that give the time history of the entire flow. Since the original codes used in the master-modes were meant for computing second-order two-point correlations, such codes have been modified to in order to quantify the degree of non-Gaussianity $\tilde{G}$. This has been done by firstly combining the master-modes computation with the post-analysis, and secondly, by running the code separately for different outputs (where each of the outputs has been produced in one single computation step). Such actions are important in order to reduce the risk of making unrealised mistakes while editing or modifying the original code, and to be able to detect any mistakes easily.

There are seven steps involved in this extraction. In the first three steps, the second-, third-, and fourth-order correlations are calculated. These correlations, in particular those of a higher-order, need to be normalised later on.

The fourth step is unique, since it involves running the original code without being edited or modified as in the previous steps, and it also gives an idea of how the correlations are normalised so as to have the 'correlation functions' from the next steps. The outputs are the second-moments (i.e. the second-order correlation functions).

Note that a subroutine is used to compute single-point second-order correlations, as well as two-point correlations. The former is only necessary for normalisation, and it is not possible to have single-point higher correlations with this subroutine. Even if $\mathbf{u}_i^4(\mathbf{x})$, for instance, can be obtained, its ensemble averaging $\langle \mathbf{u}_i^4(\mathbf{x}) \rangle$ is not a procedure which has been

programmed into the master-modes. Therefore, the wider function of such a subroutine is to take the ensemble average of two-point correlations including the higher order two-point moments.

The last three steps determine:

(1) the correlation functions (i.e. both third- and fourth- moments) based on the previous outputs,
(2) the non-Gaussianity, in terms of skewness and flatness, in each fluctuating velocity component distribution (i.e. that of u_1, u_2, u_3, respectively), then,
(3) the averaged value of the degree of non-Gaussianity $\tilde{G}$ at each 'corresponding' meshing point.

Detailed information about the computation is presented in Appendix C. The results are shown in Figure 5-16 and Figure 5-17. Since all skewness and flatness values vanish, then, by definition, the quantified degree of non-Gaussianity $\tilde{G}$ in this flow case is 3. Note that higher-order correlations extracted by means of master-modes in serve as a basis to support and check the results of the analysed experimental data (i.e. that in turbulent channel flow).

(a)

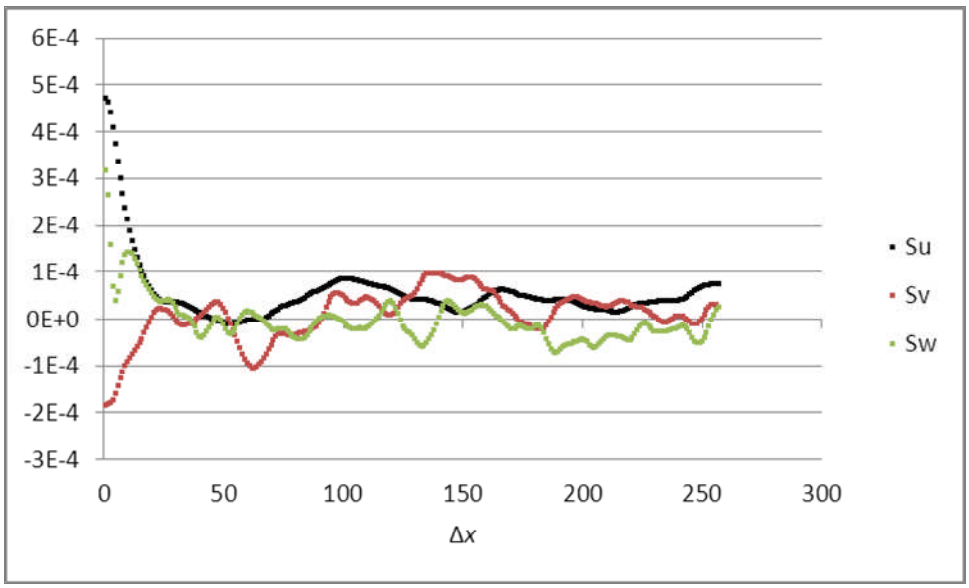

(b)

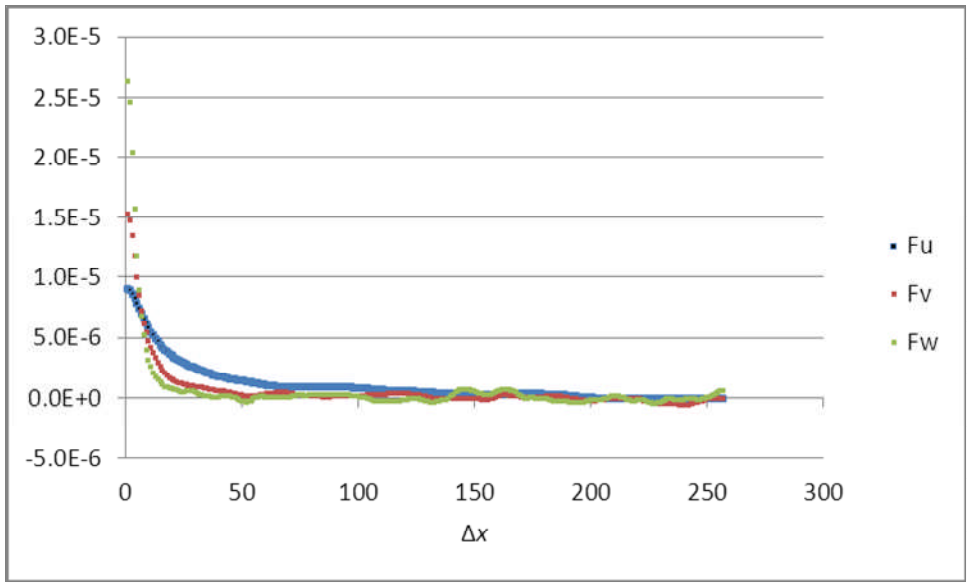

Figure 5-16 Streamwise ($\Delta y = 0$) two-point higher correlations, master-mode set; skewness S_i or R_{iii}, i=u,v,w, and Kurtosis K_i or R_{iiii}, i=u,v,w (i.e. longitudinal, spanwise, and wall-normal fluctuating velocity correlations, respectively). For $Re = 360$, $z^+ = 5.6$, $L_x \times L_y = 6 \times 3$.

(c)

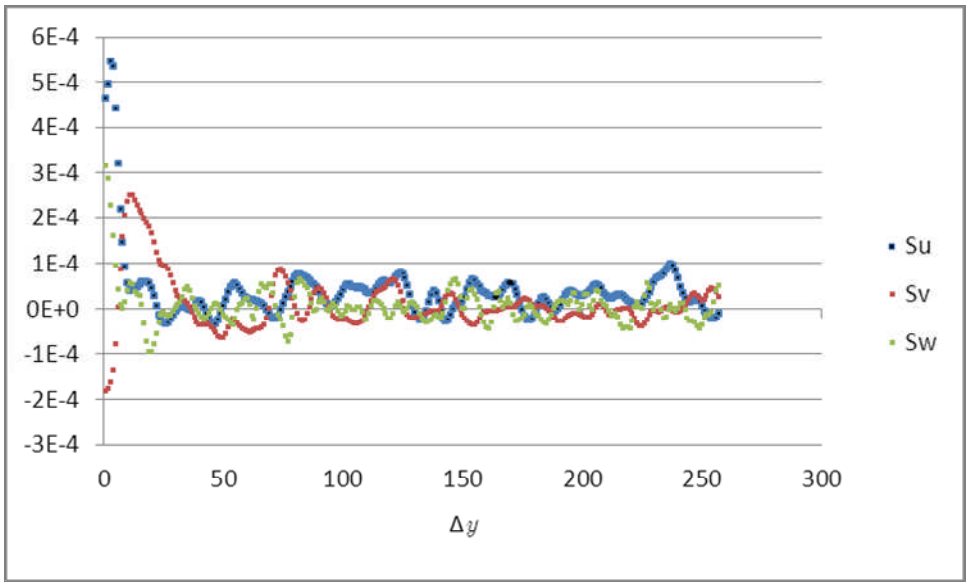

(d)

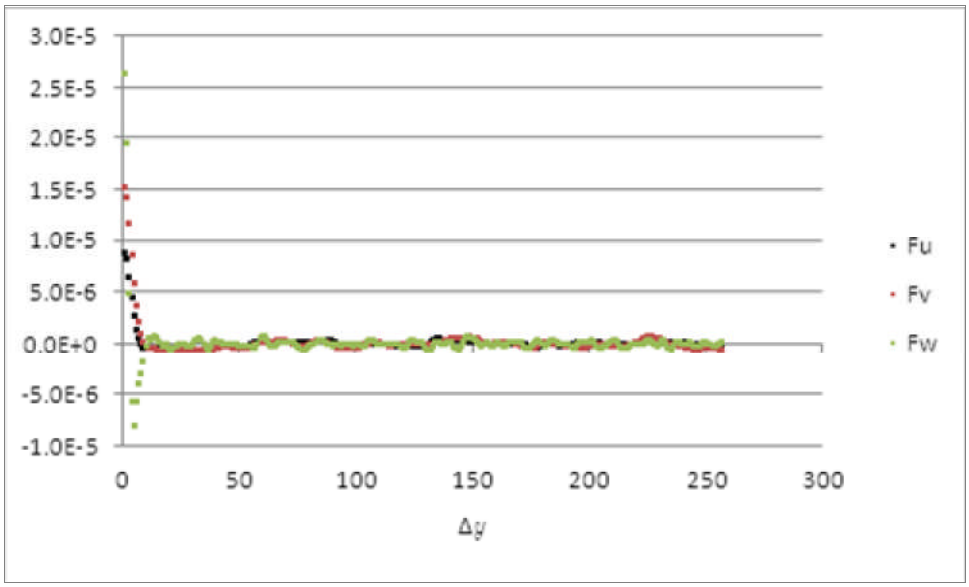

Figure 5-17 Spanwise ($\Delta x = 0$) two-point higher correlations.

5.5 Strain parameter

The other of the two structural statistical parameters $\tilde{S}$ is analysed and discussed in this section. First, let us consider the strained channel DNS data [79]. Unlike most of the data stored in a database (e.g. ERCOFTAC database), these data include not only the mean velocities at each grid point, but also their gradients in the form of partial derivatives (i.e. $\partial_y \bar{u}$ and $\partial_y \bar{v}$). This enables us to check the accuracy of equations (4-19)-(4-21) used in determining the strain parameter $\tilde{S}$. The *segment-by-segment* and *fixed-point* approaches have been used, and the results are as shown in Figure 5-18.

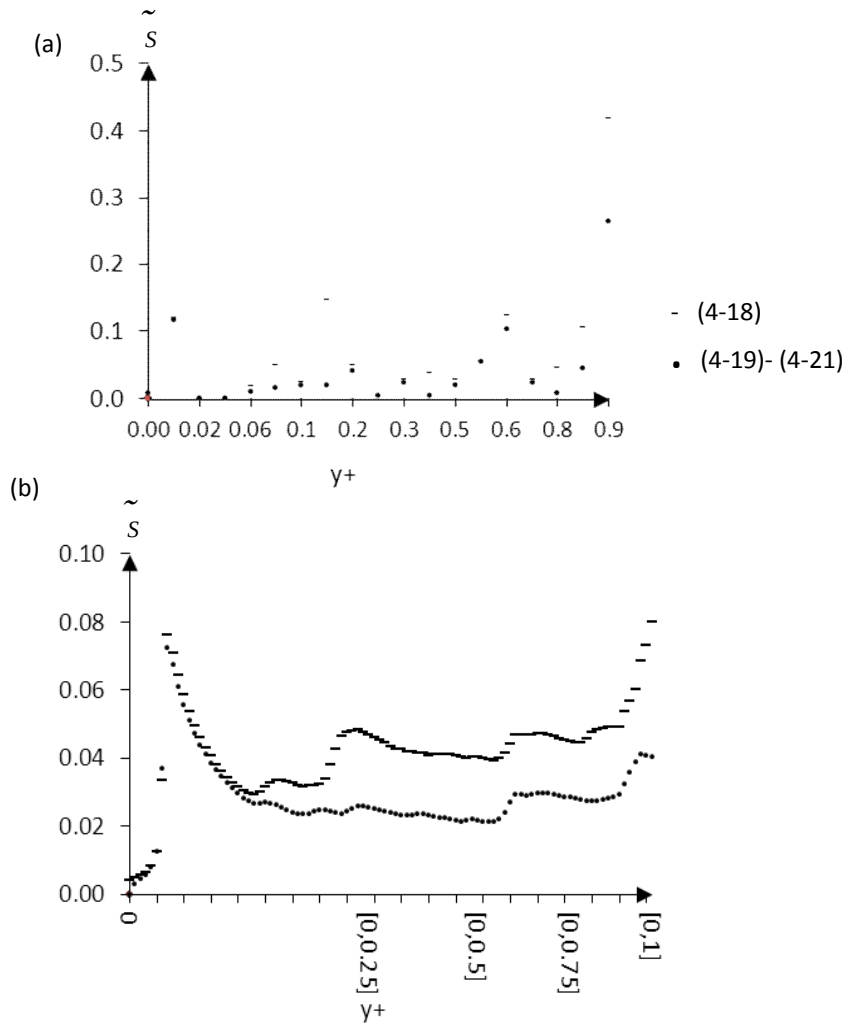

Figure 5-18 Variations of the strain parameter $\tilde{s}$ in strained channel flow at dimensionless time At = 0.77, as predicted both by **(4-18)** and **(4-19)**-**(4-21)**. (a) 'Segment-by-segment' . (b) 'Fixed-point'.

Figure 5-18a indicates that, in general, both sets of equations agree well. The difference between both plots is more pronounced at $y^+ \approx 0.05$, and $y^+ \geq 0.8$ which is covered by coarse grid points. The average value of $\tilde{S}$ is 0.07 (the qualitative estimate for $\tilde{S}$ in a strained turbulence is $0 \leftrightarrow 1$).

Similarly, Figure 5-18b shows that there is a good agreement between the profiles. Both sets of equations collapse well in the region where $0 \leq y^+ \leq 0.05$ after which they begin to slightly depart from each other.

5.5.1 Two groups of flows

Apart from the strained channel flow case discussed in the preceding section, the other two cases in which $\tilde{S} \neq 0$ are those of shear layer impingement and free shear flow [67] (see Figure 5-19), where $\tilde{S} > 1$. The parameter $\tilde{S} = 0.04$ in the former case, indicates that the effects of mean strain rate Σ are slightly higher than those of mean rate of rotation Ω. In the latter case $\tilde{s}$ is greater, i.e. $\tilde{S} = 0.24$. Nevertheless, this does not mean that the mean strain rate effects in free shear flow are greater in comparison to those in flow involving shear layer impingement. It rather suggests that the difference between the magnitude of Σ and that of Ω is greater in free shear flow. In other words, the discovery that $\tilde{S}$ is higher in free shear flow does not invalidate the fact that in the case of shear layer impingement, the magnitudes of Σ and Ω are much higher, since in the latter case, the 'impingement' takes place around the reattachment point, where both the curved flow and blocking effects play important roles. Note that, given two different types of flow with different values of $\tilde{s}$, the aim is to investigate dominant types of straining in each flow, rather than to directly observe the values of Σ and Ω.

Such a non-vanishing strain (i.e. $\tilde{S} \neq 0$) dynamically signifies the presence of external influences. If $\tilde{S}$'s magnitude is large enough (i.e. $|\tilde{S}| \geq 1/10$), and $\tilde{L}_X^{(\Sigma)} = L_X / \Lambda^{(\Sigma)} > 1$, the sensitivity of local models like EVM is considerably affected. In this case, several studies (e.g. [34]) have demonstrated how the

models can over-predict the effect of straining on the growth of k, since the turbulence is not entirely determined by the local velocity gradient.

(a)

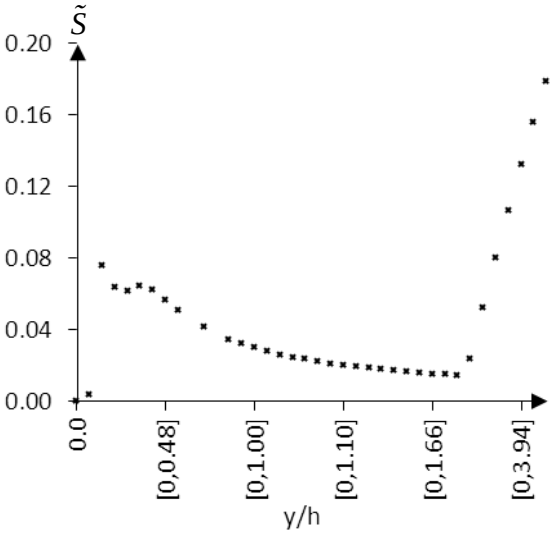

(b)

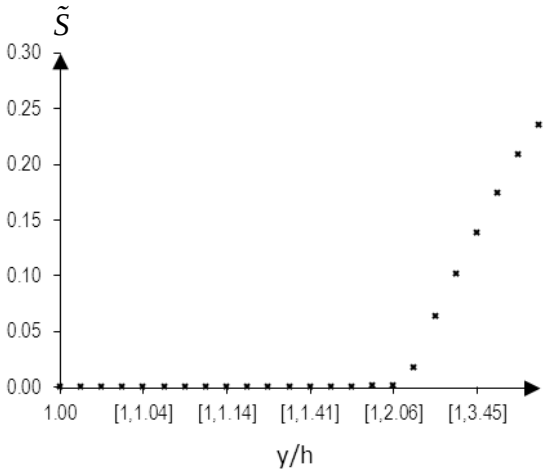

Figure 5-19 (a) Shear layer impingement (around reattachment) at Re_h = 5100, where h is the step height. Note that the y-coordinate is non-dimensionalised by h. The region of interest is $0 \le y/h \le 1$ outside which the impingement phenomenon is not supposed to be observed. The strain parameter $\tilde{s}$ in this range takes the value of 0.03 which falls into the qualitative estimate of the order of, or smaller than, 1. (b) Free shear flow at Re_h = 5100.

In the rest of the cases (i.e. [64-69]), where the only non-zero (mean) velocity gradients included in the datasets are $\partial_y \overline{u}$, $\widetilde{S}$ vanishes (see (4-18)).

The finding that $\tilde{s} = 0$ does not suggest that there is no mean strain rate Σ (or mean rate of rotation Ω), but rather that $\Sigma \approx \Omega$ such that dominant types of straining are negligible. This can be expected in cases of turbulent flow that are undergoing pure shear.

5.5.2 The impinging effect of shear layer on the straining parameter

The rearward-facing step datasets serve as a basis for testing the reliability of the approach used to quantify the strain parameter $\tilde{S}$. This section is unique in this sense, and contains the related information (i.e. various values of $\tilde{S}$. at different stations in the case of shear layer impingement).

One of the basic flows listed in [1] is the jet impaction for which the empirical estimate of $\tilde{S}$. is of the order of, or smaller than, 1. In quantifying the straining parameter $\tilde{S}$. for the shear layer impingement around the reattachment location in rearward-facing step flow, it can be considered as the flow of reference. It is shown in the previous discussion that in this case, the quantitative value of $\tilde{S}$. is 0.04. It was then hypothesised that such a low value of the order of 1/100 reflects the low impaction phenomenon. If this is true, then the straining cannot be more pronounced prior to and after the mean reattachment location, where the impingements, if any, are not more significant. The results are shown in Figure 5-20 and Table 5-9.

Based on Table 5-9, the highest value of the strain parameter $\tilde{S}$ is that around the mean reattachment location. Since the station x=1.67ℓ is not included in the region of reattachment, hence the parameter $\tilde{S}$ around it is the smallest one.

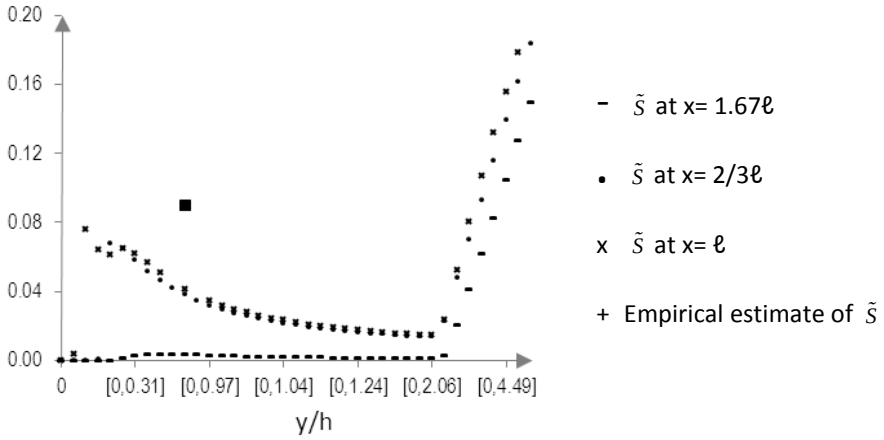

Figure 5-20 The calculated variations of the straining parameter $\tilde{S}$ around the mean reattachment location at four different stations, based on the DNS dataset of the flow over rearward-facing step (Le & Moin, 1997) at $Re_h = 5100$, where h is the step height. Note that the symbol ℓ denotes the mean reattachment length. The station of reference is at x= ℓ, which is the mean location of the reattachment.

		$\tilde{S}$				
		Quantitative			Qualitative	
Flow type	Interested region	x= 2/3ℓ	x= ℓ	x=1.67ℓ		Flow of reference
Shear layer impingement	$0 \le y/h \le 0.88$	0.0379	0.0411	0.0035	$\lesssim 1$	Jet impaction

Table 5-9 The quantitative and qualitative estimates of the straining parameter $\tilde{s}$.

5.6 Overall results for the quantified 'localness'-structural parameters

Overall results are presented by Table 5-9 (DNS cases), Table 5-11 (experimental cases), and Table 5-12 (LES and master-modes cases).

	Flow types	Interested region	Quan. $\tilde{L}_x^{(k)}$	Quan. $\tilde{L}_x^{(\Sigma)}$	Qual. $\tilde{L}_x$	$\tilde{T}_L$ Quan.	$\tilde{T}_L$ Qual.	$\tilde{S}$ Quan.	$\tilde{S}$ Qual.	Flows of reference
(a)	Constant pressure boundary layer	$40 \le y^+ \le 400$	<u>0.53</u>	1.20	$\sim 1/2$	0.10	$<< 1$	0.00	$<< 1$	Turbulent boundary layer (near a wall)
(b)	Sink flow	$1 \le y^+ \le y^+_{\delta 0.99}$	0.96	<u>0.64</u>	$<< 1$	1.92	$\gtrsim 1$	0.00	$0 \leftrightarrow 1$	Strained turbulence
(c)	Flat plate transitional boundary layer	$0.1 \le y(mm) \le y_{\delta 0.99}$	<u>1.79</u>	3.68	$\gtrsim 1$	0.34	~ 1	0.00	$\lesssim 1$	Large scale free stream turbulence interacting with a boundary layer
(d)	Shear layer impingement	$0 \le y/h \le 0.88$	<u>1.84</u>	4.47	~ 1	0.62	~ 1	0.04	$\lesssim 1$	Jet impaction
(e)	Channel flow	$0 \le y^+ \le y^+_{d/2}$	<u>1.50</u>	1.82	~ 1	0.43	~ 1	0.00	$\lesssim 1$	Turbulent boundary layer (near outer boundary)
(f)	Sheared homogeneous turbulent flow	$0 \le y \le 2.9$	0.002 $\approx$ 0.00	-	$<< 1$	1.08	$\lesssim 1$	-	$\lesssim 1$	Homogeneous stationary turbulence
(g)	Free shear flow	$0 \le y/h \le 3.45$	<u>2.38</u>	16.06	~ 1	3.39	~ 1	0.24	$\lesssim 1$	Free shear flows and separated flows

Table 5-10 Quantitative and qualitative estimates of the normalised statistical parameters. Note that the underlined values are those which are the smaller of two types of normalised length scales (*i.e.* $\tilde{L}_X{}^{(k)}$ and $\tilde{L}_X{}^{(\Sigma)}$)

	Flow types	Region of interest	$\tilde{G}$ Quan.	Qual.	Flows of reference [1]
(a)	Boundary layer (before separation point)	$27 \le y^+ \le 344$	0.49	0	Turbulent boundary layer (near a wall)
(b)	Boundary layer under favourable pressure gradient	$12 \le \delta^+ \le 30$	0.47	0	Strained turbulence
(c)	Zero-pressure-gradient boundary layer $\left(Re \approx Re_{trans}\right)$	$0.06 \le y/\Delta \le 0.23$	1.58	0	Large scale free stream turbulence interacting with a boundary layer
(d)	Near wall layer beneath separated flow (around reattachment)	$2 \le y^+ \le 158$	0.24	$\ll 1$	Jet impaction
(e)	Channel flow	$5 < y^+ < 200$	0.61	$\lesssim 1$	Turbulent boundary layer (near outer boundary)
(f)	Far plane wake	$5 \le y/D \le 12$	1.17	$\lesssim 1$	Free shear flows and separated flows

Table 5-11 The quantitative and qualitative estimates of the degree of non-Gaussianity $\tilde{G}$
(Experimental cases)

	Flow types	Quan. $\tilde{G}$	Qual.	Flows of reference [1]
(a)	Unsteady turbulent jet	2.98	$\lesssim 1$	Free shear flows and separated flows
(b)	A round jet in co-flow	1.31		
(c)	Fully developed single round jet	0.63		
(d)	Turbulent channel flow	3.00		Turbulent boundary layer (near outer boundary)

Table 5-12 The quantitative and qualitative estimates of the degree of non-Gaussianity $\tilde{G}$
(LES and master-modes cases)

6

The quantitative flow parameters as a guidance framework for prediction methods

Methods of prediction discussed in this chapter are meant for turbulent flows which have been initially considered to address the types identified in [1], and already described in Chapter 3. Although the values of dominant physical parameters in these flows (in particular $\tilde{L}_X$, $\tilde{T}_L$, and $\tilde{S}$) become specific, generic flow properties can be clearly defined once they have been quantified. It will be shown in the following sections that the normalised length scale $\tilde{L}_X$, for instance, can be used to determine whether a given flow is spatially local, i.e. when $\tilde{L}_X < 1$, or non-local, i.e. when $\tilde{L}_X \geq 1$. Prior to the quantification, it might not be very clear whether or not the turbulence is local (e.g. when $\tilde{L}_X$ is "of order one or smaller"). The turbulence models proposed here can be used to predict some UFRs based on the combination of $\tilde{L}_X$, $\tilde{T}_L$, and $\tilde{S}$. However, it should be noted that a more general 'framework' consideration for the UFRs, and hence ACs, is proposed in Chapter 7. The current chapter is necessary mainly to firmly connect the quantitative parameter estimates (as discussed in Chapter 5) to the models.

Constant pressure boundary layer

The single-point models of turbulence are clearly valid near the 'wall' in the case of turbulent boundary layer (outside the viscous sublayer zone in which the mean velocity approaches a linear laminar form when $x_2 \ll x_{20}$, where x_{20} is the roughness length defined by x_{20} of the order of ν/u^*). Here the large scale structure of turbulence is approximately local in space and time, i.e. $\tilde{L}_X = 0.5 < 1$ and $\tilde{T}_L = 0.1 < 1$, and is approximately Gaussian. Clearly the turbulence is nearly homogeneous. Also the straining is obviously dominated by pure shear such that $\tilde{S} = 0.$

The use of the mixing length model is appropriate (apart from the normal stress anisotropy prediction) for this type of semi-bounded turbulence in the presence of a flat surface. Since the Reynolds number is low, it is valid to use this scheme above the 'shifted' origin $x_2 = x_{20}$, regardless of the surface roughness, so that the scale $l_2 = \kappa x_2, \kappa = 0.4$ (which confirms that l_2 is of the order of x_2) and the surface boundary condition for the turbulent region is $\bar{u}_1 = 0$ when $x_2 = x_{20}.$ The Karman–Prandtl solution to mean momentum (and scalar) transport equations when $x_2 > x_{20}$ is:

$$\bar{u}_1 = \frac{u_*}{\kappa}\left[\ln\left(x_2/x_{20}\right) + B\right] \tag{6-1}$$

for both smooth and rough walls, where $u_*^2 = -\sigma_{12}\left(\text{as } x_2 \to 0\right)$ and $B = 5.24$.

It is worth noting, however, that over a rough surface (roughness wall layer) at high Reynolds number, l_2 is shorter than in the former case since the mean velocity gradients vary rapidly in space, and the whole turbulent field is displaced upwards by a distance d (of the order of 1/30 of the height of roughness element) so that $l_2 = \kappa\left(x_2 - d\right)$ and $\bar{u}_1\big|_{x_2 = x_{20}+d} = 0.$ It is therefore valid to use this approach (i.e. mixing length model) above the false origin $x_2 = x_{20} + d.$ The Karman-Prandtl solution for rough wall is then given by:

$$\bar{u}_1\big|_{x_2-d>x_{20}} = \frac{u_*}{\kappa}\ln\left[\left(x_2-d\right)/x_{20}\right]. \qquad (6\text{-}2)$$

In fact, (6-1) and (6-2) are often used as a convenient near wall condition for the mean velocity in turbulence models, without either physical or empirical support [1] although it is demonstrated that only if the Reynolds number is much greater in comparison to the critical Reynolds number (i.e. $Re \gg Re_{crit}$) and the flow is changing slowly enough such that $\tilde{T}_L = T_L/T_D < 1,$ the mean profile $\bar{u}_1\left(x_2/x_{20}\right)$ in (6-1) and (6-2) near a solid surface has the same characteristic form for most turbulent flows (e.g. Schlichting, 1960). Indeed, the near wall profiles differ significantly from the high *Re* form (6-2), as the more complex models show, if the turbulence approaching the wall is changing rapidly, i.e. $\tilde{T}_L \geq 1,$ for instance in a separated flow region [89], or if the Reynolds number is low so that $Re \sim Re_{crit}$ near transition. Note that the Reynolds numbers for the constant pressure boundary layer considered in this study are much larger than Re_{crit} (i.e. $Re_{\delta^*} \geq 1000$).

Note that the $k-\varepsilon$ equations can also be applied so long as additional turbulence damping models are considered, for example the Launder–Sharma [90] version which is the most widely used for a range of practical turbulent as well as transitional flows [91].

Sink Flow

In this flow type, where the turbulence is almost homogeneous, the local (mixing length) models can be used to determine the statistics in space at a specific time $t = C$ (e.g. $\bar{u}\left(\boldsymbol{x}, C\right)$ and thence $\sigma_{ij}\left(\boldsymbol{x}, C\right)$ where C is a constant) in the kinematic studies; the length scale over which the turbulence is correlated is relatively small

(i.e. $\tilde{L}_X < 1$) and therefore, the eddy structure is a local function of mean velocity gradients, and is not affected by, for instance, the presence of the rigid surface.

However, the above-mentioned local models may not be used when the time variation of the statistics is of interest, since the turbulence then does not satisfy the conditions necessary for the validity of the model. This means that the changes of the mean velocity gradients or turbulence structure occur quite rapidly with distance along the mean streamlines such that the Lagrangian integral scale (or 'memory' timescale of` the turbulence) $\tilde{T}_L$ is relatively larger than the distortion timescale T_D (defined as $|\nabla \bar{\boldsymbol{u}}|/(\bar{\boldsymbol{u}}\partial_s(\nabla \bar{\boldsymbol{u}})) \sim |\sigma_{ij}|/|(\bar{\boldsymbol{u}}\partial_s \sigma_{ij})|$, and $T_D \sim |\sigma_{ij}|/|\partial_t \sigma_{ij}|$ in a steady and transient flow, respectively). Thus the normalised turbulent timescale is:

$$\tilde{T}_L = \frac{T_L}{T_D} = 1.92 > 1.$$

Either some complex models should be applied or physically based corrections to (2-1) can be introduced (i.e. involving a postdictive process) for these types of flow. The latter is sometimes computationally more convenient.

In such a flow zone, the expressions for the Reynolds stress σ_{ij} (or Reynolds flux $\sigma_{\theta i}$) in (2-1) and (2-2) may be wrong in magnitude and even in sign [36]; Savill, [92][9]. Neglecting the effects of turbulence on the apparent stresses can lead to a more accurate computation of $\bar{u}, p$ than by including an erroneous estimate of σ_{ij} based on (2-1), e.g. [93]); however, the effects of such errors on computations of the mean flow and mean temperature are small because in rapidly changing flows the magnitude of the momentum term $\|\partial_j \sigma_{ij}\|$ is much less in comparison with

[9] Both expressions are valid if the variations in turbulence structure (e.g. that which corresponds to the variations in mean strain rate in shear flow) in zones of flow occur relatively slowly over time.

the term $\left|\bar{\boldsymbol{u}}_{\boldsymbol{j}}\partial_j\bar{\boldsymbol{u}}_{\boldsymbol{i}}\right|$ [1], which is true in all model applications for incompressible flows[10].

The RSM modelling approach is also well suited to this flow since the turbulence is less local. Auxiliary algebraic expressions or evolution equations are required to solve the equations for the apparent stresses (i.e. Reynolds stress transport equations), in particular for estimating the two-point moments (e.g. the pressure-strain terms and dissipation) in terms of one-point moments (see [12]. See also §2.5 for further details of the ARSM closure model, for instance).

The pressure-strain term (i.e. $p_{ij}=\overline{u_i\partial_j p}$) is modelled by estimating p at point $\boldsymbol{x}$ in terms of the velocity field at other neighbouring points $\boldsymbol{x}'$;

$$p = p^{(nl)} + p^{(l)}, \tag{6-3}$$

where $p^{(l)}(\boldsymbol{x}) \sim C^{(l)}\overline{uu}\;\partial\bar{u}/\partial x(\boldsymbol{x}),$ (6-4)

$$p^{(nl)}(\boldsymbol{x}) \sim C^{(nl)}\overline{uu}\varepsilon k^{-1}(\boldsymbol{x}), \tag{6-5}$$

and $C^{(l)}$ and $C^{(nl)}$ are appropriate constants.

Note that $p^{(l)}$ and $p^{(nl)}$ denote the linear third order moments (which correspond to products of moments of the velocity field $\overline{uu}$ and mean velocity gradients $\partial\bar{u}/\partial x$) and non-linear second order moments (i.e. products of fluctuating velocity correlations, the turbulent kinetic energy k, as well as the energy dissipation rate ε), respectively, following [11]. They are usually termed (relatively) 'rapid' and 'slow', respectively, to demonstrate how they act on timescales. However, in most shear/straining flows the 'rapid' term continues to influence the flow as much as, and over the same period as, the 'slow' term.

[10] The change in the magnitude of the Reynolds flux can be of the order of the mean momentum flux in flows with density variations.

Thus, some authors, such as [1] prefer the nomenclature 'linear' and 'non-linear', respectively.

The coefficient $C^{(l)}$ in (6-4) is, in practice, obtained by considering idealised turbulence undergoing a constant deformation or strain rate, and is changed when turbulence is highly anisotropic or if the mean deformation rate $(\propto \partial\overline{u}/\partial x)$ varies over the timescale T_L along the mean streamlines, as happens in flows approaching bluff bodies or in trailing edge flows. In the case of trailing edge flows, however, the errors in the mean flow are not significantly affected by the errors in the turbulence [1]. A number of workers, e.g. [94], have shown that in shear flows $C^{(l)}$ is insensitive to the anisotropy of the eddies, but in straining or rotating flows it is not.

The errors may also be more significant near boundaries where the assumption of local homogeneity is much less valid, because the scale of the eddies L_X is generally comparable with the distance $x_2 \le \delta/5$ over which the mean velocity gradient $(\partial_2\overline{u}_1)$ is varying; in fact, in such cases $L_X \sim l_m = \kappa x_2$, where l_m is the mixing length scale and $\kappa = 0.4$ at very high Reynolds numbers where there is a whole spectrum of eddies [10]. These errors in the coefficients (i.e. both $C^{(l)}$ and $C^{(nl)}$) affect p and therefore turbulent stresses σ_{ij}. Such surface errors can be rectified by representing the blocking of eddies at the boundary. One approach is by using special wall correction functions for $C^{(l)}$ and $C^{(nl)}$ (proposed by [95], for example). Secondly, p_{ij} can be computed by means of auxiliary equations to model the way the pressure field is influenced by the wall blocking [96]. Alternatively, without the need to introduce the auxiliary equations, the highly distorted eddy motion can be described by making an interpolation between three-dimensional fluctuations and the restrictive form of two-dimensional fluctuations near the wall [36]. It has been found that when the mean gradient varies considerably and when there are large pressure fields near the boundary (e.g. where jets impinge onto obstacles, for example), the differences between these models are high [12].

Flat plate transitional boundary layer

There are large variations, especially in the mean velocity field $\bar{u}_i(\underline{x},t)$ and in the turbulence kinetic energy k in this flow (i.e. $\tilde{L}_X^{(\Sigma)} \sim \tilde{L}_X^{(k)} > 1$), as in many cases of important practical complex turbulent flows (e.g. the streamlines are highly curved, are diverging or have the presence of non-uniform body forces). Although this flow changes slowly in time such that the variances $\overline{u_i}^2$ and eddy length scales ($L_X^{(i)}$ for instance) change at a dynamically low rate along the mean streamlines over a distortion timescale T_D which is greater than the 'memory' timescale of the turbulence T_L (*i.e.* $\tilde{T}_L = T_L / T_D < 1$), the mean velocity $\partial_j \bar{u}_i$ has gradients on a length scale Λ across the streamlines that are dynamically significant. This means that Λ is less than the relevant turbulent length scale L_X, i.e. the normalised length scale:

$$\tilde{L}_X = L_X / \Lambda^{(\Sigma)} > 1 .$$

In this case, where the turbulence is not homogeneous, it has been found that EVM models would over-predict the effect of straining on the growth of kinetic energy k, e.g. [34].

RSM models are better, but still are over-sensitive to $\tilde{L}_X$ of the distorted turbulence. Note, however, that these sensitivities are insignificant in the case of the flat plate transitional boundary layer.

Shear layer impingement

In the shear layer impingement case, the mean velocity fields $\bar{u}_i$ have gradients on the inhomogeneity length scale Λ that are dynamically significant (such that $L_X > \Lambda^{(\Sigma)}$), and the mean strain is relatively high (i.e. $\tilde{S} > 0$) which increases the degree of inhomogeneity of the turbulence.

Several studies, e.g. [34], have demonstrated how EVM models can over-predict the effect of straining on the growth of k when $\tilde{L}_X^{(\Sigma)} = L_X / \Lambda^{(\Sigma)} > 1$; though this sensitivity is not very large in the case of shear layer impingement since the mean strain is insignificantly small, i.e. $\tilde{S} = 0.04 \ll 1$.

RSM models are better, since the individual transport equations for Reynolds-stress include the pressure-strain 'redistribution' term p_{ij} which is modelled as $\left(p^{(l)} + p^{(nl)} \right)$ (where $P^{(l)}$ and $P^{(nl)}$ are linear or 'rapid' term, and non-linear or 'slow' term, respectively), and indicate the significant role of non-local pressure fluctuations in a distorted turbulent flow (e.g. [12]). This level of closure models, however, is still over-sensitive to $\tilde{L}_X$ of the distorted turbulence [1].

A number of modifications to one-point turbulence models have been proposed to handle such problems, including eddy viscosity closure models where the turbulence viscosity ν_e depends non-linearly on the strain rate (e.g. [61]) as briefly mentioned in §2.5. For this type of distorted and inhomogeneous turbulent flow, upstream boundary conditions need to be introduced even if only single-point statistics are required, since the upstream or initial anisotropy and spectra form have considerable effects on the changes in the variances $\overline{u_i u_i}$ of all the components and in the length scales and dissipation rate [12]. These sensitivities are greatest when the mean strain is closer to pure strain, such that $\tilde{S} \sim 1$.

Channel flow

In the non-homogeneous channel flow (outside viscous sublayer zone), the assumption of spatial localness of the turbulence is not strictly valid, and since the one-point models are worse in the outer part than near the wall, a rectification of this deficiency is necessary, where specific models for the

turbulence viscosity ν_e itself have been suggested for the outer region (e.g. the Spalart-Allmaras model mentioned in §2.2.2).

The simplest transport models, such as the widely used $k-\varepsilon$ two-equation eddy viscosity model for example, are valid in this type of flow, since they assume that turbulence is changing slowly enough and homogeneously enough at low Reynolds number such that;

$$\sigma_{ij} = -\nu_e\left(\partial_j\overline{u}_i + \partial_i\overline{u}_j\right), \nu_e = C_\nu k^{1/2} L_X ,$$
$$F_{\theta i} = -\kappa_e \partial_i \Theta , \ \kappa_e = C_\kappa k^{1/2} L_X ,$$
$$\text{where } C_\nu , C_\kappa \sim 1.$$

The ratio of these coefficients depends on the eddy structure, and varies only slightly in any turbulent flow type. (see e.g. [30] and [12] for the construction of more complex tensor models for a ν_{ei} and κ_{ei}). It is worth noting that it is not necessary for k to be the actual turbulence kinetic energy so as to compute ν_e and κ_e, but rather some portion of this (e.g. $\overline{u_2^2}$) corresponding to large eddy motions dominating the process of transport.

Sheared homogeneous turbulent flow

Prediction methods proposed in sheared homogeneous turbulent flow are not much different from those in sink flow (both types of turbulence are less local in time, i.e. $\tilde{T}_L \sim 1$), where the mixing length model (with physically based correction) and ARSM model are valid, as has been discussed in. However, due to the fact that the former is extremely local spatially (i.e. $\tilde{L}_X = 0.002 \ll 1$ which strongly suggests the homogeneity of the turbulence field), the EVM models can estimate well the effect of straining on the growth of k (e.g. [34]).

Free shear flow

Both the normalised integral timescale $\tilde{T}_L$ and the straining parameter $\tilde{S}$ are large in contrast to those in all the previous cases. The dynamics of turbulence are relatively non local, especially in time (i.e. the turbulence is not in equilibrium, such that $\tilde{T}_L = 3.4 > 1$). Furthermore, since there is a zone of mean strain which is not purely shear in this flow (where the turbulence is undergoing a constant rate of deformation or strain, i.e. $\tilde{S} = 0.24 > 1/10$ which contributes to the inhomogeneity of the turbulence), the turbulence is not entirely determined by the local velocity gradient. Thus, the use of the $k-\varepsilon$ model is not well adapted for this non-local flow.

Other alternatives involve the use of non-local EVM or RSM models with temporal as well as spatial development in order to obtain approximately correct predictions.

Interestingly, in a group of turbulent jets, i.e. a round jet in co-flow [88] and a jet in free stream [76], the local (mixing length) model, in particular solutions (6-1) and (6-2) are valid above or below horizontal fluid interfaces (e.g. [97], where the horizontal velocity fluctuations u_{i} are not necessarily zero (in reference to the interface).

It is expected that there are low and high 'streaks' forms of the turbulence structure in the free shear flow considered in this study, which are the result of a combination of shear and rotation (which systematically strengthens the straining field), e.g. [80]. Also, the form of local straining is very significant; the turbulence structure is very sensitive to the form, and is even more sensitive to the shearing than to the swirling effects. Even if the magnitude of the rate of strain is of the order of $1/10$ (i.e. $\left|\tilde{S}\right| \sim 1/10$), the structure of the eddy is changed from its form in pure shear where $\tilde{S} = 0$ ([41]; [62]; [98]).

Since the mean shear is non-uniform, the formula for the finite length, $L_x \sim u_o/S$ is valid [16] (otherwise, if it is uniform and constant in time, as in certain laboratory and numerical works, the length scale grows, i.e. the eddies are stretched, with time without limit and thus, such equation is no longer valid, e.g. [99]). This suggests that the direct simulation mentioned in §3.6 of Chapter 3 (where the mean shear is non-uniform such that $\overline{u}_1'' \neq 0$) is a suitable 'test case' for the use of turbulence models in flows of practical importance. Note that the overall straining field can be constant in space and time even if $\overline{u}_1'' \neq 0$.

It is clear that the guideline 'modelling' map (i.e. Figure 6-1) can, in principle, be overlaid on a newly quantified version of Figure 4-1 (i.e. Figure 6-2) in order to ascertain which flows different models should be appropriate for.

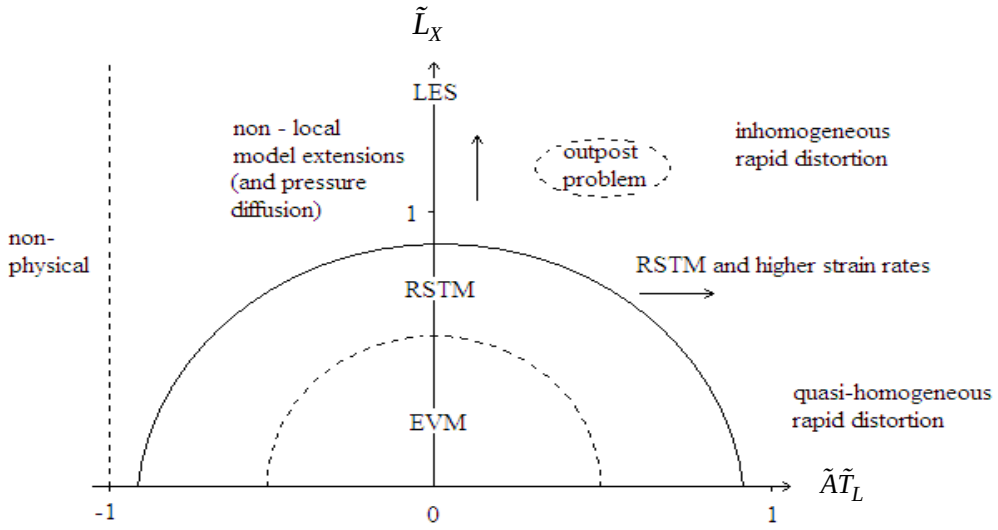

Figure 6-1 Guideline 'modelling' map based on the spatial and temporal localness parameters $\tilde{L}_X$, $\tilde{T}_L$ reproduced from [1].The solid line is the 'frontier' of standard RSM, while that made up of dashes indicates a typical 'outpost' type of flow where flow specific modelling has been developed. Note that the numbers on both axes represent only qualitative estimates.

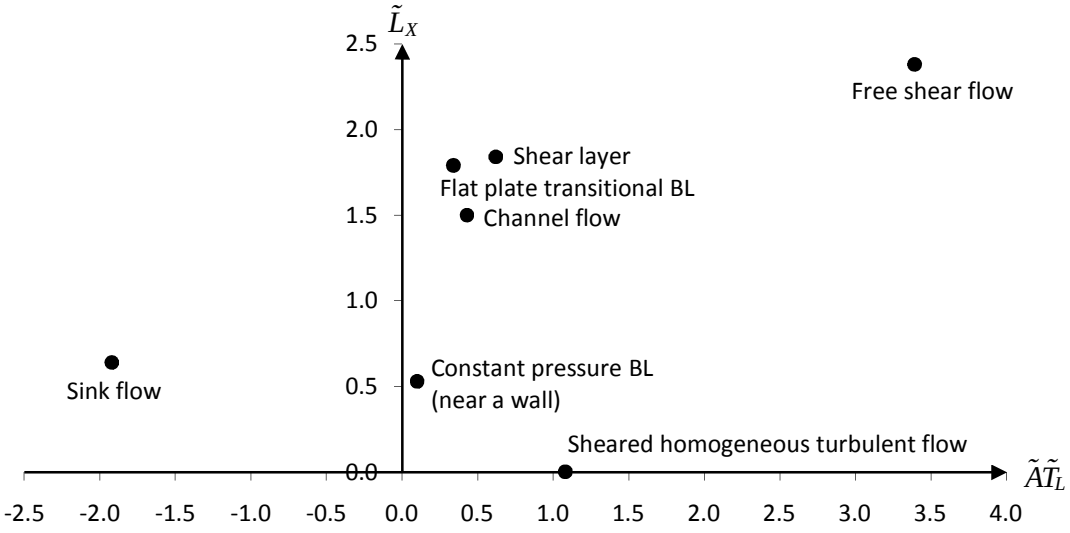

Figure 6-2 The quantitative localness map. Note that $\tilde{A}$ is the sign of the advective term in the energy equation.

7

Models for application challenges[11]

A general framework consideration of the underlying flow regimes (UFRs) is needed to model the application challenges (ACs), i.e. to put the ACs on the map for appropriate prediction methods. The localness in turbulence, both in space and in time, determines the distribution of the UFRs, and hence the ACs on the 'localness' map in several ways (see Figure 7-1 for an example of such distribution), and therefore confirms the validity of given closure models. Whether or not a turbulent flow is local or non-local depends on whether both the fraction of the scale over which the kinetic energy or mean velocity gradient varies $\tilde{L}_x$, and the ratio of the integral timescale to that of distortion $\tilde{T}_L$, are less than 1 (i.e. $\tilde{L}_x < 1, \tilde{T}_L < 1$), or of the order 1 or greater $\left(\text{i.e. } \tilde{L}_x \gtrsim 1, \tilde{T}_L \gtrsim 1\right)$, respectively (see [1]). There are also cases where the turbulence is local in either space or time only, when $\tilde{L}_x \gtrsim 1, \tilde{T}_L < 1$, for instance. Note that the 'local' flows and those which are 'non-local' in space and time will simply be referred to as 'local' and 'non-local', respectively.

Another important parameter to consider here is the strain parameter $\tilde{S}$ which not only represents the dominant type of strain in turbulence cases but also gives information about the presence of external influences on the turbulence structure. This means that the choice of local/non-local turbulence models can be made on the basis of three parameters, i.e. $\tilde{L}_X$, $\tilde{T}_L$, and $\tilde{S}$.

[11] An introduction to the work in this chapter (along with the preliminary results) were presented in [100].

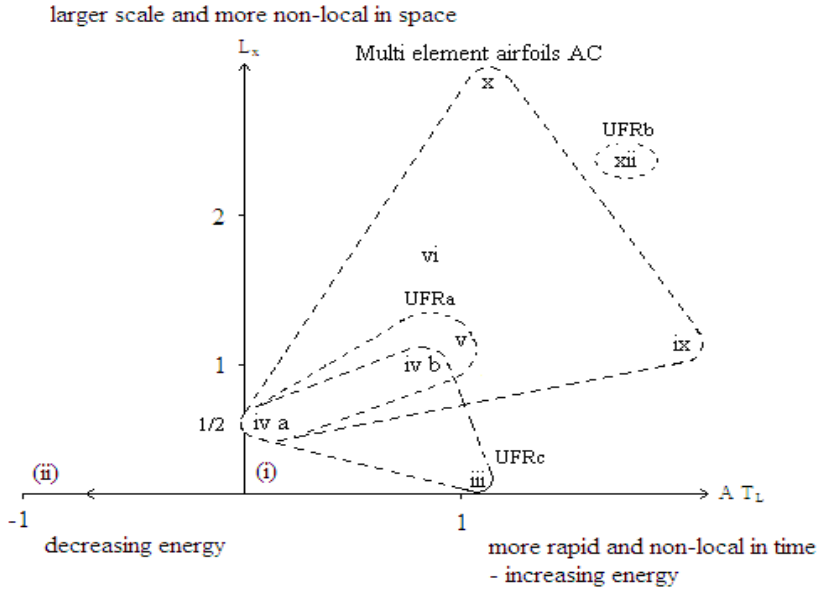

Figure 7-1 Map for the localness of turbulence processes reproduced with simplification and additional information from [1]. The Roman numerals on the graph refer to a few particular types described in table 3.2, section 3.4.7. One case of AC (that of multi element airfoils) and three examples of UFRs are shown:
UFRa – Boundary layers under various pressure gradients, including severe adverse pressure gradient causing separation.
UFRb – Flow over surface mounted cube/rectangular obstacles.
UFRc – Flow in pipes with sudden contraction.

Both the ACs and UFRs of interest, as shown in Table 2-3, have been discussed in §2.8.5. The selection is mainly based on the main types of flow listed by [1] whose 'localness' map serves as a qualitative guideline to tackle practical engineering as well as environmental problems. This map initiates further classification of the ACs and UFRs under consideration that have been diagrammatically plotted (see Figure 7-2 and Table 7-1) in order to investigate the necessity of zonal-modelling (see for example [55], and [56]) in complex flow predictions.

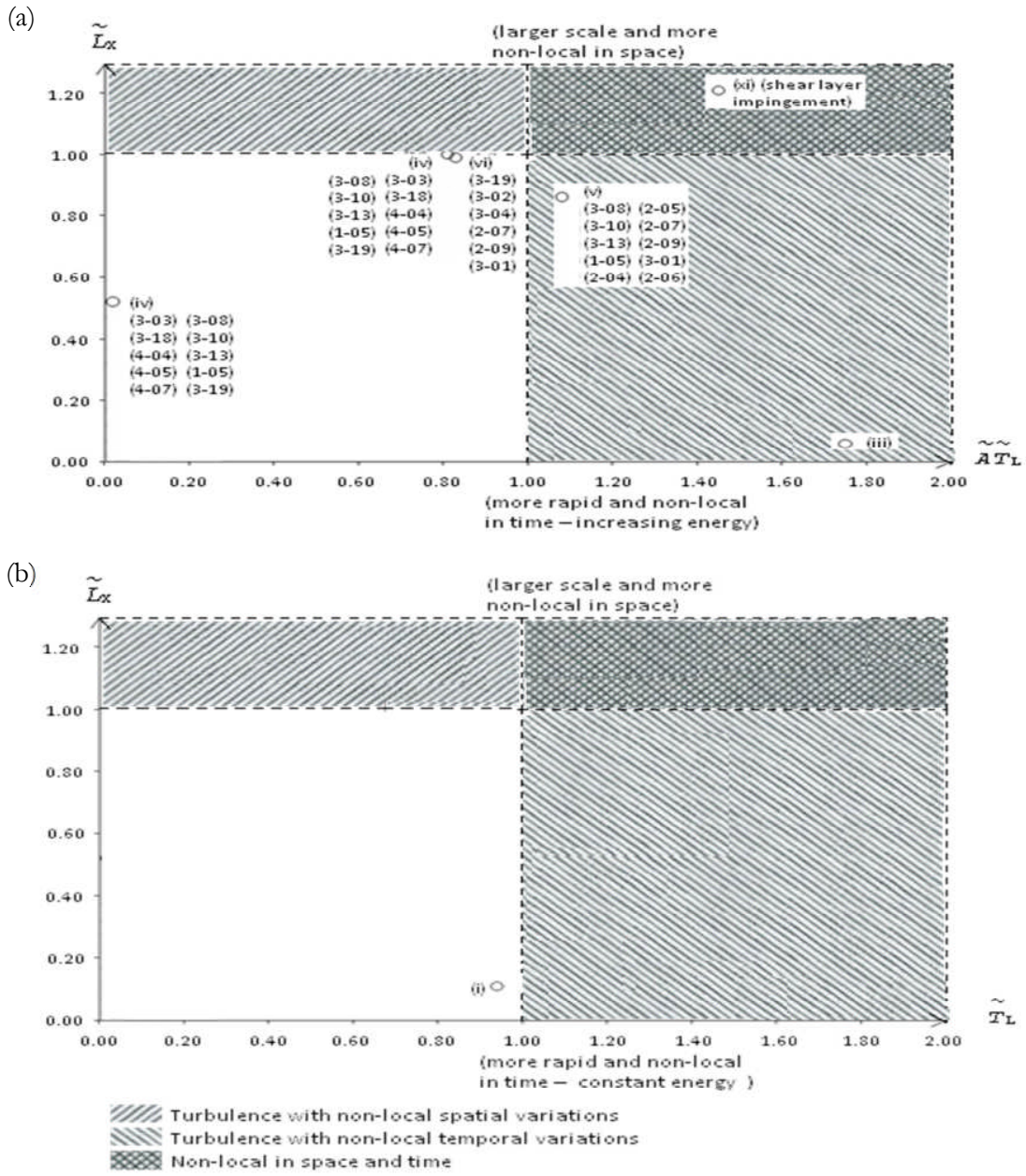

Figure 7-2 Maps for the localness of turbulence process. *(a) 'Localness' map for UFRs which address seven (out of thirteen) types of turbulent flow in* [1]. *(b) Map for turbulent flow with constant energy input.* The number in brackets indicates ACs – UFRs of interest. The Roman numerals on each graph refer to main types of flow. Note that $\tilde{A}$ is the sign of the advective term in the kinetic energy equation (that is either '+' or '-'), and that (i) is the only flow in which the energy input is constant where the product $\tilde{A}\tilde{T}_L$ is undefined, as shown in (b).

	Types of turbulent flow	UFRs
(i)	Homogeneous stationary turbulence	
(ii)	Homogeneous decaying turbulence	
(iii)	Strained turbulence	4-13
(iv)	Turbulent boundary layer	
	(near a wall)	1-02, 3-02,3-03,3-06,3-07,3-08,3-10,3-13,3-18,3-19,4-04,4-05,4-07
	(near outer boundary)	1-02,3-02,3-03,3-06,3-07,3-08,3-10,3-13,3-18,3-19,4-04,4-05,4-07
(v)	Free shear flows and separated flows	1-01,1-04,1-05,2-02,2-03,2-04,2-05,2-06,2-07,2-09,3-01,3-08,3-10,3-13,4-11,4-12
(vi)	Large scale free stream turbulence interacting with a boundary layer	2-07,2-09,3-01,3-02,3-04,3-19
(vii)	Turbulence near a free surface	
(viii)	Natural convection (no mean flow)	3-06,3-07,4-09, 4-10
(ix)	Shock boundary layer interaction	3-05,3-16
(x)	Trailing edge boundary layer-wake interactions	2-01
(xi)	Jet impaction	3-09
(xii)	Turbulent flow over small obstacles	3-14,
(xiii)	Swirling shear flows	4-02,4-03,4-06,4-11,4-12

Table 7-1 Classification of UFRs based on the main types of flow.
Note that this table is complementary to Figure 7-2.

Note that all ACs are generally covered in this work. The UFRs are classified on the basis of their primary contributions to the ACs, and of their associations with the main flow types of [1] (i.e. those which are represented by the combinations of all four qualitative statistical parameters $\widetilde{L}_x, \widetilde{T}_L, \tilde{S}$, and $\tilde{G}$).

The approach used in this classification reveals whether one standard prediction method (e.g. local models alone) could produce accurate results for an AC (e.g. AC-*External Aerodynamics*), and hence eliminate the need for zonal modelling (ZM) or not. Only if both types of model (i.e. local and non-local) are used in predictions, is ZM said to be necessary.

The application of ZM is crucial when a UFR or AC is divided into different flows/zones with different localness parameter ranges. However, since the localness in space and time are independent of each other, this application may not be necessary when the required statistics are affected by only one of the localness parameters (i.e. $\widetilde{L}_x$ and $\widetilde{T}_L$), and such parameter values lie in the same range for all flows.

7.1 Classification of UFRs - ACs

In order to see whether or not ZM is appropriate for an AC, it is worth looking first at Table 2-2 to further classify the main types of flow based on the 'localness' parameters. Flows (iv) (near outer boundary), (v) (vi), and (ix)-(xiii) are non-local. Others are local either in space or time; flows (i), (ii), and (iii) are spatially local, while (iv) (near a wall), (vii), and (viii) are local in time. Secondly, the structural parameter, in particular the strain parameter $\tilde{S}$, is considered in order to define the main flows on the basis of the external influences on turbulence structure. Whether the 'amount' of the influences is large or not depends on whether the magnitude of $\tilde{S}$ is less than 1 (i.e. $|\tilde{S}|<1$), or of order 1 or greater (i.e. $|\tilde{S}| \gtrsim 1$), respectively. Then, by rearranging these flows, one has Table 7-2.

It is important here to note that the 'stationarity' of flow (i) is due to the constant energy input that is neither increasing nor decreasing (i.e. where it was considered that $\tilde{A} = 0$ instead of +1 or -1) in order to maintain the eddies against distortion, such that $\tilde{T}_L \sim 1$ (see [1]). Clearly, such homogeneous

Types of turbulent flow	
(i) Homogeneous stationary turbulence	
(ii) Homogeneous decaying turbulence	
(iii) Strained turbulence	
(iv) Turbulent boundary layer (near a wall)	
(vii) Turbulence near a free surface	
(viii) Natural convection (no mean flow)	
(iv) Turbulent boundary layer (near outer boundary)	
(v) Free shear flows and separated flows	
(vi) Large scale free stream turbulence interacting with a boundary layer	
(ix) Shock boundary layer interaction	
(x) Trailing edge boundary layer-wake Interactions	
(xi) Jet impaction	
(xii) Turbulent flow over small obstacles	
(xiii) Swirling shear flows	

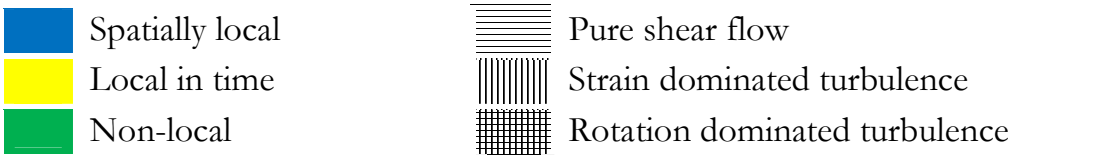

Table 7-2 Rearrangement of main types of turbulent flow based on their 'localness' and strain characteristics

stationary turbulence is roughly temporally non-local, despite the fact that $\tilde{A}\tilde{T}_L = 0$, and the product $\tilde{A}\tilde{T}_L$ may cause the loss of information (i.e. the degree of non-equilibrium $\tilde{T}_L$) when the energy input is constant. The problem arises since $\tilde{A}$ is defined by the sign of the advective term (that is either '+' or '-' for increasing or decreasing energy input, respectively) in the kinetic energy equation (see [1]). The sign is unilaterally dependent on the term. If the term is zero (as in the case of homogeneous turbulent flow, for instance), then it could take any sign, and it would be impossible to determine the input energy profile by means of the term. Thus it is proposed in this study that when the energy input is constant, $\tilde{A}$ and consequently $\tilde{A}\tilde{T}_L$ are undefined.

By referring to Figure 7-2 and Table 7-2 as initial guidelines, all the UFRs of interest can now be classified by localness and strain characteristics. Most of the time, each single flow belongs to either one type of localness or another. (see Table 7-3).

Although our aim is to understand whether there is a necessity for the development of ZM in an AC rather than a UFR, the following classification of UFRs (which is also tabulated in Table 7-3) is useful since it determines the distribution of the ACs on the 'localness' map, and hence, on that for turbulence models;

UFRs (1-01), (1-04), (1-05), (2-01), (2-02),
(2-03), (2-04), (2-05), (2-06), (2-07),
(2-09), (3-01), (3-02), (3-03), (3-04),
(3-05), (3-06), (3-07), (3-08), (3-09),
(3-10), (3-13), (3-14), (3-16), (3-18),
(3-19), (4-02), (4-03), (4-04), (4-05),
(4-06), (4-07), (4-11), and (4-12).

These flows are of the same type (i.e. non-local), where a non-local model is better for prediction.

UFRs (1-02), (3-02), (3-03), (3-06), (3-07),
(3-08), (3-10), (3-13), (3-18), (3-19),
(4-04), (4-05), (4-07), (4-09), (4-10),
and (4-13).

The wall presence may or may not determine the localness (in space-time) of the flow regions in these flows. Note that (4-13) is the only case where the turbulence is spatially local, where local models are better for prediction.

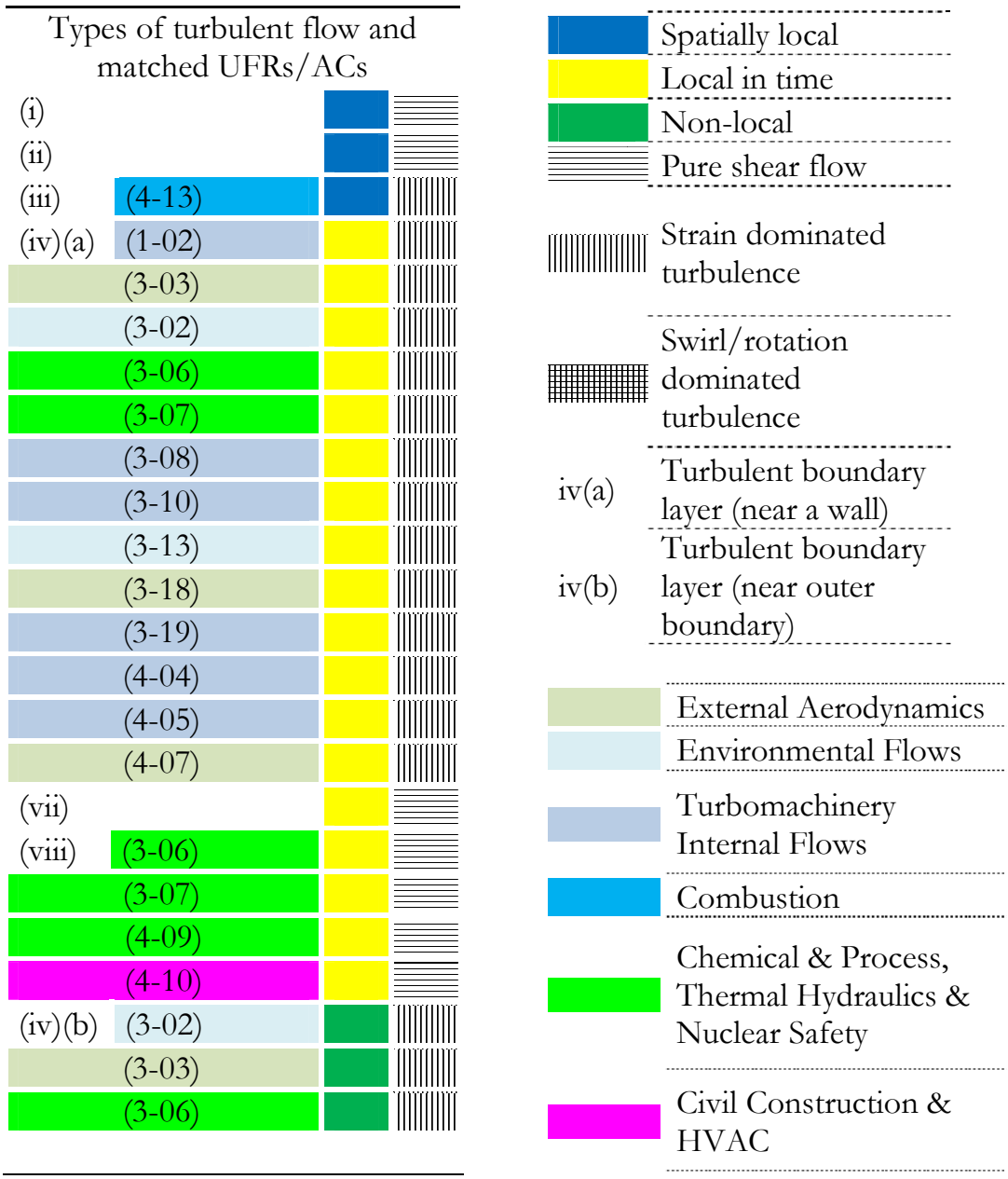

Table 7-3 Classification of matched UFRs/ACs based on the localness-straining characteristics

Types of turbulent flow and matched UFRs/ACs	
(iv)(b)	(3-07)
	(3-08)
	(3-10)
	(3-13)
	(3-18)
	(3-19)
	(4-04)
	(4-05)
	(4-07)
(v)	(1-01)
	(1-04)
	(1-05)
	(2-02)
	(2-03)
	(2-04)
	(2-05)
	(2-06)
	(2-07)
	(2-09)
	(3-01)
	(3-08)
	(3-10)
	(3-13)

Types of turbulent flow and matched UFRs/ACs	
	(4-11)
	(4-12)
(vi)	(2-07)
	(2-09)
	(3-01)
	(3-04)
	(3-19)
(ix)	(3-05)
	(3-16)
(x)	(2-01)
(xi)	(3-09)
(xii)	(3-14)
(xiii)	(4-02)
	(4-03)
	(4-06)
	(4-11)
	(4-12)

Table 7-3 *(continued)*

Remarks

In some cases, ZM could be relaxed, either when the flow regions of interest are not affected by the presence of rigid surfaces or fluid interfaces, or the calculations cover the whole flow field right up to the solid boundary or interface, for instance. The latter needs including, in a model for fully developed turbulence, a representation of fluctuating motions near the boundary that are not fully turbulent. For instance differential closure equations such as $k-\varepsilon$ are applied very near the wall and boundary conditions are assumed as $x_2 \to 0$ for $\bar{u}(x_2), k(x_2), \varepsilon(x_2)$ and their derivatives.

The solutions of these models yield the 'structural' wall profiles for $\bar{u}, k, \varepsilon$ in a thin layer (i.e. at $0 \le x_2 \le x_{2w}$, where x_{2w} is the wall level for defining the thickness of a non-conforming wall layer). This approach is soundly based on the assumption that the profiles of k, ε very close to the wall are effectively understood and can be defined in any given flow situation (see for example Section 2 in [1] for further details).

7.2 Maps of turbulence models for ACs

Since each flow type in a UFR belongs to a particular AC, the distribution of ACs on the 'localness' map is very much determined by Table 7-3. Consequently, the role of the straining needs also to be taken into account in order to investigate more deeply the appropriateness of the ZM. When the strain parameter is relatively large, such that $|\tilde{S}| > 0$, then the eddy structure and the turbulence energy are quite sensitive to the upwind conditions and the flow history [80]. This indicates that $\tilde{S}$ contains some information about external influences which contribute to the non-localness of the turbulence. In such a case (as far as $\tilde{S}$ is concerned), the use of non-local models is better to handle the effects of these influences. If $\tilde{S} \approx 0$ (as happens in the constant pressure boundary layer and channel flow cases discussed in §5.5), then the

necessity for non-local models can be justified on the basis of 'localness' parameters (i.e. $\tilde{L}_x$ and $\tilde{T}_L$) alone.

Table 7-4 shows how certain combination of the 'localness'-strain parameters could lead to the need for ZM, or not. This 'localness'-strain based approach relies upon the statistics that are affected by the related statistical parameters.

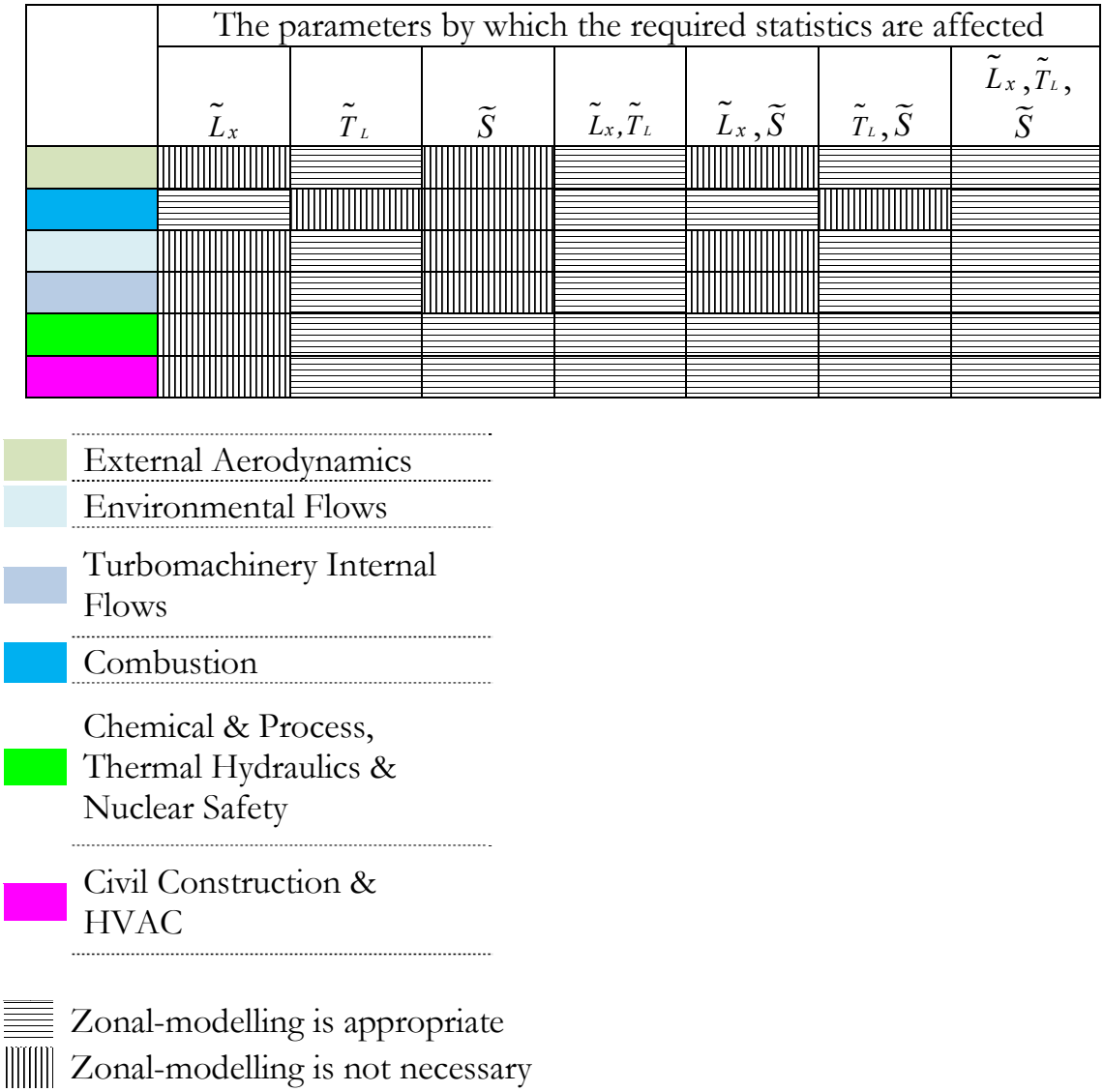

Table 7-4 Appropriateness of zonal-modelling for predictions in ACs. The need for zonal-modelling varies in all ACs, depending on the parameters by which the required statistics are affected.

Consider AC-*Combustion*. In order to compute, for instance, the kinetic energy k and rate of dissipation ε which are affected by the normalised length scale $\widetilde{L}_x$ (where $\widetilde{L}_X \alpha k^{3/2}/\varepsilon$), both local and non-local turbulence models need to be used, since, by taking the whole UFRs which contribute to AC-*Combustion* (as given in Table 7-3) into account, it is not generally possible to make accurate predictions at local closure model (e.g. Prandtl mixing length) levels alone. Less local models (e.g. $k-\varepsilon$) may be sufficient, but they are relatively more complex than the former, because the evolution equations are involved at this level of closure to account for the history effects. Thus, it is more practical to treat both types of turbulence (i.e. local and non-local) separately, which means that ZM is appropriate in this case. However, other ACs, as far as column '$\widetilde{L}_x$' is concerned, do not involve ZM, where the use of local models is invalid.

When the production of turbulent kinetic energy $\mathcal{P}$ is to be obtained, for example, then the normalised time scale $\widetilde{T}_L$ plays a considerable role. While the implementation of non-local models is inevitable for each UFR in AC-*Combustion*, ZM is appropriate for the rest of the ACs. This argument is similar to that used in the case involving column '$\tilde{T}_L,\tilde{S}$', which deals particularly with quantities such as ε and mean strain rate $\partial_j \bar{u}$.

Column '$\widetilde{S}$' separates AC-*Chemical and Process, Thermal Hydraulics and Nuclear Safety* and AC-*Civil Construction and HVAC* cases (which require ZM) from the rest. In the latter cases, the strain parameter $\left|\widetilde{S}\right|>0$ suggests that the eddy structure and the turbulence energy depend on external influences.

While column '$\widetilde{L}_X,\widetilde{S}$' suggests that ZM is not necessary for half of the ACs (those in *External aerodynamics, Environmental flows*, and *Turbomachinery internal flows*), for the rest of the columns (i.e. those of '$\widetilde{L}_x,\widetilde{T}_L$' and '$\widetilde{L}_x,\widetilde{T}_L,\widetilde{S}$') the requirement for ZM may not be relaxed. Figure 7-3 to Figure 7-8 (which are meant for AC-*External Aerodynamics* alone) provide instances of how an AC can be modelled by referring to Table 7-3 and Table 7-4. These figures are those of 1-D and 2-D. Their uses depend on whether the statistics of interest are affected by any combination of the statistical parameters.

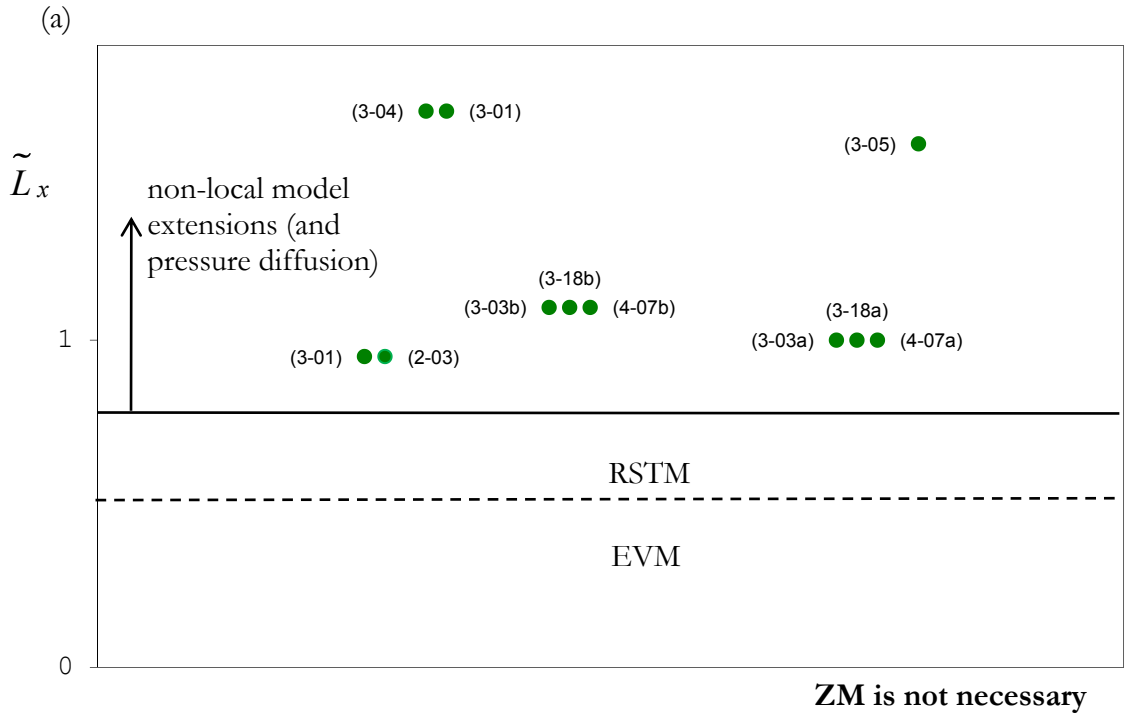

Figure 7-3 1-D normalised length scale $\tilde{L}_X$ based modelling map

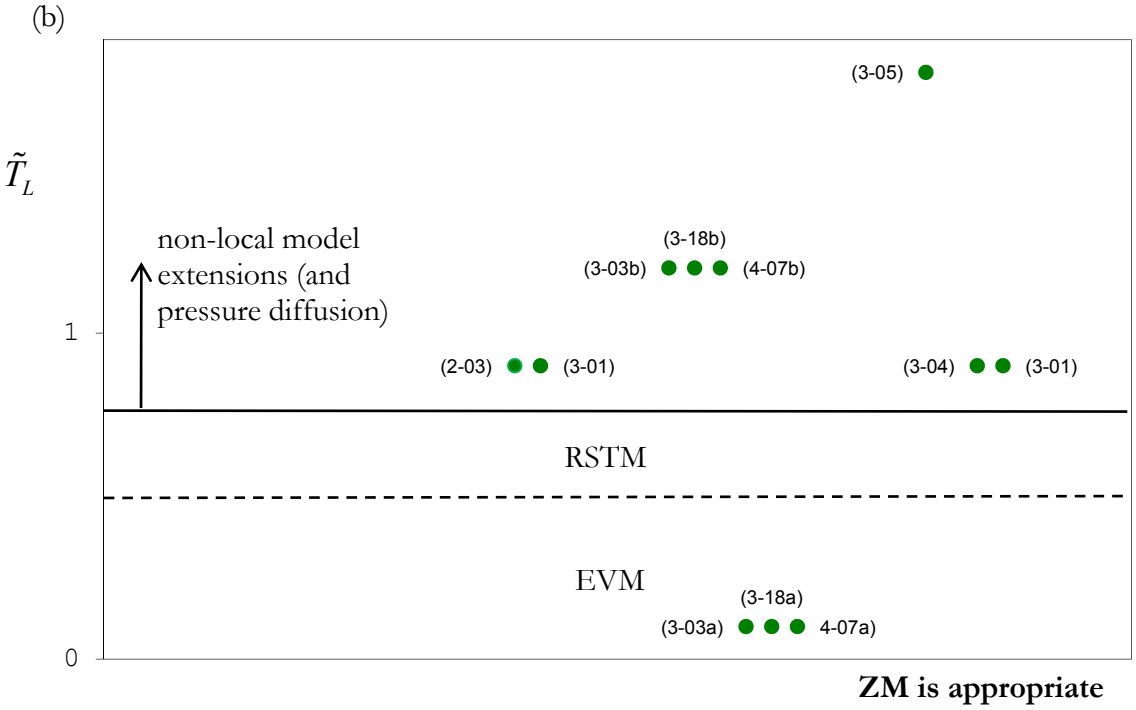

Figure 7-4 1-D normalised time scale $\tilde{T}_L$ based modelling map

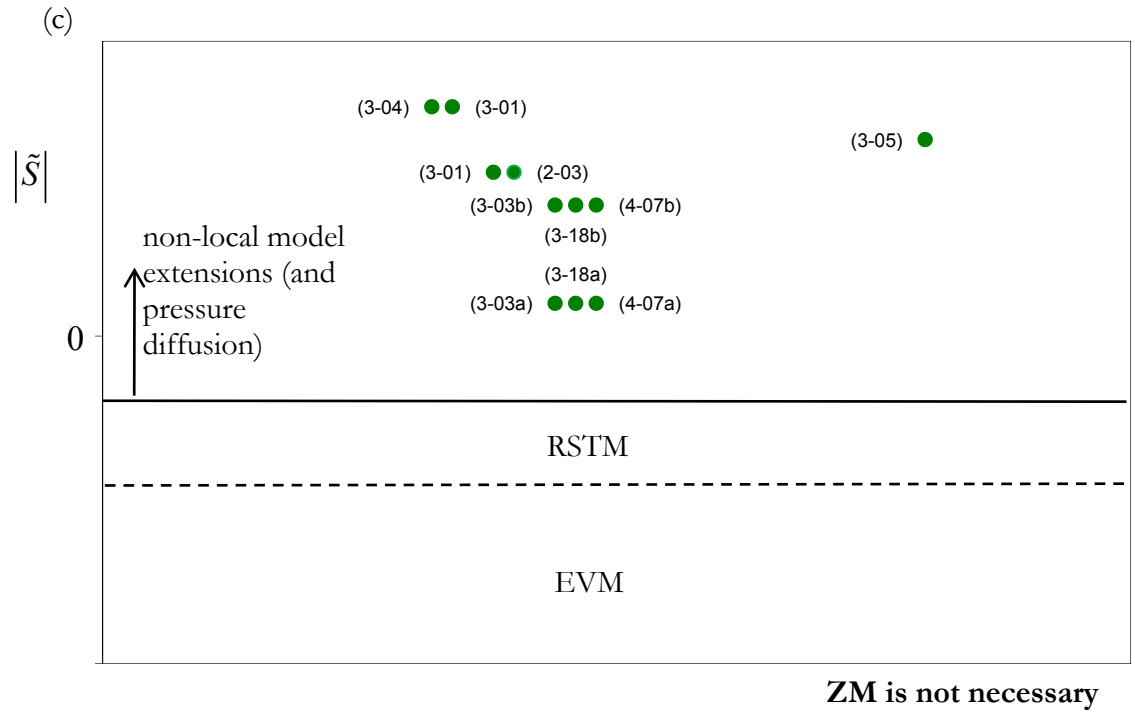

Figure 7-5 1-D strain parameter $\tilde{S}$ based modelling map

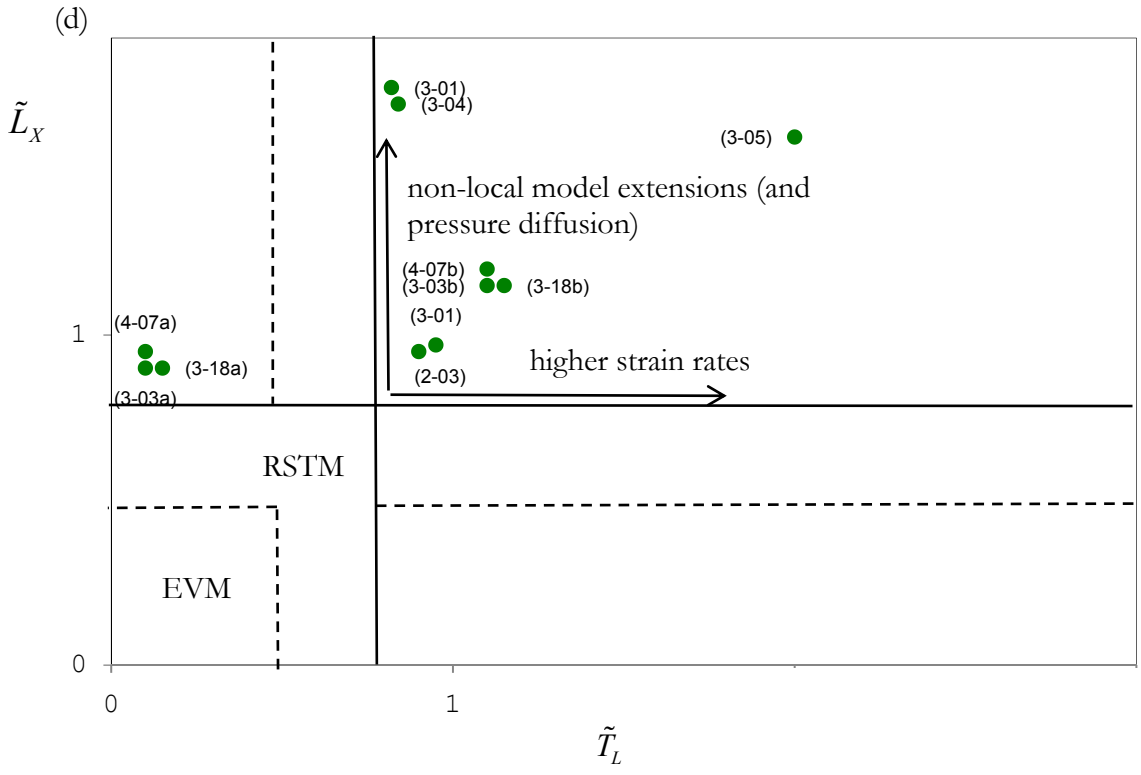

Figure 7-6 2-D $\tilde{L}_X - \tilde{T}_L$ based modelling map

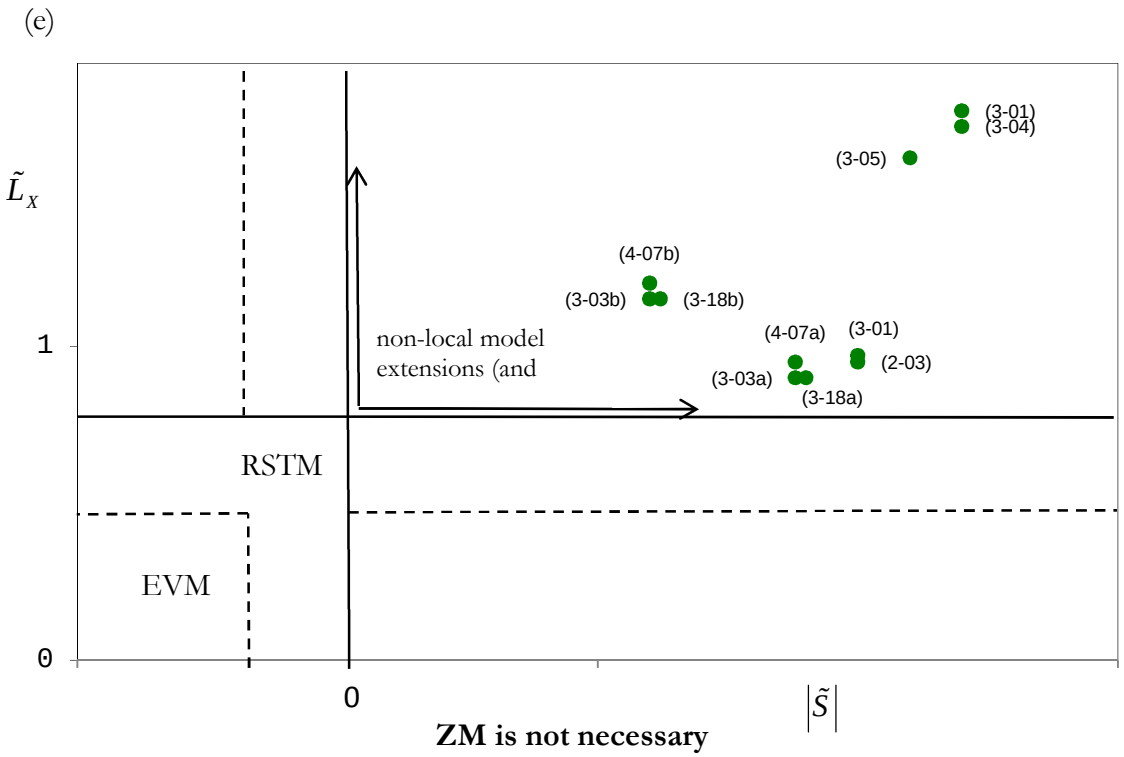

Figure 7-7 2-D $\tilde{L}_X - \tilde{S}$ based modelling map

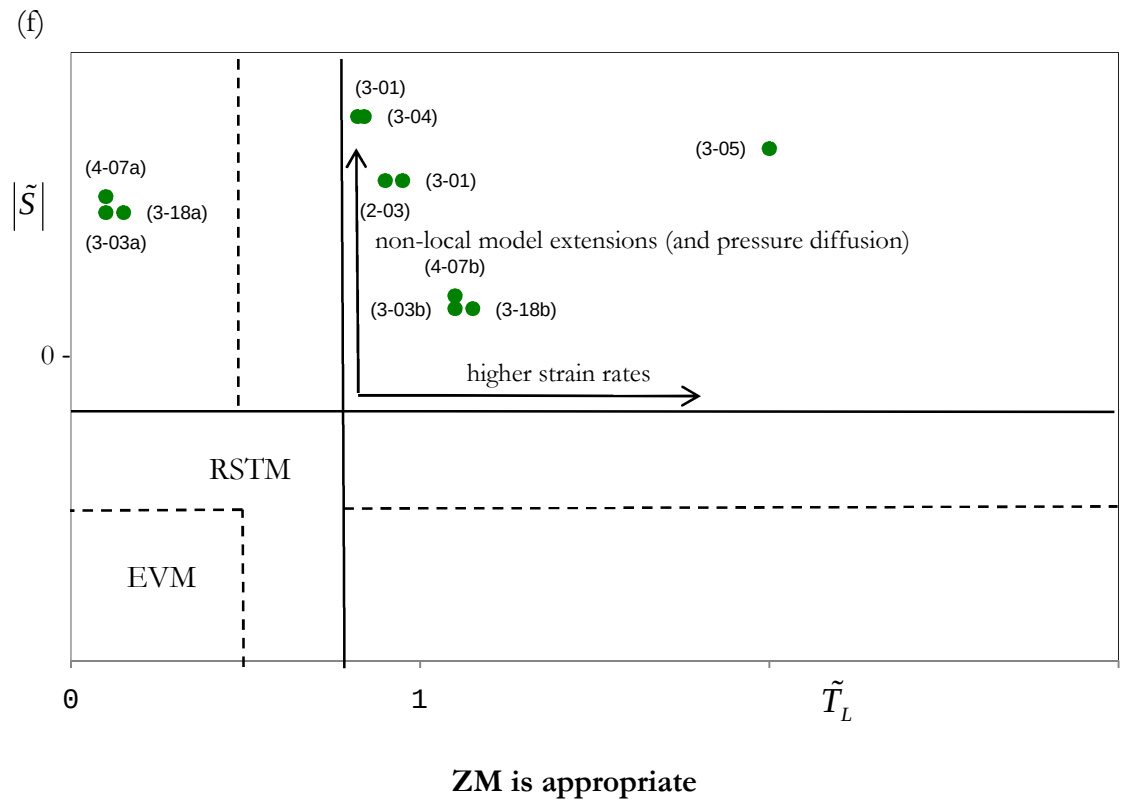

Figure 7-8 2-D $\tilde{S} - \tilde{T}_L$ based modelling map

The suggested scheme that has been described in this chapter can be summarised as follows:

1. Rearrange main flow types of turbulent flow on the basis of their 'localness' and strain parameters.

2. Identify UFRs of interest and classify them based on the main types of flow.

3. Match each class of UFR with an AC/s.

4. Classify matched UFRs-ACs using the localness-straining characteristics by which the required statistics are affected.

5. Determine whether or not the UFRs can be grouped on the modelling maps for ACs to form the basis of decisions in assessing the need for the localness based zonal-modelling.

Note that models for ACs which have been proposed in this thesis are those involving three statistical parameters (i.e. two 'localness' parameters and a structural parameter). Although these parameters are sufficient as the basis for the choice of the models in the case of fully developed turbulence, it is unquestionable that the effects of the Gaussian or non-Gaussian structure of the large scale turbulence can also suggest the localness or non-localness of the turbulence. If such structure away from a region (e.g. near a fluid interface) affects the structure at that region, then it is whole patterns of large scale eddy transports, and not local gradients, that determine the fluxes of heat and momentum, which is why for even qualitatively correct results, the RSTM method is the simplest level of method [95]. Otherwise, local gradients are sufficient to determine such fluxes.

8
Conclusions and consideration of future work

8.1 Conclusions

Refinement of all 'localness'-structural parameters is indeed possible, and is of practical importance for turbulence prediction in both industrial and environmental areas since the parameters represent the particular statistical properties of a turbulent flow of interest. Although the apparent (generic) type of the flow is recognised, its varieties based on basic physical mechanisms are wide enough, and need to be taken into account so as to make a good choice of turbulence prediction methods (i.e. turbulence models).

It is obvious that in each case of main flow type, a subtype of flow could slightly differ from another such that the combinations of the parameter values are also different. Nevertheless, since their 'localness'-structural classifications are based on the mathematical-empirical estimate [1], such values are within the same range. Thus, the parameter quantification links clearly a given flow to its main type which dominates it.

Even though in some cases the set of the parameters does not fully 'imitate' the previous estimate [1], this can be appreciated by considering the origins of the datasets analysed in this work. Turbulent flows of practical importance reproduced in numerical studies and the laboratory are sometimes subject to simplifications. This means that the reproduced flows are, at most, close to those that occur in real situations (i.e. that are much more complex).

The classifications of these flows of interest show that, given the various cases of turbulence, it is indeed possible to group them based on the mathematical-empirical estimate, and secondly, to choose the relevant turbulence models appropriately. Note that the groups do not necessarily refer to the main types of turbulence; they might be directly linked to a partial or full set of the statistical parameters.

Having linked the complex flows to their corresponding statistical parameters, the concept of localness based zonal-modelling proves to be both necessary and sufficient (as guidelines) for many cases involving the application challenges (ACs). Although the necessity for such a concept (of zonal-modelling) varies depending on the criteria of the 'mixture' of the underlying flow regimes (UFRs) in each AC, and on the quantified values of the parameters, this study shows that a prototype for the grouping approach is beneficial and can be referred to to during the assessment.

Discussions in Chapter 6 on the *quantified parameters-prediction methods* relationship provide an instance of how to choose the appropriate turbulence models for a single and/or group of flows (e.g. AC-*external aerodynamics* turbulent flows) for whose parameters quantitative values are known. However, since the distribution of the UFRs, and thence ACs on the 'localness'-structural map are purely based on the mathematical-empirical estimate [1], the guidelines for turbulent predictions given in [1] complete this classification. Hence, the quantitative estimates serve as a guideline for the grouping of the UFRs contributing to the key industrial-environmental ACs (six of them as demonstrated by ERCOFTAC), which is useful in order to assess the need for the localness based zonal-modelling.

It is found that the need for zonal-modelling is characterised by both the required statistics (e.g. the mean velocity and the Reynolds stress) as well as the 'localness'-straining parameters which affect these statistics. There seem to be non-linear interplays between the straining parameter $\tilde{S}$ and the 'localness' parameters, i.e. $\tilde{L}_X$ and $\tilde{T}_L$, since $\tilde{S}$ has a relationship with the localness of

the turbulence (see Chapter 7), where its magnitudes and signs could be important in the choice of a local or non-local turbulence model.

In summary, the following are concluded:

(1) The 'localness' of the turbulence, denoted by the inverse of $\tilde{L}_X$ and $\tilde{T}_L$, can be best understood as the 'non-sensitiveness' of the turbulence to the external forces. Such non-'localness' parameters (i.e. $\tilde{L}_X$ and $\tilde{T}_L$) signify the frequency of the occurrence of the discrete distortions.

(2) (i) Variations of basic physical properties in various complex flows necessitate the quantification of the statistical parameters for the purpose of turbulent predictions.

(ii) The numerical simulation databases have been able to be used to quantify the previous qualitative estimates for the two initial 'localness' quantities (i.e. $\tilde{L}_X$ and $\tilde{T}_L$), and to some extent, the strain parameter $\tilde{S}$.

(iii) The model equation for quantifying $\tilde{L}_X$ which was invented at the earlier stage of this work proves to be valid in turbulent boundary layer, provided that the domain of interest excludes the viscous sublayer region as well as that near outer boundary.

(iv) The finite difference quotients are practically useful in order to compute the first and second order derivatives (e.g. $\partial_i k$ and $\partial_i^2 \bar{u}$) to quantify the statistical parameters, in particular $\tilde{L}_X$ and $\tilde{S}$. Their reliability has successfully been shown.

(v) A full set of quantitative estimates could slightly vary from that of qualitative guidelines. The latter confirms the 'main' class in which the former lies.

(3) Two different turbulent flows which belong to the same main type of flow can be distinguished by unique combinations of the quantified statistical parameters.

(4) (i) The need for localness-based ZM in ACs is determined by a variable 'mixture' of UFRs in every AC, and the statistics of interest. Besides $\tilde{L}_X$ and $\tilde{T}_L$, parameter $\tilde{S}$ also (indirectly) affects the localness/non-localness of the turbulence, and consequently the models for AC.

(ii) The use of the numerical simulation databases has been extended to a broader range of UFRs in order to assess an example of AC for universal or zonal modelling.

(iii) Practically, while ZM is characterised by qualitative guidelines, the turbulence models of ACs can be firmly suggested by the quantitative parameter estimates.

(5) Analysis has also been extended to include $\tilde{G}$ at least for the baseline flows, by using the experimental results. Note that the significant limitations of current DNS/LES databases (e.g. those of the ERCOFTAC and the UKTC) are the lack of information concerning the third- and fourth-order correlations which are needed for the quantification of $\tilde{G}$, as well as the time-series data with which to describe spatial correlations.

8.2 Recommendations for future work

Much of the research represents the basics of a more vast capability and there remains a number of interesting possibilities that exist to extend, deepen or complete the work presented in this thesis:

(1) (i) More complex baseline cases have to be considered so as to provide a more realistic guideline on how to select the appropriate prediction method for a single and/or group of flows (e.g. AC-*combustion* turbulent flows) whose parameters quantitative values are known. Certain types of strain that is caused by the straining and rotational motion, however strong or weak, need to be taken into account.

(ii) The quantification method used in this work can be extended for the rest of the main types of turbulent flow given by Hunt and Savill in [1], and other UFRs. A complete set of main flows with quantitative estimates could be done to suggest 'best' turbulence models for UFRs which contribute to key industrial and environmental ACs.

(iii) Other AC-*external aerodynamics* examples and other AC sets could then be also addressed and analysed. Note that although a model example for AC-e*xternal aerodynamics* has been proposed, no models for five more ACs have been given. The process involved in proposing the former serves as a guideline for recommending the latter models.

(2) The degree of non-locality $\tilde{L}_X$ can be obtained in a more straightforward manner from the time series of the fluctuating velocities (e.g. u' across a turbulent flow), without the need to apply dimensional reasoning to the size of eddies (i.e. $L_X = k^{3/2}/\varepsilon$), provided that the large scale L_X is appropriately non-dimensionalised. Such an animation data is not included in most of the DNS/LES datasets, yet seems to be very useful.

(3) It is worth to apply third-order-accurate difference quotients in order to determine $\tilde{L}_X$, $\tilde{T}_L$, and $\tilde{S}$ to see whether the formula would give much better results, or only further improves the accuracy (which is less dramatic).

(4) (i) In the case of master-modes set for turbulent channel flow, the computation of the third- and fourth-moments could be made much faster when the post-analysis activities are minimised by utilising the DNS Web Server more fully, and when a single code is run for various outputs.

(ii) The robustness of the code used for manipulating master-modes set can be increased by programming a procedure that takes ensemble average of both one- and two-point correlations including higher order

one-point moments. This could be done by modifying the corresponding subroutine.

(5) Other dimensions and variations of mapping could be explored by:

(i) Taking into account all four statistical parameters (i.e. two 'localness' parameters and two structural parameters) so that the accuracy of the models for ACs might then be enhanced. This is especially of practical importance when dealing with turbulent flows which are bounded by solid surfaces (such as pipe walls or a compressor blade) or by fluid interfaces where the damping or disappearance of the turbulence takes place, and the Gaussian/non-Gaussian structure might be affected by external influences.

(ii) Exploring the relationship that is more complex between each UFR and the corresponding ACs, since a UFR is not necessarily unique to one single AC. This would then increase the number of choices for the models for ACs.

(6) More DNS with more complete datasets could also be carried out to improve the integrity of quantitative sets of 'localness'-structural parameters; each dataset should be able to provide sufficient information, including one-point higher-order correlations, in an effort to completely quantify the parameters.

REFERENCES

[1] Hunt, J. C. R. and Savill, A. M. (2005), "Guidelines and criteria for the use of turbulence models in complex flows", in Hewitt, G. F. (ed.) *Prediction of Turbulent Flows,* Cambridge University Press., UK, pp. 291-343.

[2] Hunt, J. C. R., Sandham, N. D., Vassilicos, J. C., Launder, B. E. and Monkewitz, P. A. and Hewitt, G.F. (2005), "Developments in the understanding and modelling of turbulence", in Hewitt, G. F. and Vassilicos,J.C. (ed.) *Prediction of turbulent flows,* Cambridge University Press., UK, pp. 5-49.

[3] Sovran, G. (1982), "A user's viewpoint on computational fluid dynamics", in Kline, S. J. (ed.), *Complex Turbulent Flows,* Vol. II, Stanford University, pp. 963.

[4] Tjonneland, E. (1982), "Prediction of turbulent flows -- a Boeing view", in Kline, S. J. (ed.), *Complex Turbulent Flows,* Vol. II, Stanford University, pp. 971.

[5] Savill, A. M. (1982), "Futuristic turbulence modelling?", in Kline, S. J. (ed.), *Complex Turbulent Flows,* Vol. II, Stanford University, pp. 971.

[6] Emmons, H. W., Chapman, D. R., Hill, P. G., Lilley, G. M., Lubert, M., Morkovin, M. V., Reynolds, W. C., Roache, P. and Steger, J. (1982), "Evaluation committee report", in Kline, S. J. (ed.), *Complex Turbulent Flows,* Vol. II, Stanford University, pp. 979.

[7] Prandtl, L. (1925), "Uber die ausgebildete turbulenze", *ZAMM,* vol. 5, pp. 136-139.

[8] Launder, B. E. (1989), "Second-moment closure: present… and future?", *International Journal of Heat and Fluid Flow,* vol. 10, no. 4, pp. 282-300.

[9] Van Driest, E. R. (1956), "On turbulent flow near a wall", *North American Aviation, Inc.,* vol. 23, no. 11, pp. 1007-1011.

[10] Hunt, J. C. R. and Carlotti, P. (2001), "Statistical Structure at the Wall of the High Reynolds Number Turbulent Boundary Layer", *Flow, Turbulence and Combustion,* vol. 66, pp. 453-475.

[11] Launder, B. E., Reece, G. J. and Rodi, W. (1975), "Progress in the development of a Reynolds stress turbulence closure ", *J .Fluid Mech.,* vol. 68, pp. 537-566.

[12] Durbin, P. A. and Pettersson-Reif, B. A. (2000), *Statistical Theory of Modelling for Turbulent Flow,* John Wiley.

[13] Clauser, F. H. (1956), "The Turbulent Boundary Layer", *Adv. Appl. Mech.,* vol. IV, pp. 1-51.

[14] Klebanoff, P. S. "Characteristics of turbulence in a boundary layer with zero pressure gradient", *NACA TN 3178*.

[15] Hunt, J. C. R. and Durbin, P. A. (1999), "Perturbed vortical layers and shear sheltering", *Fluid Dynamics Research,* vol. 24, no. 6, pp. 375-404.

[16] Lumley, J., Yang, Z. and Shih, T. (2000), "A Length-Scale Equation", *Flow, Turbulence and Combustion,* vol. 63, no. 1, pp. 1-21.

[17] Launder, B. E. e. a. (1982), "Ad-hoc committee reports", in Kline, S. J. (ed.), *Complex Turbulent Flows,* Vol. II, Stanford University, pp. 957.

[18] Cebeci, T. and Smith, A. M. O. (1974), *Analysis of turbulent boundary layers,* Academic Press.

[19] Baldwin, B. S. and Lomax, H. (1978), "Thin layer approximation and algebraic model for separated turbulent flows", *AIAA paper,* , pp. 78-257.

[20] Hallback, M. and Johansson, A. V. and Burden,A.D. (1996), "The Basics of Turbulence Modelling", in Hallback, M. (ed.) *Turbulence and Transition Modelling,* 1st Edition ed, Kluwer Academic Publisher, Netherlands, pp. 81-154.

[21] Prandtl, L. (1945), "Uber ein neues formelsystem die ausgebildete turbulenz", *Nacr. Akad Wiss. Gottingen, Math-Phys. Kl.,* , pp. 6-19.

[22] Wilcox, D. C. (2006), *Turbulence modelling for CFD,* 3rd ed, DCW inc, California, pp. 84-87.

[23] Baldwin, B. S. and Barth, T. J. (1990), "A one-equation turbulence transport model for high Reynolds number wall-bounded flows", *NASA TM-102847*.

[24] Spalart, P. R. and Allmaras, S. R. (1992), "A one-equation turbulence model for aerodynamic flows", *AIAA paper,* , pp. 92.

[25] Kolmogorov, A. N. (1942), "Equations of turbulent motion of an incompressible fluid", *Physics,* vol. 6, no. Nos. 1 and 2, pp. 56-58.

[26] Jones, W. P. and Launder, B. E. (1972), "The prediction of laminarization with a two-equation model of turbulence", *International Journal of Heat and Mass Transfer,* vol. 15, no. 2, pp. 301-314.

[27] Jones, W. P. and Launder, B. E. (1973), "The calculation of low-Reynolds-number phenomena with a two-equation model of turbulence", *International Journal of Heat and Mass Transfer,* vol. 16, no. 6, pp. 1119-1130.

[28] Rodi, W. and Mansour, N. N. (1993), "Low Reynolds number *k–e* modelling with the aid of direct simulation data", *J. Fluid Mech.,* vol. 250, pp. 509-529.

[29] Hunt, J. C. R., Kawai, H., Ramsey, S. R., Pedrizetti, G. and Perkins, R. J. (1990), "A review of velocity and pressure fluctuations in turbulent flows around bluff bodies", *Journal of Wind Engineering and Industrial Aerodynamics,* vol. 35, no. 1-3, pp. 49-85.

[30] Pope, S. B. (2000), *Turbulent Flows,* Cambridge University Press.

[31] Townsend, A. A. (1976), *The Structure of Turbulent Shear Flow,* Cambridge University Press.

[32] Marusic, I. and Perry, A. E. (1995), " A wall-wake model for turbulence structure of boundary layer – part 2: further experimental support", *J. Fluid Mech.,* vol. 298, pp. 389-407.

[33] Bradshaw, P. (1997), "Understanding and prediction of turbulent flow—1996", *International Journal of Heat and Fluid Flow,* vol. 18, no. 1, pp. 45-54.

[34] Murakami, S., Mochida, A. and Hayashi, Y. (1990), "Examining the k−∈ model by means of a wind tunnel test and large-eddy simulation of the turbulence structure around a cube", *Journal of Wind Engineering and Industrial Aerodynamics,* vol. 35, no. 1-3, pp. 87-100.

[35] Hunt, J. C. R. and Morrison, J. F. (2000), "Eddy structure in turbulent boundary layers", *European Journal of Mechanics - B/Fluids,* vol. 19, no. 5, pp. 673-694.

[36] Craft, T. J. and Launder, B. E. (1996), "A Reynolds stress closure designed for complex geometries", *International Journal of Heat and Fluid Flow,* vol. 17, no. 3, pp. 245-254.

[37] Lumley, J. L., Zeman, 0. and Siess, J. (1978), " The influence of buoyancy on turbulent transport ", *J. Fluid Mech.,* vol. 84, pp. 581-597.

[38] Wyngaard, J. C. (1979), "The atmospheric boundary layer — modelling and measurement", in Bradbury, L. J. S. (ed.) *Turbulent Shear Flows,* Springer-Verlag.

[39] Kim, K. C. and Adrian, R. J. (1999), "Very large-scale motion in the outer layer", *Phys. Fluids,* vol. 11, no. 2, pp. 417-422.

[40] Savill, A. M., (2008), *Viscous Flows* (Lecture Notes), *Computational Aerodynamics and Combustion Design Group*, Cranfield University.

[41] Bradshaw, P. (1971) "Variations on a theme of Prandtl", *AGARD Conference Proceedingson Turbulent Shear Flows,* pp. C- I.

[42] Hinze, J. O. (1975), *Turbulence,* 2nd ed, McGraw-Hill, New York.

[43] Reynolds, A. J. (1974), *Turbulent flows in engineering,* John Wiley.

[44] Schetz, J. A. (1993), *Boundary layer analysis,* Prentice Hall.

[45] Garde, R. J. (1994), *Turbulent flow,* John Wiley.

[46] Kays, W. M. and Crawford,M.E. (1980), "The differential equations of the boundary layer", in Holman, J. P. (ed.) *Convective Heat and Mass Transfer,* 2nd ed, McGraw-Hill, US, pp. 17-44.

[47] Kays, W. M. and Crawford,M.E. (1980), "Momentum transfer: The turbulent momentum boundary layer", in Holman, J. P. (ed.) *Convective Heat and Mass Transfer,* 2nd ed, McGraw-Hill, US, pp. 161-195.

[48] Launder, B. E. and Spalding, D. B. (1972), *Lectures in mathematical models of turbulence,* Academic Press.

[49] Chen, C. -. and Jaw, S. -. (1997), *Fundamentals of turbulence modelling,* Taylor Francis Group.

[50] Tennekes, H. and Lumley, J. L. (1972), *A first course in turbulence,* MIT Press.

[51] Libby, P. A. (1996), *An introduction to turbulence,* CRC Press.

[52] Sandham, N. D. (2005), "Turbulence simulation", in Hewitt, G. F. (ed.) *Prediction of turbulent flows,* Cambridge University Press., UK, pp. 217-227.

[53] ERCOFTAC (2011), "Application Areas and Underlying Flow Regimes", QNET-CFD Wiki Home Page, *http://qnet-ercoftac.cfms.org.uk/w/index.php/Main_Page*

[54] *Best Practice Guidelines,* (2000), Version 1.0 ed, ERCOFTAC, Europe.

[55] Kline, S. J. (1982), "Universal or zonal modelling - the road ahead", in Kline, S. J. (ed.), *Complex Turbulent Flows,* Vol. II, Stanford University, pp. 991.

[56] Morrison, J. F. (2005), "Boundary layers under strong distortion: an experimentalist's view", in Hewitt, G. F. (ed.) *Prediction of Turbulent Flows,* Cambridge University Press., UK, pp. 163-206.

[57] Abdullah, A. and Savill, A. M. (2008), "Matching conditions for the use of turbulence models in complex flows" *UKTC Workshop*, New Forest, UK, Sept. 1-2, 2008.

[58] Kenjeres, S. and Hanjalic, K. (1999), "Transient analysis of Rayleigh–Bénard convection with a RANS model", *International Journal of Heat and Fluid Flow,* vol. 20, no. 3, pp. 329-340.

[59] Launder, B. E. and Sandham, N. D. (eds.) (2002), *Closure Strategies for Turbulent and Transitional Flows,* Cambridge University Press.

[60] Sagaut, P. (2001), *Large Eddy Simulation for Incompressible Flows,* second ed, Springer.

[61] Hunt, J. C. R., Sandham, N., Vassilicos, J. C., Launder, B. E., Mokewitz, P. A. and Hewitt, G. F. (2001), " Developments in turbulence research: a review based on the 1999 programme of the Isaac Newton Institute. Cambridge", *J. Fluid Mech.,* vol. 436, pp. 393-407.

[62] Belcher, S. E., Weng, W. S. and Hunt, J. C. R. (1991) "Structure of turbulent boundary layers perturbed over short length scales", *Eighth Symp. on Turb. Shear Flows,* paper 12-2 Tech. Univ. of Munich.

[63] Hutton, A. G. (2003), "The prediction of turbulent flows in industrial application", *The INI Workshop 'Prediction of Turbulent Flows',* 7.11.2003, Cambridge University, INI, UK.

[64] Yang and Voke "Flat plate transitional boundary layers", in *ERCOFTAC Database.*

[65] Spalart "Constant-pressure boundary layer DNS", in *ERCOFTAC Database.*

[66] Spalart "Sink-flow boundary layer", in *ERCOFTAC Database.*

[67] Le and Moin "Backward-facing step", in *ERCOFTAC Database.*

[68] Kim and Moin and Moser "Channel flow DNS", in *ERCOFTAC Database.*

[69] Matsumoto, A. and Nagano, Y. a. T.,T. "Homogeneous turbulent shear flow DNS", in *ERCOFTAC Database.*

[70] Abdullah, A. and Savill, A. M. (2009), "Industrial guidelines progress and requirements", *UKTC Conference*, New Forest, UK, Sept. 21-22, 2009.

[71] Kreplin, H. and Eckelmann, H. (1979), "Behaviour of the three fluctuating velocity components in the wall region of a turbulent channel flow", *Phys. Fluids,* vol. 22, pp. 12-33.

[72] Britter, R. E., Hunt, J. C. R. and Mumford, J. C. (1979), " The distortion of turbulence by a circular cylinder ", *J. Fluid Mech.,* vol. 92, pp. 269-301.

[73] Godeferd, F. S., Cambon, C. and Scott, J. F. (2001), " Two-point closures and their applications: report on a workshop ", *J. Fluid Mech.,* vol. 436, pp. 393-407.

[74] Anderson, J. D. (1995), "Grids with Appropriate Transformations", in Corrigan, J. J. (ed.) *Computational Fluid Dynamics: The Basics with Applications,* International Editions 1995 ed, McGraw-Hill, Inc., New York, pp. 168-215.

[75] Savill, A. M. (2006), "From DNS to applications", *UK Turbulence Workshop,* 2006, New Forest, UK Turbulence HPCC, UK.

[76] Spanelis, A., (2011), "Fully developed incompressible single round jet LES", *Computational Aerodynamics and Combustion Design Group*, Cranfield University.

[77] Kassinos, S. C., Reynolds, W. C. and Rogers, M. M. (2001), "One point turbulence structure tensors", *J. Fluid Mech.,* vol. 428, pp. 213-248.

[78] Oberlack, M. and Busse, F. (eds.) (2002), *Theories of Turbulence,* Springer-Verlag.

[79] Coleman, G.N., (2009), "Decelerating wall bounded turbulent flow DNS", *Aerodynamics and Flight Mechanics Research Group*, University of Southampton.

[80] Cambon, C. and Scott, J. F. (1999), "Linear and nonlinear models of anisotropic turbulence", *Annu. Rev. Fluid Mech.,* vol. 31, pp. 1-53.

[81] Fabris, G. (1983), "Higher-order statistics of turbulent fluctuations in the plane wake", *American Institute of Physics,* vol. 26, no. 6, pp. 1437-1445.

[82] Abdullah, A. and Savill, A. M. (2010), "Simulation guideline parameters for classifying turbulent flows and their Modeling", *UKTC Conference*, London, UK, Sept. 1-2, 2010.

[83] Roger, L. S., Chew, Y. T. and Shivaprasad, B. G. (1981), "The structure of a separating turbulent boundary layer. Part 2. Higher-order turbulence results", *J. Fluid Mech.,* vol. 113, pp. 53-73.

[84] Ichimiya, M., Nakamura, I. and Yamashita, S. (1998), "Properties of a relaminarizing turbulent boundary layer under a favorable pressure gradient", *Experimental Thermal and Fluid Science,* vol. 17, pp. 37-48.

[85] Fernholz, H. H. and Finley, P. J. (1996), "The incompressible zero-pressure-gradient turbulent boundary layer: an assessment of the data", *Prog. Aerospace Sci.,* vol. 32, pp. 245-311.

[86] Hancock, P. E. (2007), "Scaling of the near-wall layer beneath turbulent separated flow", *European Journal of Mechanics B/Fluids,* vol. 26, pp. 271-283.

[87] Karabasov, S. A., Afsar, M. Z., Hynes, T. P., Dowling, A. P., McMullan, W. A., Pokora, C. D., Page, G. J. and McGuirk, J. J. (2008), "Using large eddy simulation within an acoustic analogy approach for jet noise modelling", *14th AIAA/CEAS Aeroacoustics Conference*, Vancouver, Canada, May 5-7, 2008, pp. 2630-2645.

[88] Ranga Dinesh, K. K. J., (2009), "A round jet in co-flow LES", *Computational Aerodynamics and Combustion Design Group*, Cranfield University.

[89] Dengel, P. and Fernholz, H. H. (1990), " An experimental investigation of an incompressible turbulent boundary layer in the vicinity of separation ", *J. Fluid Mech.,* vol. 212, pp. 615-636.

[90] Launder, B. E. and Spalding, D. B. (1974), "The numerical computation of turbulent flows", *Computer Methods in Applied Mechanics and Engineering,* vol. 3, no. 2, pp. 269-289.

[91] Savill, A. M. (1996), "One point closures applied to transition", in Hallback, M., Henningson, D. S., Johnsson, A. V., et al (eds.) *Turbulence and Transition Modelling,* Kluwer Academic Press.

[92] Savill, A. M. (1987), "Recent developments in rapid-distortion theory", *Ann. Rev. Fluid Mech.,* vol. 19, pp. 521-53l.

[93] Belcher, S. E., Newley, T. M. J. and Hunt, J. C. R. (1993), "The drag on an undulating surface induced by the flow of a turbulent boundary layer", *J. Fluid Mech.,* vol. 249, pp. 557-596.

[94] Hunt, J. C. R. and Carruthers, D. J. (1990), " Rapid distortion theory and the 'problems' of turbulence ", *J. Fluid Mech.,* vol. 212, pp. 497-532.

[95] Gibson, M. M. and Launder, B. E. (1978), " Ground effects on pressure atmospheric boundary layer ", *J. Fluid Mech.,* vol. 86, pp. 49 1-511.

[96] Durbin, P. A. (1993), " A Reynolds stress model for near wall turbulence", *J. Fluid Mech.,* vol. 249, pp. 465-498.

[97] Lombardi, P., Angelis, V. D. and Banerjeeb, S. (1996), "Direct numerical simulation of near-interface turbulence in coupled gas-liquid flow", *Phys. Fluids,* vol. Vol. 8, no. No. 6, pp. 1643-1665.

[98] Teixeira, M. A. C. and Belcher, S. E. (2000), " Dissipation of shear-free turbulence near boundaries ", *J. Fluid Mech.,* vol. 422, pp. 167-191.

[99] Champagne, F. H., Harris, V. G. and Corrsin, S. (1970), " Experiments on nearly homogeneous turbulent shear flow ", *J. Fluid Mech.,* vol. 41, pp. 81-139.

[100] Abdullah, A. and Savill, A. M. (2010) "Quantification of statistical parameters for classifying complex turbulent flows", *European Fluid Mechanics Conference-8*, Bad Reichenhall, Germany, Sept. 13-16, 2010.

[101] Murlis, J., Tsai, H. M. and Bradshaw, P. (1982), "The structure of turbulent boundary layers at low Reynolds numbers", *J. Fluid Mech.,* vol. 122, pp. 13-56.

[102] Bisset, D. K., Hunt, J. C. R. and Rogers, M. M. (2002), " The turbulent/interface bounding a far wake", *J. Fluid Mech.,* vol. 451, pp. 383-410.

[103] Chernyshenko, S. I. and Bondarenko, M. E. "Master-modes in 3D turbulent channel flow", *Under consideration for publication in J. Fluid Mech.*

[104] Chernyshenko, S. I., "The DNS Database Web Server and Master-Mode Database User Manual", *Aerodynamics and Flight Mechanics (AFM) Research Group,* University of Southampton.

PUBLICATIONS

1. Abdullah, A. and Savill, A. M. (2008), "Matching conditions for the use of turbulence models in complex flows" *UKTC Workshop*, New Forest, UK, Sept. 1-2, 2008.

2. Abdullah, A. and Savill, A. M. (2009), "Industrial guidelines progress and requirements", *UKTC Conference*, New Forest, UK, Sept. 21-22, 2009.

3. Abdullah, A. and Savill, A. M. (2010), "Simulation guideline parameters for classifying turbulent flows and their Modeling", *UKTC Conference*, London, UK, Sept. 1-2, 2010.

4. Abdullah, A. and Savill, A. M. (2010) "Quantification of statistical parameters for classifying complex turbulent flows", *European Fluid Mechanics Conference-8*, Bad Reichenhall, Germany, Sept. 13-16, 2010.

APPENDICES

Appendix A
Boundary layer data

```
Mean and mean-square fluctuations:
  J    y/delta      y+           U+          uu+         vv+         ww+         uv+
  1  1.5089E-03  2.3066E-01  2.3072E-01  7.8927E-03  4.1944E-07  3.0906E-03 -1.3901E-05
  :      :           :           :           :           :           :           :
 48  2.7574E+00  4.2153E+02  1.8527E+01  3.2146E-04  4.3371E-04  8.0414E-05  1.1595E-05

Budget of uu:
  J      y+         Diss         Prod    vel_p_grad   turb_diff   visc_diff  advection      sum
  1  2.3066E-01 -2.9551E-01  2.7812E-05  1.5695E-03  4.1402E-05  2.9376E-01  2.0426E-08 -1.0345E-04
  :      :           :           :           :           :           :           :           :
 48  4.2153E+02 -1.3564E-06 -1.9603E-11  4.3271E-06 -4.9041E-09  6.0233E-08 -2.2049E-06  8.2105E-07

Budget of vv:
  :      :           :           :           :           :           :           :           :
Budget of ww:
  :      :           :           :           :           :           :           :           :
Budget of uv:
  :      :           :           :           :           :           :           :           :

Budget of uu+vv+ww:
  J      y+         Diss         Prod    vel_p_grad   turb_diff   visc_diff  advection      sum
  1  2.3066E-01 -4.0533E-01  2.7812E-05  8.5066E-03  3.8855E-05  3.9660E-01 -7.4356E-08 -1.6434E-04
  :      :           :           :           :           :           :           :           :
 48  4.2153E+02 -2.7039E-06 -1.9603E-11  8.5010E-06 -2.4941E-10  1.1511E-07 -4.5503E-06  1.3616E-06

Re_delta* = 1000, Re_theta = 670, Re_delta+ = 325.
  :      :           :           :           :           :           :           :
Re_delta* = 2000, Re_theta = 1410, Re_delta+ = 650.
  :      :           :           :           :           :           :           :
```

Boundary layer data, reproduced with simplification from [65], at Re_delta* = 500, Re_theta = 300, Re_delta+ = 150. All quantities are normalised by u_tau and nu unless stated otherwise. The data are compiled from [65].

Appendix B
Variations of statistical parameters

B.1 The degree of non-locality

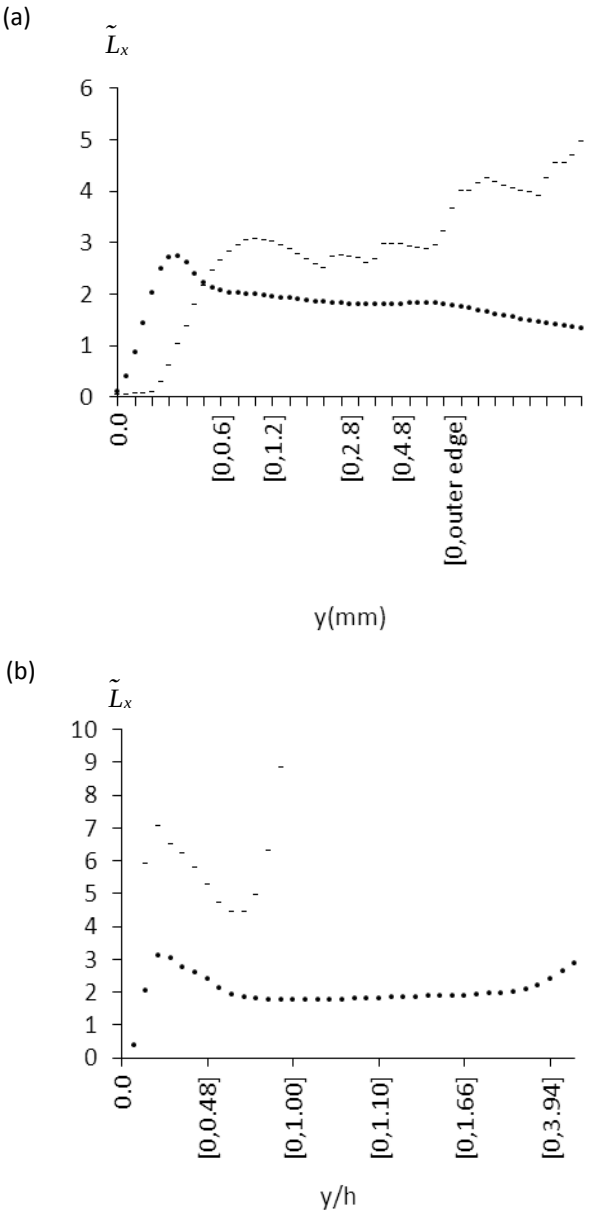

Figure B-1
(a) Flat plate transitional boundary layer (LES by Yang and Voke, 1993).
Note: Graphs are presented using a *fixed-point* approach.
(b) Shear layer impingement, i.e. around reattachment in the flow over rearward facing step (Le and Moin, 1992), at $Re_h = 5100$, where h is the step height.

(c)

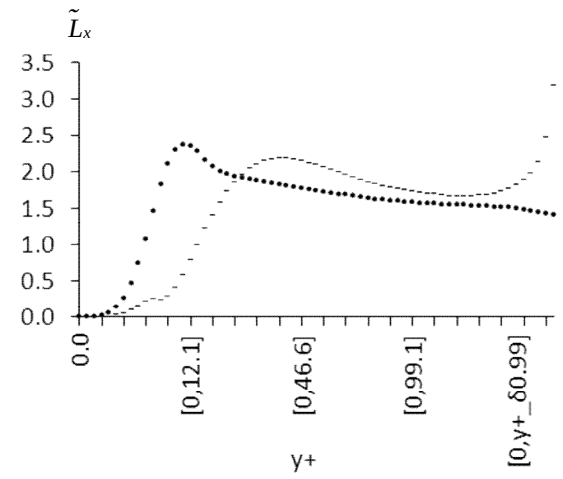

(d)

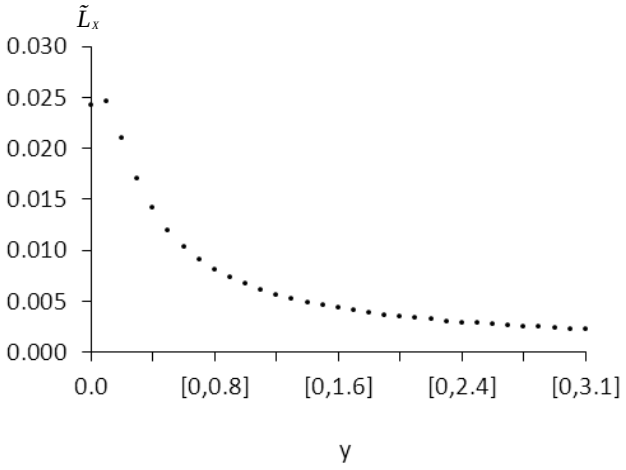

Figure B-1 *(continued)*

(c) Channel flow (DNS by Kim et al., 1987) at $Re_{\tau/2} = 3250$. Note that d is the diameter of the channel.

(d) Sheared homogeneous turbulent flow (DNS by Matsumoto and Nagano).

(e)

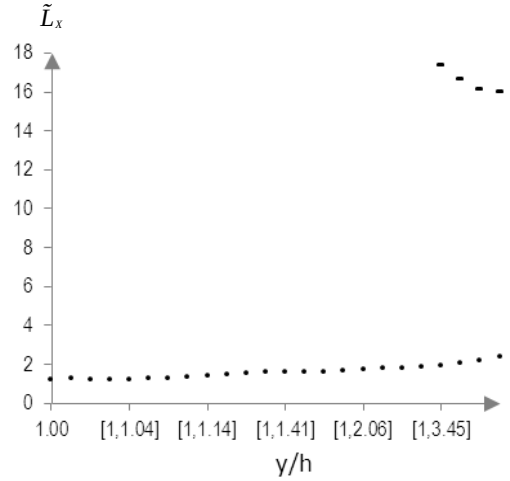

(f)

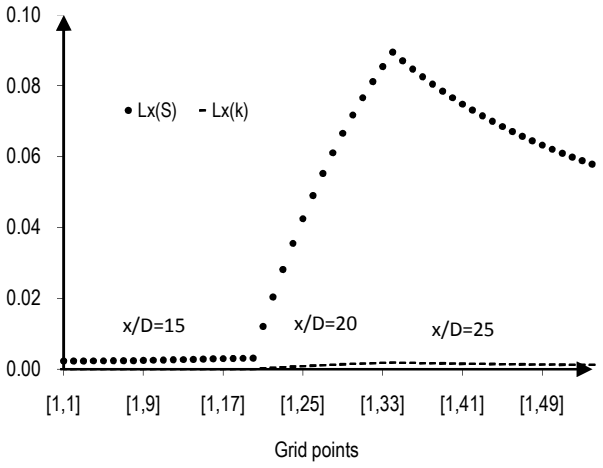

Figure B-1 *(continued)*

(e) Free shear flow, a zone in the flow over rearward facing step (Le and Moin, 1992), at $Re_h = 5100$, where h is the step height.

(f) Single round jet [76].

B.2 The degree of non-equilibrium

(a)

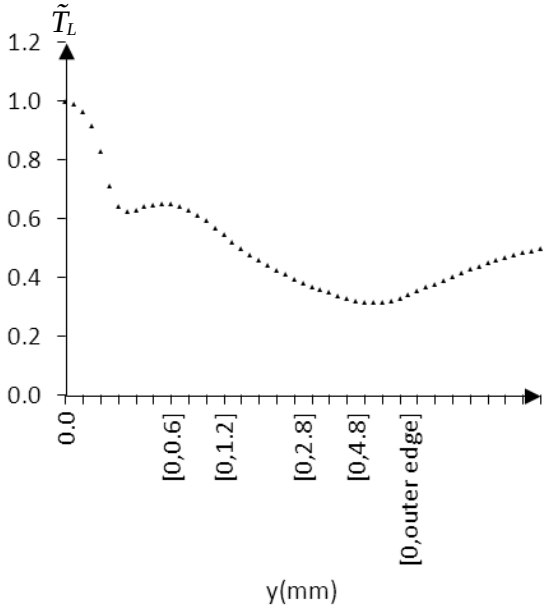

(b)

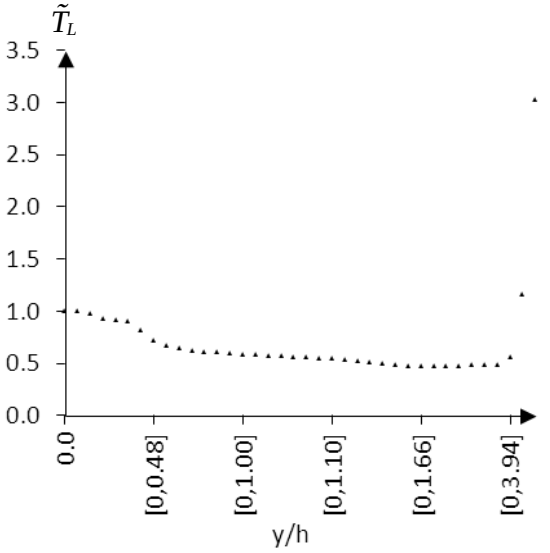

Figure B-2
(a) Flat plate transitional boundary layer (LES by Yang and Voke, 1993).
(b) Shear layer impingement, i.e. around reattachment in the flow over rearward facing step (Le and Moin, 1992), at $Re_h = 5100$, where h is the step height.

(c)

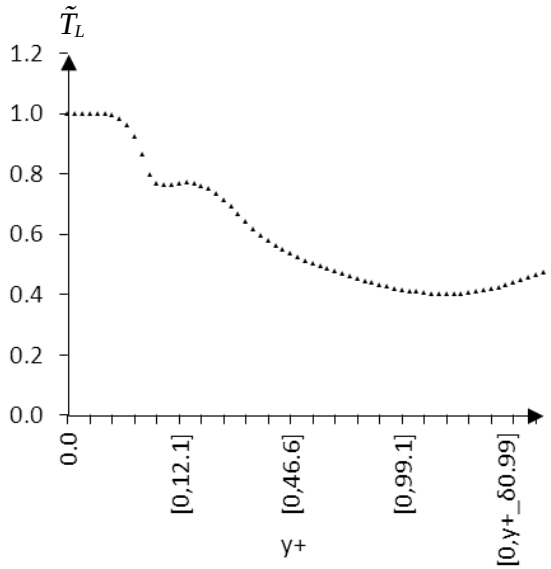

(d)

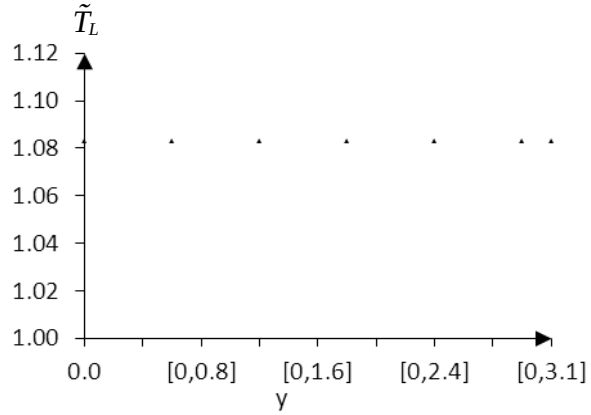

Figure B-2 *(continued)*

(c) Channel flow (DNS by Kim et al., 1987) at $Re_{d/2} = 3250$. Note that d is the diameter of the channel.

(d) Sheared homogeneous turbulent flow (DNS by Matsumoto and Nagano).

(e)

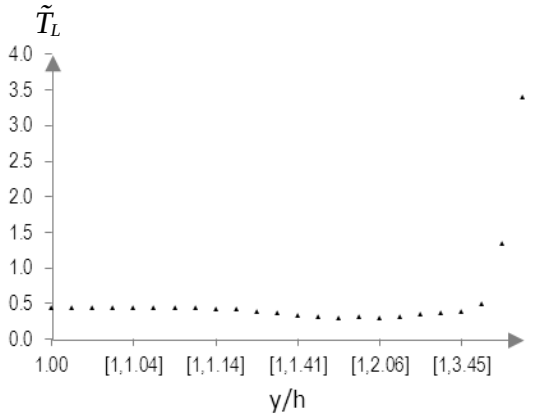

(f)

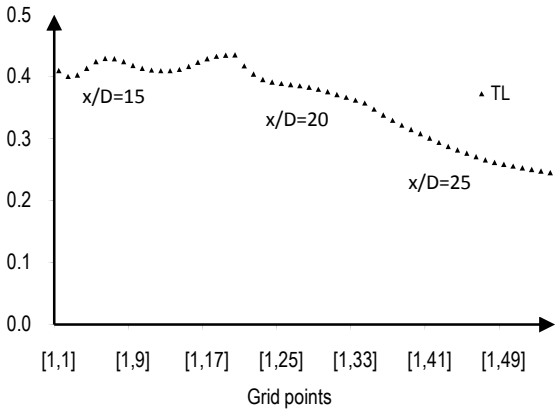

Figure B-2 *(continued)*

(e) Free shear flow, a zone in the flow over rearward facing step (Le and Moin, 1992), at $Re_h = 5100$, where h is the step height.

(f) Single round jet [76].

B.3 The strain parameter

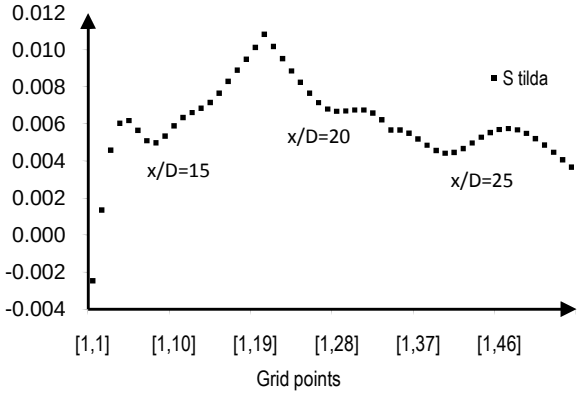

Figure B-3 Single round jet [76].

B.4 The degree of non-Gaussianity

y+	Ku	Su
1.63	4.610	1.025
2.11	4.250	0.935
2.44	4.070	0.980
2.66	4.340	1.070
3.00	3.800	0.980
3.72	3.620	0.890
4.08	3.530	0.800
5.00	3.440	0.845
5.99	2.900	0.440
7.31	2.630	0.440
8.96	2.270	0.260
10.00	2.225	0.125
14.69	2.270	-0.190
16.70	2.279	-0.190
18.71	2.360	-0.235
20.00	2.450	-0.325
30.00	2.810	-0.550
42.74	3.080	-0.595
50.00	3.080	-0.460
64.99	3.080	-0.415
93.29	3.170	-0.550
100.00	3.170	-0.595
200.00	3.530	-0.640

y+	Kv	Sv
3.54	3.710	0.980
7.31	4.610	0.305
10.67	4.745	0.305
15.70	4.925	0.170
29.99	3.800	0.080
46.38	3.485	0.125
83.30	3.440	0.170
146.69	3.530	0.215
200.00	3.485	0.000

y+	Kw	Sw
1.67	5.475	0.080
2.11	5.250	0.035
2.39	5.340	-0.010
2.66	4.845	0.080
3.00	4.800	0.057
3.72	4.755	-0.010
4.17	4.440	0.013
5.00	4.215	-0.100
5.99	3.990	-0.033
7.31	3.765	0.035
8.96	3.405	-0.010
9.95	3.315	-0.033
14.69	3.000	0.035
16.70	2.865	-0.033
18.71	2.910	-0.010
20.00	2.910	-0.010
30.00	2.910	-0.010
41.83	2.955	0.035
50.00	3.000	0.035
64.99	3.045	0.013
93.29	3.135	-0.010
99.95	3.225	0.057
200.00	3.495	0.035

Table B-4a Quadruple K_u and and triple S_u correlation functions collected from [71]. The corresponding plots are shown in Figure B-4a.

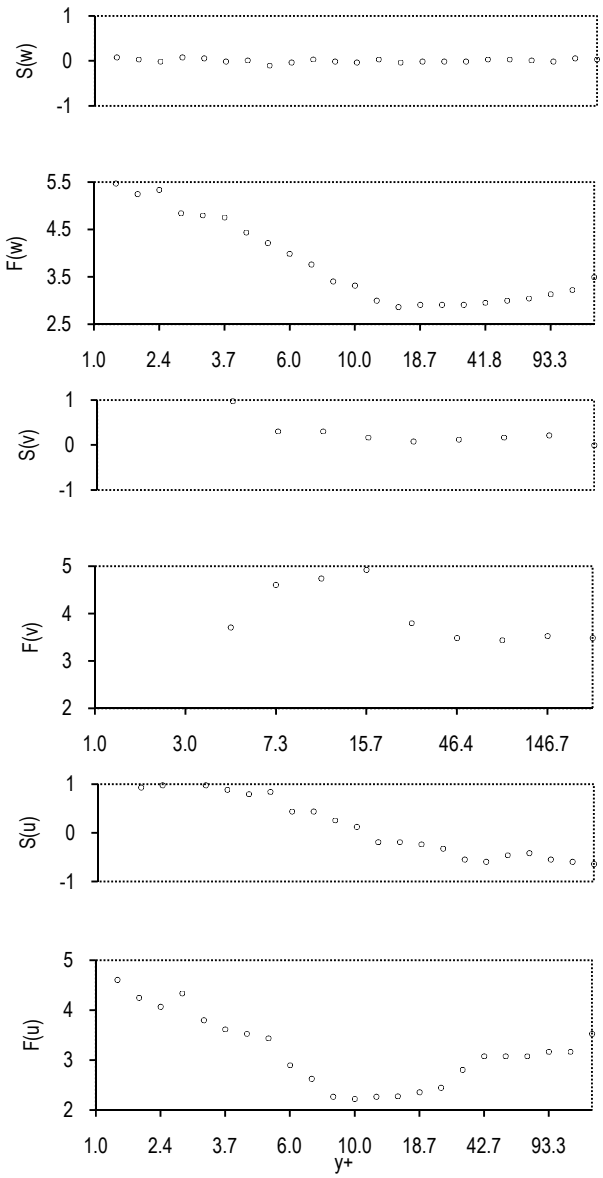

Figure B-4a Correlation functions obtained from the experiment [71]. The 4th- and 3rd-order correlations are represented by $K(u_i)$ and $S(u_i)$, respectively, where the subscript index i=1,2,3, and u_1 = u, u_2 = v, and u_3 = w.

Separating turbulent boundary layer

y+	K_u	G_K
2.04	5.040	2.040
3.02	4.835	1.835
4.15	4.273	1.273
5.19	3.761	0.761
6.26	3.429	0.429
7.27	3.148	0.148
9.45	2.892	0.108
13.49	2.713	0.287
15.97	2.713	0.287
20.37	2.918	0.082
26.97	3.148	0.148
53.91	3.582	0.582
72.74	3.621	0.621
89.38	3.582	0.582
107.78	3.557	0.557
185.48	3.352	0.352
236.58	3.403	0.403
285.29	3.480	0.480
344.02	3.480	0.480

y+	S_u	G_s
1.96	0.813	0.813
3.02	0.781	0.781
4.07	0.702	0.702
5.00	0.622	0.622
6.50	0.431	0.431
7.27	0.352	0.352
9.45	0.256	0.256
14.01	0.050	0.050
16.89	-0.030	0.030
21.54	-0.149	0.149
27.48	-0.300	0.300
55.97	-0.467	0.467
68.77	-0.467	0.467
89.38	-0.443	0.443
109.81	-0.420	0.420
196.19	-0.364	0.364
227.89	-0.380	0.380
280.00	-0.396	0.396
344.02	-0.396	0.396

y+	G
2.04	2.040
3.02	1.835
4.15	1.273
5.19	0.761
6.26	0.431
7.27	0.352
9.45	0.256
13.49	0.287
15.97	0.287
20.37	0.149
26.97	0.300
53.91	0.582
72.74	0.621
89.38	0.582
107.78	0.557
185.48	0.364
236.58	0.403
285.29	0.480
344.02	0.480
Average	0.486

Table B-4a The corresponding plots are shown in Figure B-4(1).

1(a)

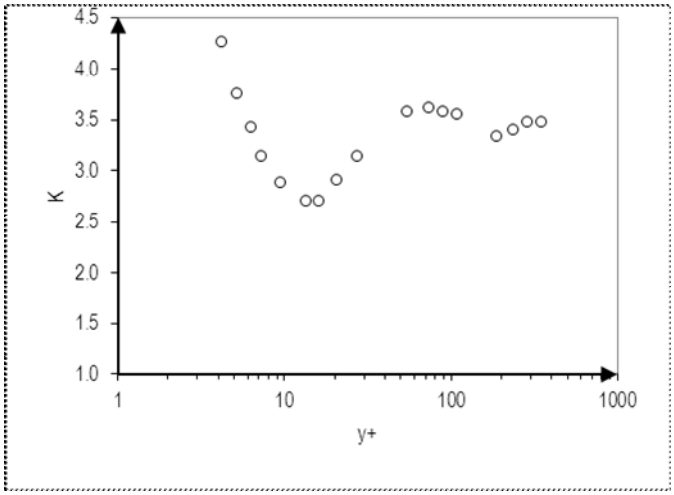

1(b)

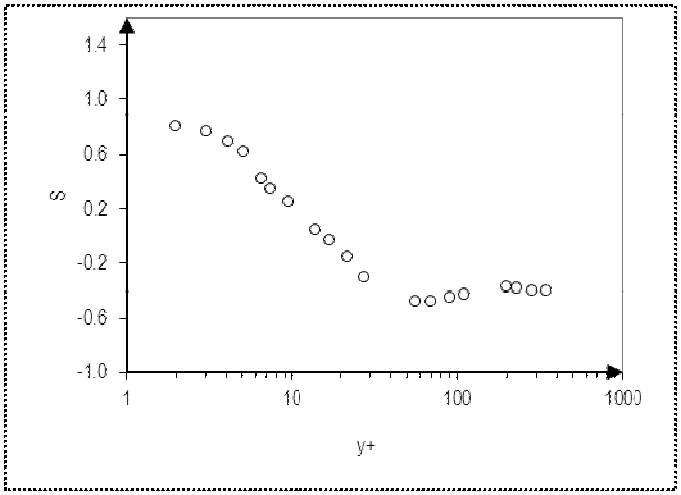

Figure B-4(1) Separating turbulent boundary layer [83].
1(a), 1(b) Variations of Kurtosis K and Skewness S factors, respectively.

1(c)

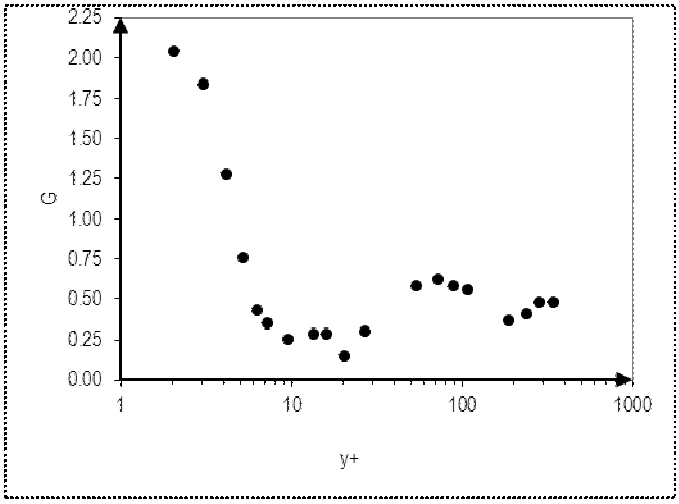

Figure B-4(1) *(continued)*

1(c) Variation of the degree of non-Gaussianity $\tilde{G}$.

Turbulent boundary layer under a favourable pressure gradient

	y+ = 12		y+ = 30		
$x/delta_o$	K_u	G_{Ku}	K_u	G_{Ku}	$G_{Ku\ average}$
-40.00	2.498	0.502	2.617	0.383	0.443
-30.10	2.287	0.713	2.715	0.285	0.499
-29.28	2.266	0.734	2.813	0.187	0.460
-21.03	2.280	0.720	2.757	0.243	0.481
-16.91	2.301	0.699	2.715	0.285	0.492
-12.78	2.336	0.664	2.778	0.222	0.443
-9.07	2.315	0.685	2.785	0.215	0.450
-4.12	2.336	0.664	2.785	0.215	0.439
-2.06	2.287	0.713	2.827	0.173	0.443
0.41	2.266	0.734	2.855	0.145	0.439
2.06	2.287	0.713	2.855	0.145	0.429
4.12	2.203	0.797	2.995	0.005	0.401
5.77	2.154	0.846	3.037	0.037	0.442
7.84	2.196	0.804	3.150	0.150	0.477
10.31	2.238	0.762	3.199	0.199	0.480
11.55	2.336	0.664	3.360	0.360	0.512
12.78	2.379	0.621	3.206	0.206	0.414
14.43	2.540	0.460	2.953	0.047	0.254
17.32	2.883	0.117	3.164	0.164	0.140
19.38	3.150	0.150	3.206	0.206	0.178
21.44	3.304	0.304	3.136	0.136	0.220
23.51	3.199	0.199	2.953	0.047	0.123
25.57	3.009	0.009	2.757	0.243	0.126
29.28	2.322	0.678	2.813	0.187	0.432
33.40	2.673	0.327	2.757	0.243	0.285
38.35	2.561	0.439	2.645	0.355	0.397
42.06	2.561	0.439	2.645	0.355	0.397

Table B-4b The corresponding plots are shown in Figure B-4(2).

	y+=12		y+ = 30				
x/delta$_o$	S_u	G_{Su}	S_u	G_{Su}	$G_{Su\ average}$		G
-40.00	0.019	0.019	-0.108	0.108	0.064		0.443
-30.10	-0.108	0.108	-0.257	0.257	0.183		0.499
-29.28	-0.101	0.101	-0.300	0.300	0.200		0.460
-21.03	-0.151	0.151	-0.278	0.278	0.215		0.481
-16.91	-0.144	0.144	-0.264	0.264	0.204		0.492
-12.78	-0.151	0.151	-0.264	0.264	0.208		0.443
-9.07	-0.151	0.151	-0.335	0.335	0.243		0.450
-4.12	-0.123	0.123	-0.300	0.300	0.211		0.439
-2.06	-0.165	0.165	-0.335	0.335	0.250		0.443
0.41	-0.151	0.151	-0.335	0.335	0.243		0.439
2.06	-0.222	0.222	-0.413	0.413	0.317		0.429
4.12	-0.172	0.172	-0.618	0.618	0.395		0.401
5.77	-0.038	0.038	-0.618	0.618	0.328		0.442
7.84	-0.108	0.108	-0.788	0.788	0.448		0.477
10.31	-0.080	0.080	-0.830	0.830	0.455		0.480
11.55	-0.002	0.002	-0.844	0.844	0.423		0.512
12.78	-0.031	0.031	-0.887	0.887	0.459		0.459
14.43	0.132	0.132	-0.759	0.759	0.446		0.446
17.32	0.295	0.295	-0.880	0.880	0.587		0.587
19.38	0.344	0.344	-0.887	0.887	0.616		0.616
21.44	0.401	0.401	-0.830	0.830	0.616		0.616
23.51	0.443	0.443	-0.689	0.689	0.566		0.566
25.57	0.585	0.585	-0.561	0.561	0.573		0.573
29.28	0.075	0.075	-0.328	0.328	0.202		0.432
33.40	0.075	0.075	-0.094	0.094	0.085		0.285
38.35	0.175	0.175	0.012	0.012	0.093		0.397
42.06	0.189	0.189	0.012	0.012	0.100		0.397
						Average	0.470

Table B-4b *(continued)*

2(a)

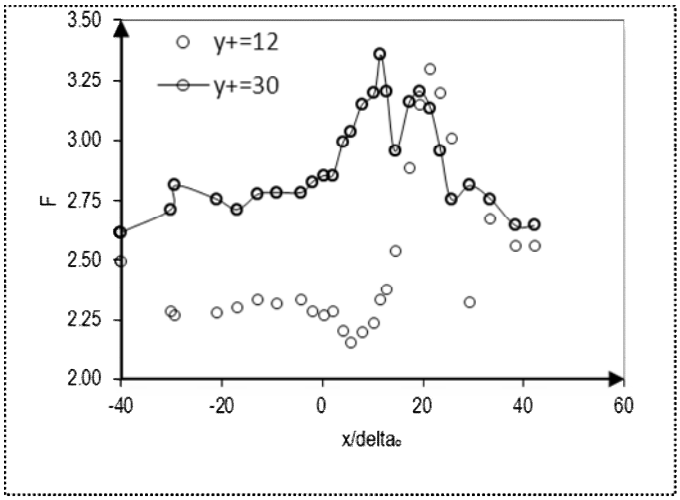

2(b)

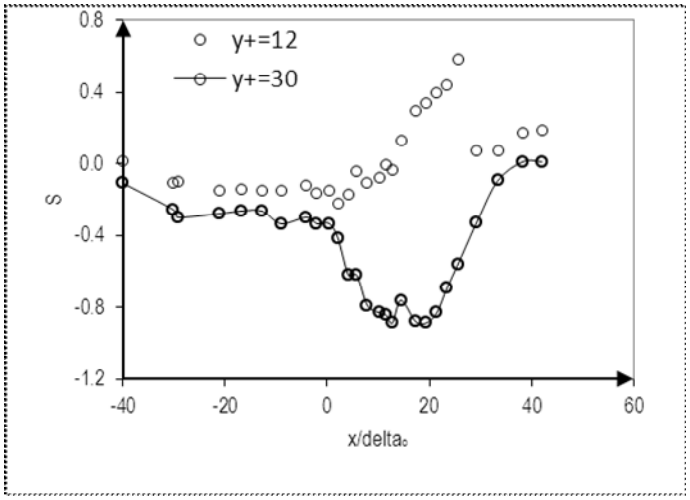

Figure B-4(2) Turbulent boundary layer under a favourable pressure gradient [84]. Variations of; 2(a) Kurtosis factor K. 2(b) Skewness factor *S*.

2(c)

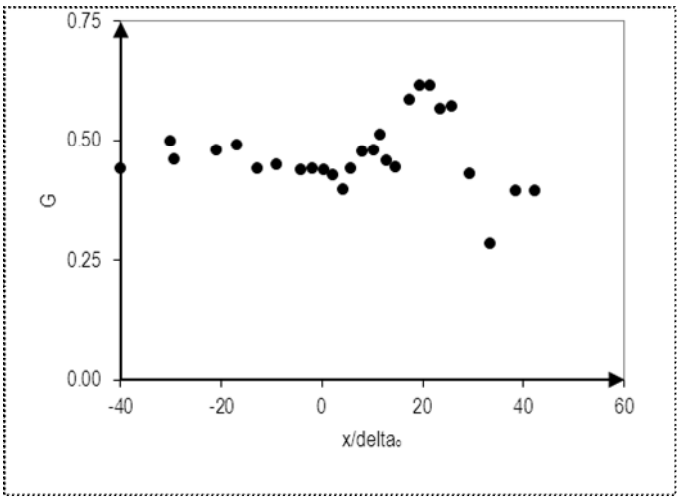

Figure B-4(2) *(continued)* Variation the degree of non-Gaussianity $\tilde{G}$.

Zero pressure gradient turbulent boundary layer

y/Δ	K_u	K_v	K_w	G_K	y/Δ	S_u	S_v	G_S
0.007	2.649	4.317	3.425	0.698	0.004	0.114	0.439	0.277
0.011	2.794	3.988	3.425	0.540	0.007	-0.248	0.512	0.380
0.019	2.794	3.841	3.203	0.417	0.010	-0.248	0.329	0.289
0.031	2.830	3.439	3.072	0.227	0.012	-0.175	0.238	0.207
0.073	2.794	3.146	3.072	0.141	0.018	-0.175	0.146	0.161
0.131	3.156	3.402	3.203	0.254	0.026	-0.103	0.183	0.143
0.177	3.735	4.098	4.157	0.997	0.039	-0.031	0.293	0.162
0.231	10.833	6.439	6.065	4.779	0.137	-0.429	0.366	0.397
					0.185	-0.827	0.768	0.798
					0.236	-2.058	1.244	1.651

y/Δ	G	
0.007	0.698	
0.011	0.540	
0.019	0.417	
0.029	0.227	
0.056	0.162	
0.134	0.397	
0.181	0.997	
0.234	4.779	
Average	1.584	(wall layer is excluded)

Table B-4c The corresponding plots are shown in Figure B-4(3).

3(a)

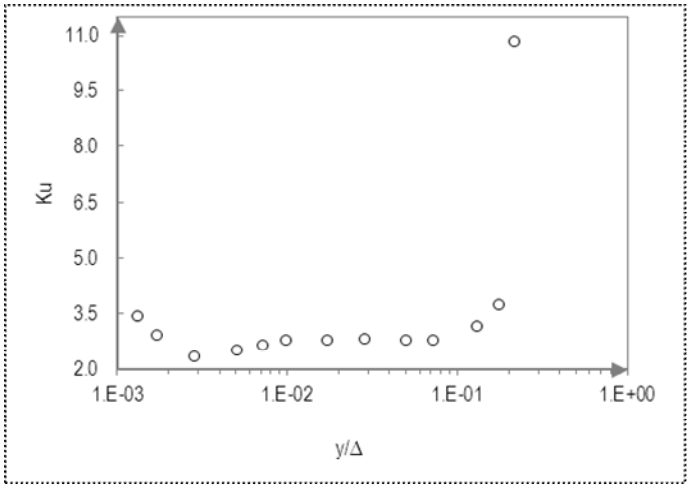

3(b)

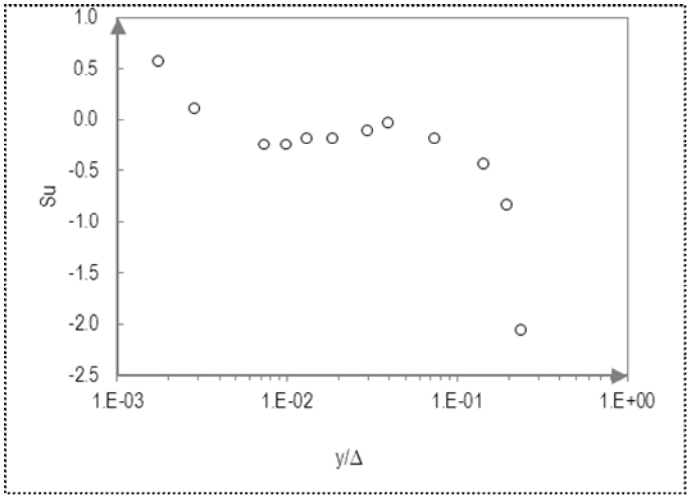

Figure B-4(3) Zero pressure gradient turbulent boundary layer
3(a), 3(b) Variations of Kurtosis K and Skewness *S* factors, respectively, of the streamwise fluctuating velocities u distribution.

3(c)

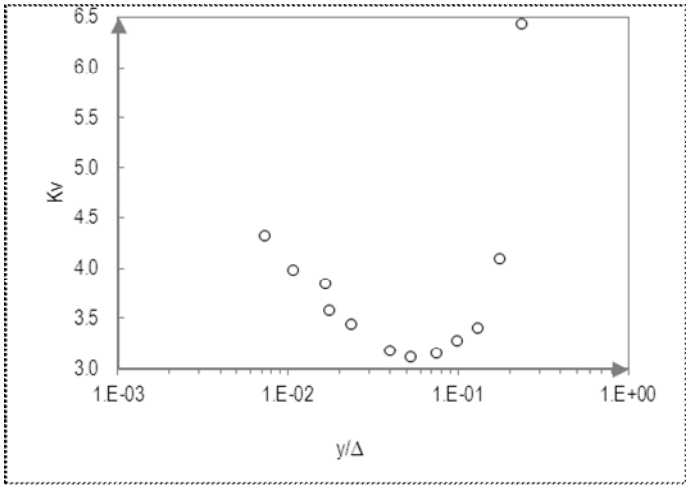

3(d)

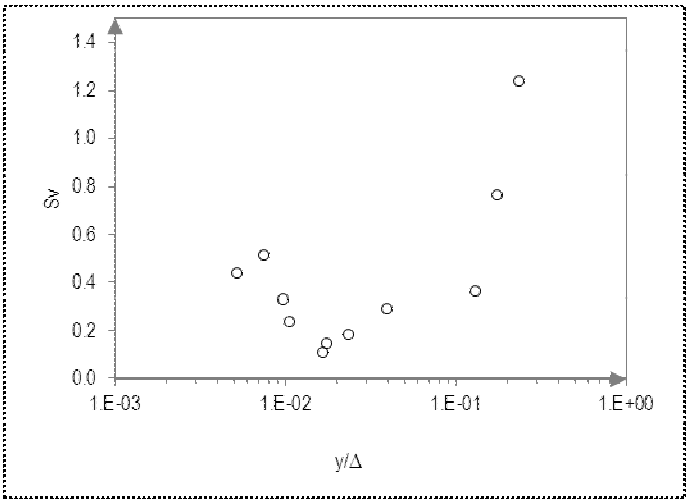

Figure B-4(3) *(continued)*
3(c), 3(d) Variations of Kurtosis K and Skewness S factors, respectively, of the wall normal fluctuating velocities v distribution.

3(e)

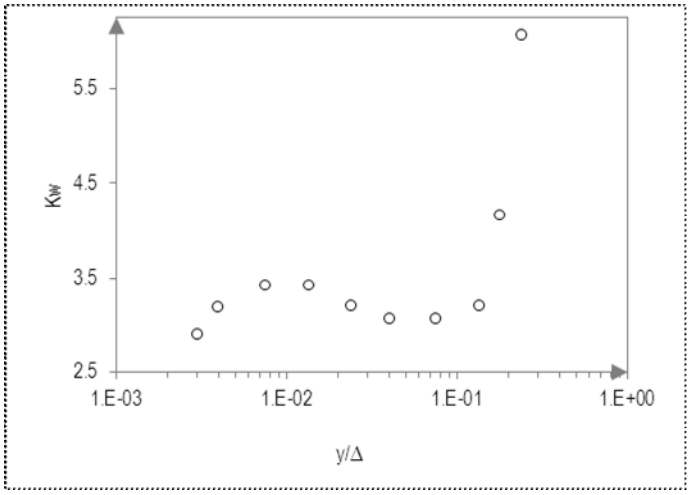

3(f)

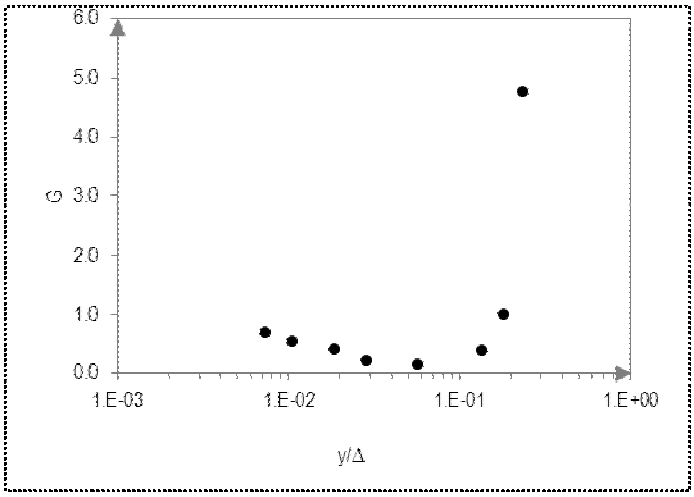

Figure B-4(3) *(continued)*
3(e) Variation of Kurtosis factor K of the spanwise fluctuating velocities w distribution.
3(f) Variation of the degree of non-Gaussianity $\tilde{G}$.

Near wall layer beneath turbulent separated flow

y^+	K_u	G_K	y^+	S_u	G_S
1.500	3.403	0.403	0.000	-0.423	0.423
3.000	2.824	0.176	1.604	-0.143	0.143
5.000	3.138	0.138	3.209	0.038	0.038
7.000	2.921	0.079	4.011	0.242	0.242
12.000	2.945	0.055	7.219	0.176	0.176
16.500	3.138	0.138	12.032	0.264	0.264
23.000	2.897	0.103	16.845	0.242	0.242
30.000	2.993	0.007	22.460	0.308	0.308
45.000	2.824	0.176	29.679	0.264	0.264
61.000	2.945	0.055	44.920	0.198	0.198
83.000	2.945	0.055	60.160	0.165	0.165
113.000	2.848	0.152	83.422	0.214	0.214
158.000	2.703	0.297	113.102	0.132	0.132
			158.021	0.110	0.110

y^+	G
1.500	0.403
3.000	0.176
5.000	0.242
7.000	0.176
12.000	0.264
16.500	0.242
23.000	0.308
30.000	0.264
45.000	0.198
61.000	0.165
83.000	0.214
113.000	0.152
158.000	0.297
Average	0.24

Table B-4d The corresponding plots are shown in Figure B-4(4).

4(a)

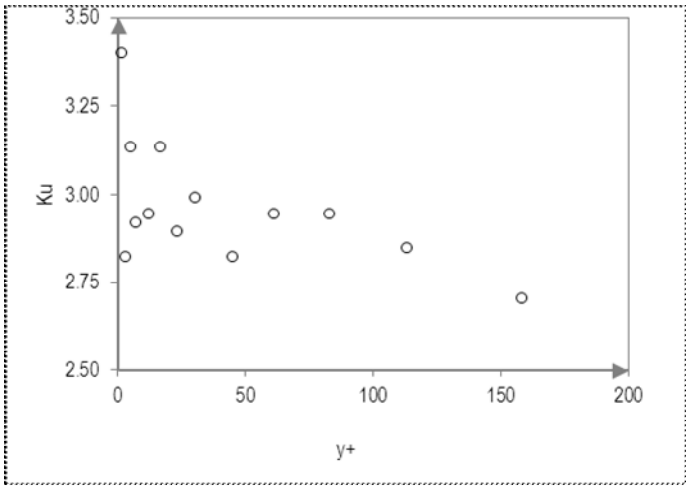

4(b)

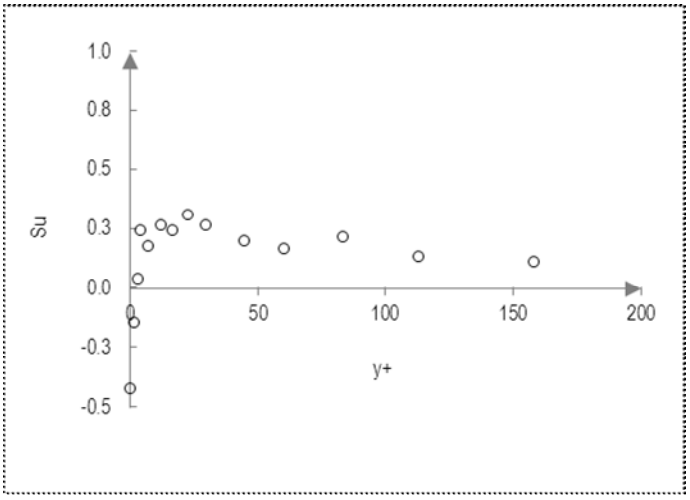

Figure B-4(4) Near wall layer beneath turbulent separated flow
4(a), 4(b) Kurtosis K and Skewness S factors variations,
respectively, of the fluctuating velocities distribution.

4(c)

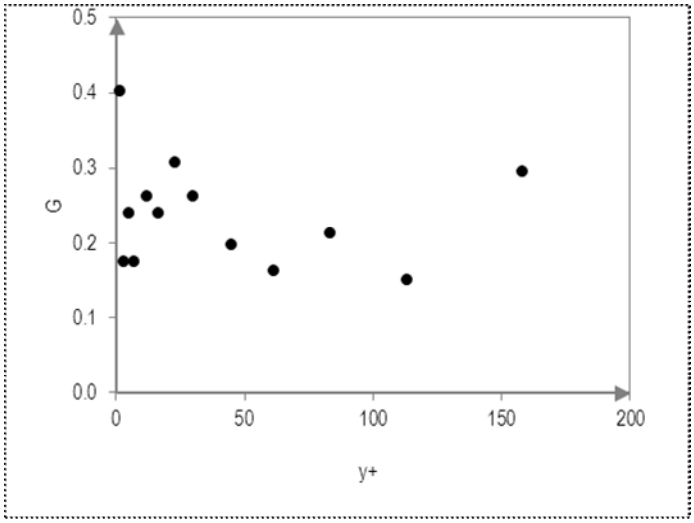

Figure B-4(4) *(continued)*
4(c) The degree of non-Gaussianity $\tilde{G}$ variation

Channel flow

	y+	K(u)	S(u)	K(v)	S(v)	K(w)	S(w)	G_K	G_S	G
viscous sublayer region	1.67	4.584	1.018			5.475	0.080	2.353	0.366	2.353
	2.11	4.250	0.935			5.250	0.035	2.167	0.323	2.167
	2.39	4.100	0.973			5.340	-0.010	2.147	0.328	2.147
	2.44	4.070	0.980			5.241	0.008	2.104	0.329	2.104
	2.66	4.340	1.070			4.845	0.080	2.062	0.383	2.062
	3.00	3.800	0.980			4.800	0.057	1.867	0.346	1.867
	3.54	3.665	0.913	3.710	0.980	4.766	0.007	1.047	0.633	1.047
	7.31	2.630	0.440	4.610	0.305	3.765	0.035	0.915	0.260	0.915
	10.67	2.231	0.080	4.745	0.305	3.267	-0.022	0.927	0.136	0.927
	15.70	2.275	-0.190	4.925	0.170	2.933	0.001	0.906	0.120	0.906
	29.99	2.810	-0.550	3.800	0.080	2.910	-0.010	0.360	0.213	0.360
	46.38	3.080	-0.527	3.485	0.125	2.980	0.035	0.195	0.229	0.229
	83.30	3.138	-0.502	3.440	0.170	3.103	-0.002	0.227	0.225	0.227
	146.69	3.338	-0.616	3.530	0.215	3.351	0.047	0.406	0.293	0.406
	200.00	3.530	-0.640	3.485	0.000	3.495	0.035	0.503	0.225	0.503

Table B-4e The corresponding plots are shown in Figure B-4(5)

5(a)

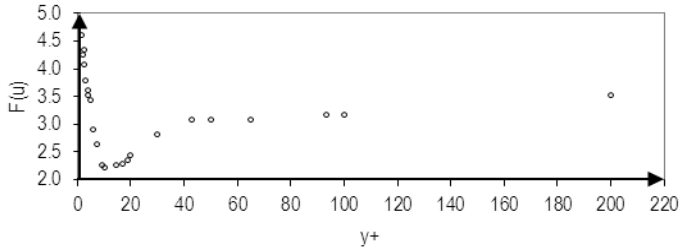

5(b)

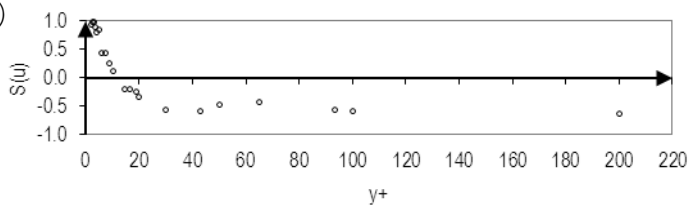

5(c)

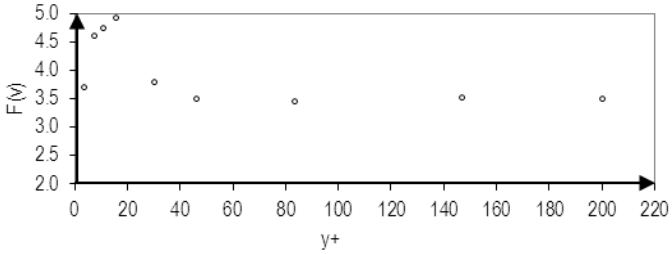

5(d)

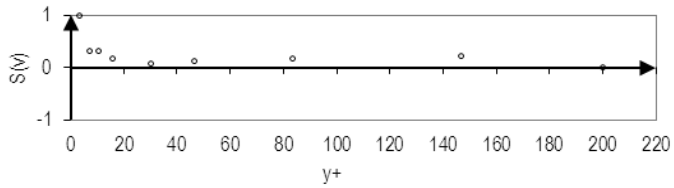

5(e)

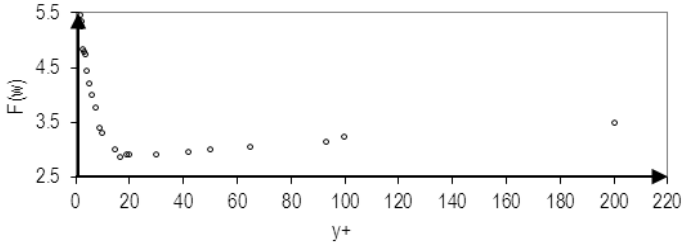

5(f)

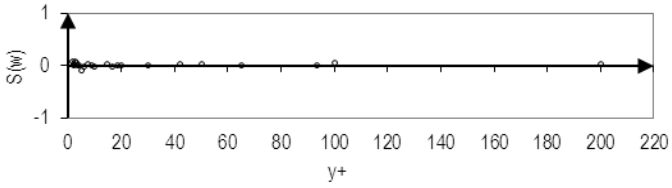

Figure B-4(5) Channel flow. 5(a)-5(f) Kurtosis K and Skewness S factors of the fluctuating velocity components (i.e. u, v, w) distributions.

5(g)

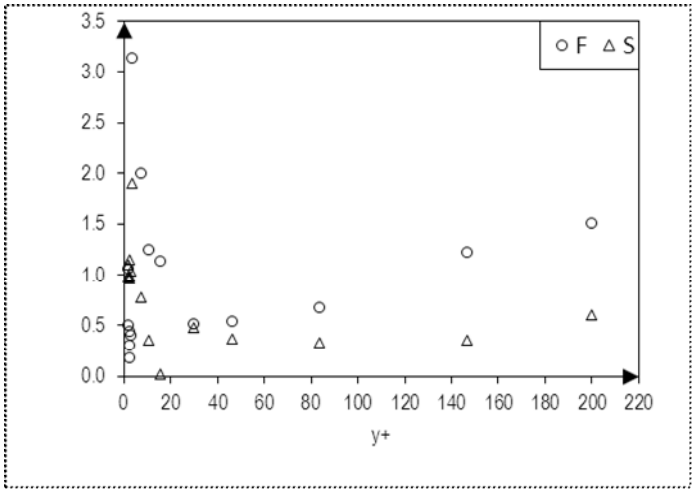

5(h)

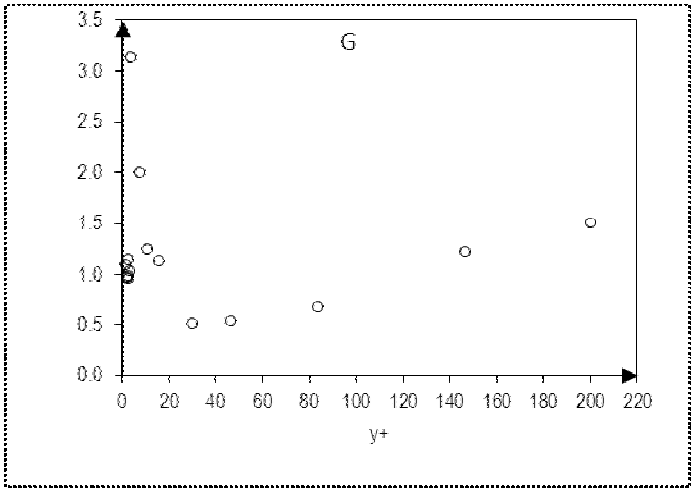

Figure B-4(5) *(continued)*

5(g) Variations of K and S which are the averages of K_i and S_i shown in 5(a)-5(f).

5(h) The degree of non-Gaussianity $\tilde{G}$.

Far plane turbulent wake

y/D	K_u	K_v	K_w	G_K
4.84	2.700	2.640	3.200	0.287
6.00	3.240	3.300	3.400	0.313
7.78	3.780	3.960	3.800	0.847
8.42	5.350	4.290	3.600	1.413
10.00	5.620	4.620	4.200	1.813
10.73	4.540	4.290	5.200	1.677
12.00	0.110	4.130	3.800	1.607

y/D	S_u	S_v	G_S
4.84	-0.600	0.520	0.373
6.00	-0.840	0.600	0.480
7.78	-1.020	0.680	0.567
8.42	-1.400	0.800	0.733
10.00	-1.400	0.960	0.787
10.73	-0.920	0.760	0.560
12.00	-0.880	0.080	0.320

y/D	G
4.84	0.373
6.00	0.480
7.78	0.847
8.42	1.413
10.00	1.813
10.73	1.677
12.00	1.607
Average	1.173

Table B-4f The corresponding plots are shown in Figure B-4(6)

6(a)

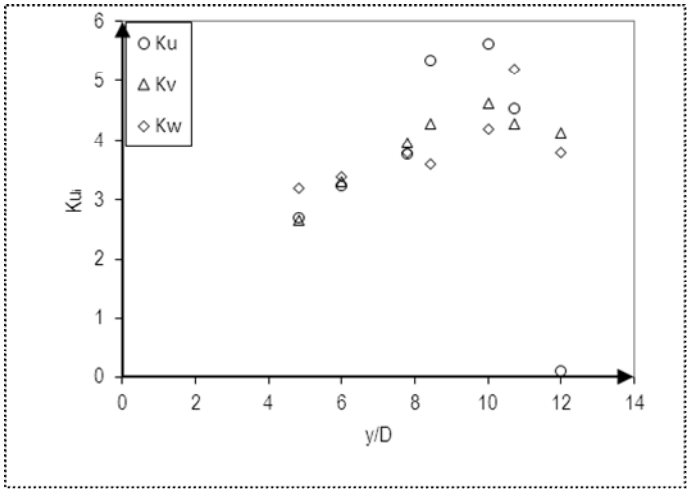

6(b)

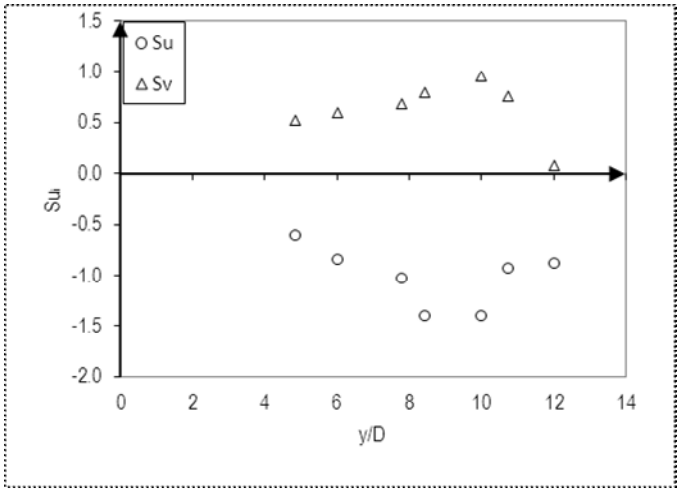

Figure B-4(6) Far plane turbulent wake
6(a), 6(b) Kurtosis K and Skewness S factors
variations, respectively, of the fluctuating velocities distribution.

6(c)

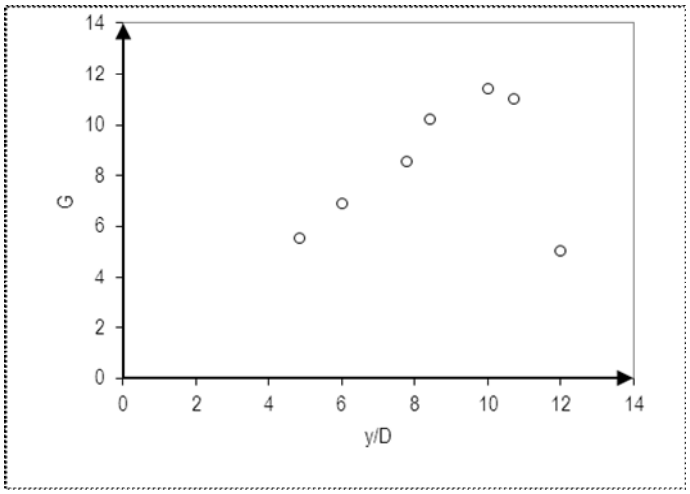

Figure B-4(6) *(continued)*
6(c) The degree of non-Gaussianity

Appendix C
Computing higher-moments using the master-modes in 3D channel flow

Let

$\mathbf{x}$ = position vector of reference

$\mathbf{r}$ = vectoral distance between 2 points x and x_1

u_i = fluctuating velocity $(i = 1, 2, 3)$

$u_1 = u_x$

$u_2 = u_y$

$u_3 = u_z$

STEP 1

Computing second-order correlations;

$$\langle u_i(\mathbf{x}) u_i(\mathbf{x}+\mathbf{r}) \rangle \qquad \text{(A-1)}$$

STEP 2

Obtaining third-order correlations;

$$\langle u_i^2(\mathbf{x}) u_i(\mathbf{x}+\mathbf{r}) \rangle \qquad \text{(A-2)}$$

STEP 3

Fourth-order correlations;

$$\langle u_i^3(\mathbf{x}) u_i(\mathbf{x}+\mathbf{r}) \rangle \qquad \text{(A-3)}$$

STEP 4

Extracting the second-order correlation functions [103; 104];

$$\frac{\left\langle \mathrm{u_i}(\mathbf{x})\mathrm{u_i}(\mathbf{x}+\mathbf{r})\right\rangle}{\sqrt{\left\langle \mathrm{u_i}^2(\mathbf{x})\right\rangle\left\langle \mathrm{u_i}^2(\mathbf{x})\right\rangle}} \tag{A-4}$$

Note that the outputs from the previous steps (i.e. STEPS 1 – 3) are obtained by modifying the numerator in (A-4).

STEP 5

At this stage and later, no simulations are involved. The outputs have been used to determine all the components of K_i and S_i;

$$S_{\mathrm{i}} = \frac{(\mathrm{A}-2)}{\left[(\mathrm{A}-1)/(\mathrm{A}-4)\right]^{3/2}} \tag{A-5}$$

$$K_{\mathrm{i}} = \frac{(\mathrm{A}-3)}{\left[(\mathrm{A}-1)/(\mathrm{A}-4)\right]^{2}} \tag{A-6}$$

The denominators in (A-5) and (A-6) are necessary for normalisation.

STEP 6

Calculating the 'deviation' from normal distribution;

$$S_1 - 0 \tag{A-7}$$

$$S_2 - 0 \tag{A-8}$$

$$S_3 - 0 \tag{A-9}$$

$$K_1 - 3 \tag{A-10}$$

$$K_2 - 3 \tag{A-11}$$

$$K_3 - 3 \tag{A-12}$$

The end magnitudes of these 'deviations' are kept.

STEP 7

Evaluating $\tilde{G}$;

$$\tilde{G} = max\left\{\frac{(A-10)+(A-11)+(A-12)}{3}, \frac{(A-7)+(A-8)+(A-9)}{3}\right\}$$

All seven steps are taken at each 'corresponding' grid point.

Appendix D
ERCOFTAC Application Challenge and Underlying Flow Regime Indexes

The sector disciplines of interests are Built Environment, Chemical and Process Engineering, External Aerodynamics, Turbomachinery, Combustion and Heat Transfer. Each Application Area is comprised of Application Challenges (AC) which are realistic industrial test cases used to judge the competency and limitations of CFD for a given Application Area [53]. See Table D-1 for AC index.

Application Area	AC number	Application Challenges
External Aerodynamics		
	1-01	Aero-acoustic cavity
	1-02	RAE M2155 Wing
	1-05	Ahmed body
	1-08	L1T2 3 element airfoil
Combustion		
	2-01	Bluff body burner for CH4-HE turbulent combustion
	2-06	The confined TECFLAM swirling natural gas burner
	2-07	Confined double annular jet
	2-08	Premixed Methane-Air Swirl Burner (TECFLAM)
	2-09	SANDIA Flame D
Chemical & Process, Thermal Hydraulics & Nuclear Safety		
	3-01	Buoyancy-opposed wall jet
	3-02	Induced flow in a T-junction
	3-03	Cyclone separator

Table D-1 AC Index

Application Area	AC number	Application Challenges
Chemical & Process, Thermal Hydraulics & Nuclear Safety		
	3-08	Spray evaporation in turbulent flow
	3-10	Combining/dividing flow in Y junction
	3-11	Downward flow in a heated annulus
Civil Construction & HVAC		
	4-01	Wind environment around an airport terminal building
	4-02	Flow and Sediment Transport in a Laboratory Model of a stretch of the Elbe River
	4-03	Air flows in an open plan air conditioned office
	4-04	Tunnel fire
Environmental Flows		
	5-05	Boundary layer flow and dispersion over isolated hills and valleys
Turbo-machinary Internal Flows		
	6-02	Low-speed centrifugal compressor
	6-05	Annular compressor cascade with tip clearance
	6-06	Gas Turbine nozzle cascade
	6-07	Draft tube
	6-08	High speed centrifugal compressor
	6-10	Axial compressor cascade
	6-12	Steam turbine rotor cascade

Table D-1 *(continued)*

The Underlying Flow Regimes (UFR) are generic, well studied test cases capturing important elements of the key flow physics encountered across the Application Areas [53]. Table D-2 shows the UFR index.

Flow type	UFR number	Underlying Flow Regime
Free Flows		
	1-01	Underexpanded jet
	1-02	Blade tip and tip clearance vortex flow
	1-05	Jet in a Cross Flow
	1-06	Axisymmetric buoyant far-field plume
	1-07	Unsteady near-field plume
Flows around Bodies		
	2-01	Flow behind a blunt trailing edge
	2-02	Flow past cylinder
	2-03	Flow around oscillating airfoil
	2-04	Flow around (airfoils and) blades (subsonic)
	2-05	Flow around airfoils (and blades) A-airfoil (Ma=0.15, Re/m=2x10^6)
	2-06	Flow around (airfoils and) blades (transonic)
	2-07	3D flow around blades
	2-10	Flow Around Finite-Height Circular Cylinder
	2-11	High Reynolds Number Flow around Airfoil in Deep Stall
Semi-confined Flows		
	3-01	Boundary layer interacting with wakes under adverse pressure gradient - NLR 7301 high lift configuration

Table D-2 UFR Index

Flow type	UFR number	Underlying Flow Regime
Semi-confined Flows		
	3-03	2D Boundary layers with pressure gradients (A)
	3-04	Laminar-turbulent boundary layer transition
	3-05	Shock/boundary-layer interaction (on airplanes)
	3-06	Natural and mixed convection boundary layers on vertical heated walls (A)
	3-07	Natural and mixed convection boundary layers on vertical heated walls (B)
	3-08	3D boundary layers under various pressure gradients, including severe adverse pressure gradient causing separation
	3-09	Impinging jet
	3-10	The plane wall jet
	3-11	Pipe expansion (with heat transfer
	3-12	Stagnation point
	3-13	Flow over an isolated hill (without dispersion)
	3-14	Flow over surface-mounted cube/rectangular obstacles
	3-15	2D flow over backward facing step
	3-18	2D Boundary layers with pressure gradients (B)
	3-30	2D Periodic Hill Flow
Confined Flows		
	4-02	Confined coaxial swirling jets
	4-03	Pipe flow - rotating

Table D-2 *(continued)*

Flow type	UFR number	Underlying Flow Regime
Confined Flows		
	4-04	Flow in a curved rectangular duct - non rotating
	4-05	Curved passage flow
	4-06	Swirling diffuser flow
	4-08	Orifice/deflector flow
	4-09	Confined buoyant plume
	4-10	Natural convection in simple closed cavity
	4-11	Simple room flow
	4-13	Compression of vortex in cavity
	4-14	Flow in pipes with sudden contraction

Table D-2 *(continued)*